2007

Design of nanoscale responsive polymer film for sensor application

Yen-Hsi Lin
Iowa State University

Design of nanoscale responsive polymer film for sensor application

by

Yen-Hsi Lin

A dissertation submitted to the graduate faculty

in partial fulfillment of the requirements for the degree of

DOCTOR OF PHILOSOPHY

Major: Materials Science and Engineering

Program of Study Committee:
Vladimir V. Tsukruk, Major Professor
Xiaoli Tan
Victor Shang-Yi Lin
Surya K. Mallapragada
Michael Kessler

Iowa State University

Ames, Iowa

2007

UMI Number: 3274850

ProQuest Information and Learning Company
300 North Zeeb Road
P.O. Box 1346
Ann Arbor, MI 48106-1346

TABLE OF CONTENTS

ACKNOWLEDGMENTS

First of all, I wish to express sincere appreciation to my POS committee for taking time out of their busy schedules. I would like to thank all those people who made this dissertation possible and an enjoyable experience for me. I am thankful to the members of my research group for technical advices and numerous favors as well as my second family in America during pass 5 years. I acknowledge my gratitude to Dr. Duangrut Julthongipiput (Mai) and Dr. Melburne LeMieux for aid and suggestion. In addition, special thanks for Dr. Sergey Peleshanko, Dr. Maryna Ornatska, Hyunhyub Ko, Michael McConney and Srikanth, Singamaneni whose familiarity with the needs and ideas of the community were helpful during the research.

The following research would not have been possible without the productive collaboration with Dr Zhong L. Wang (Georgia Tech.), Dr. Jr-Hao. He (National Taiwan University), Dr. Zhiqun Lin (Iowa State University), Dr. Eugene Zubarev (Rice University) and Jin Teng (Iowa State University) and Dr. Timothy. Bunning (AFRL). The research is supported by AFOSR, FA9550-05-1-0209, the National Science Foundation, NSF-CTS-0506832, DMR-0308982 Grants, and Grant M01-C03 from DOC through the National Textile Center.

Most of all, of course, I would like to express my deepest sense of gratitude to my supervisor Dr. Vladimir Tsukruk for his encouragement and excellent advice throughout this study. I would not be here today if not for Professor Vladimir Tsukruk. Despite his busy schedules, he is always there for students, listening our new idea for project, offering support, patient guidance, and make sure students are on the right track. I owe him more than I can say for his patience, persistence, insight and support.

I would like to thank Bryce Campbell for supporting and suggestions for the editing of my thesis. Finally, I take this opportunity to express my profound gratitude to my beloved parent, Chihua Lin and Limei Cheng.

ABSTRACT

The concept of fabricating sensing or responsive surfaces at the nanoscale has been the subject of extensive investigations since they can function as nanoscale device as well as next-generation miniaturized sensor. Polymers offer particular insights into the developments of novel responsive materials, which can be integrated with sensory systems to alter structure and properties in response to environmental stimuli. These responsive polymer nanolayers change surface composition and properties modulated by external triggers such as temperature, pH, solvent exposure, and light. This study explores possibilities of designing such polymer surfaces that possess versatile sensing mechanisms via controlled reorganization of chain and functional groups in multi-component and composite surface and then applying this into actual sensory systems of critical relevance. To achieve this, we designed novel nano-structured materials based on the employment of polymer methodologies, chemical functionality, and provide new capabilities by adding nanoparticles/nanowires to alter responsive polymer systems. We selected polymer with very different chemistry, switchable properties, and the surface composition which can be precisely controlled and divided into four groups: 1) switchable adaptive polymer nanolayer on planar silicon substrates, 2) compliant polymer or nanocomposite nanolayer enhancing/improving the sensitivity of current cantilever based sensors, 3) polymer nanolayer on ZnO nanobelt with enhanced photosensitivity 4) assembled ultra thin film with optical grating 3D structures. Furthermore, we designed and fabricated compliant polymer or nanocomposite films for thermal, chemical and light sensitive systems which can greatly enhance the sensitivity of corresponding micro/nanodevices.

CHAPTER 1

NANOMATERIALS SENSING LAYERS, AN OVERVIEW

Nanomaterials. Nature plays with the full range of objects on the length scale and functionality of any length scale arise from the complex interplay of its constituents (Figure1-1) [1] A particularly interesting length scale is of course, the nanoscale organization of matter. The definition of Nanomaterials in recent report[2,3] is a blend of definition of Nanoscience and Nanotechnologies (which is avoiding the use of dimension):

- **Nanoscience** is the study of phenomena and manipulation of materials at atomic, molecular, on macromolecular scales, where properties differ significantly from those at a large scale.
- **Nanotechnologies** are the design, characterization production, and application of structure, devices and systems by controlling shape and size on the nanoscale.

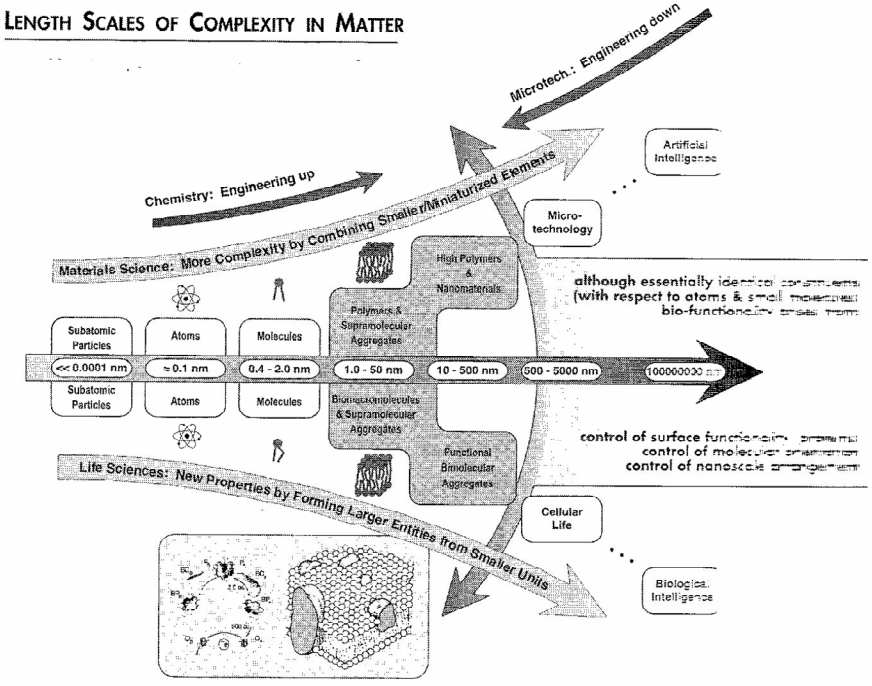

Figure 1-1. Length scale of complexity in Matter[1]

Nanomaterial technology is based on a convergence of basic disciplines such as technical physics, molecular biology and chemistry. Nanoscale level of operation and manipulation has opened up for a multidisciplinarity and combination of scientific paradigms leading to new research areas and possibilities for new technology development (Figure 1-2).[4] The nanotechnologies may be divided into a number of subsections such as nanostructured materials, nanoelectronics, nanophotonics, nanobiotechnology and nanoanalytics.

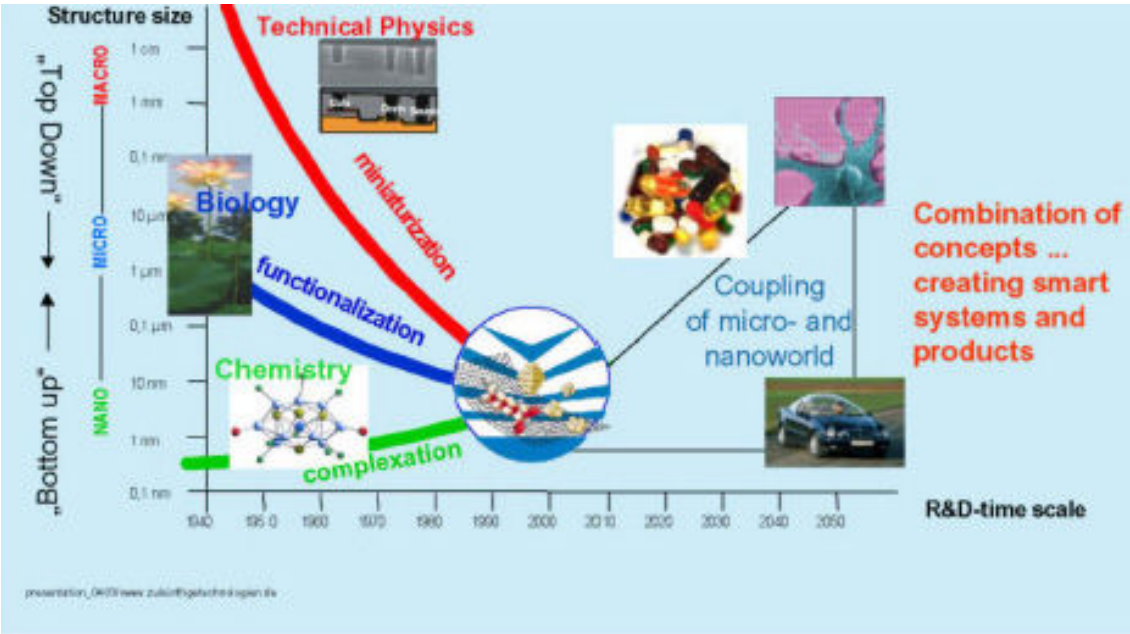

Figure 1-2. Multidisciplinarity combination of nanotechnology paradigms[4]

Nanomaterials can be all metals, ceramics, polymeric materials, or composite materials. Their defining characteristic length scale is in the range of 1-100 nanometers. Nanomaterials manifest extremely fascinating and useful properties, which can be exploited for a variety of structural and non-structural applications. For the current design of nanomaterial sensing layer is moving towards smaller, more flexible, and more versatile materials with exceptional mechanical properties. It is important to understand how nature has programmed the system to react and then to artificially recreate the process for developing sensing nanomaterials.

Synthesis and assembly of nanomaterials have shown great promise of advantage in applications such as nanoelectronics, photonics, computing, sensing, and diagnostics.[5,6,7,8,] It is critical to realizing the full potential of nanomaterials and one of the key is the directed assembly of sensing materials whose properties can be controlled in response to not only external *physical* stimuli (such as temperature[9], photonic[10], and electrical[11]), but also internal *chemical* stimuli, (such as pH variations[12] and the presence of a small molecule signaling the need for such materials). The challenge here is the controlled assembly of materials that respond to multiple internal stimuli with controllable stimuli cooperatively so that more complex architectures with multifaceted properties can be fabricated. With different combination of chemistry, the responsive surface can be fabricated via several different models of surface modification systems and be tuned under different environmental stimuli (Table 1-1).[13]

Physical	Chemical	Biochemical
Temperature	pH	Enzyme substrates
Ionic strength	Specific ions	Affinity ligands
Solvents	Chemical agents	Other biochemical agents
E. M. radiation (UV, visible)		
Electronic fields		
Mechanical stress, strain		
Sonic radiation		
Magnetic fields		

Table 1-1. Environmental Stimuli

Polymer based sensors Global research and development has expanded the field of sensor research (specifically in medical and environmental sectors) for the last 20 years. Sensors are engineered to measure various parameters such as electrical resistivity, chemical activity, magnetic permeability, thermal conductivity, and capacitance (table 1-2).[14] All of these characteristics depend greatly on the micro/nano structure (grain size)

of the materials employed in the sensors. A change in the sensor's environment is manifested by the sensor material's chemical, physical, or mechanical characteristics. Table 1-2 presents a list of materials used for the building of various sensor device.[15,16] The disadvantage and challenge of most these sensors is the thickness of the sensing layer (usually several microns thick). Current research is mainly focused on pushing the sensitivity limit and miniature size of sensors. Over the past 10 years, polymers have gained tremendous recognition in the field of artificial sensors for mimicking natural sense organs.[17] Enhanced selectivity and fast measurements have been fulfilled by replacing classical sensor materials with polymers involving nanotechnology and exploiting either the intrinsic or extrinsic functions of polymers[18]. Because of physico-chemical aspects of polymers, they are great candidate which offers particular insights into the developments of novel sensing materials for sensor device. Polymer chains always respond to some extent by changing their conformation and location of backbone segments, side chains, pendant groups or end groups.[19,20] Hence, polymer serves as the key elements to design sophisticated materials with responsive layer by variation of the length, chemical composition, architecture, and a topology of the chains for last two decades.[21,22,23,24,25]

Several approaches have been employed to design the responsive layer such as (a) synthesis of functional polymer with specific composition and architecture[26,27,28] (b) blending of virgin polymer materials with small amount of molecular additive[29,30,31] (c) surface modification by various chemical/physical treatments.[32, 33, 34] However, polymeric materials are not usually perfectly chemically or molecularly homogenous but are multicomponent system. By adding fillers such as ceramics metal or even air, scientists can generate an infinite variety of materials for sensor application. On the other hand, organization of structural features across several length scales is one of the challenging aspects in design responsive polymer layer. Inspired by nature, future polymeric layer will contain multifunctional components placed in the network holding it together to maintain functionality.

Type of sensor	Materials	Analyte
Semiconductor based solid-state sensors	Si, GaAs	H^+, O_2, CO_2, H_2S, propane etc.
Semiconducting metal oxide sensors	SnO_2, ZnO, TiO_2, CoO, NiO, WO_3	H_2, CO, O_2, H_2S, AsH_3, NO_2, N_2H_4, NH_3, CH_4, alcohol
Solid electrolyte sensors	Y_2O_3 stabilized ZrO_2	O_2 in exhaust gases of automobiles, boilers etc.
	LaF_3	F^-, O_2, CO_2, SO_2, NO, NO_2
	$SrCl_2$–KCl–AgCl, $PbCl_2$–KCl	Chlorine
	Ba $(NO_3)_2$–AgCl, $(AlPcF)_n$	NO_2
	ZrO_2–Y_2O_3	Dissolved oxygen in molten metals
	Na_2SO_4–$Y_2(SO_4)_3$–SiO_2	SO_2
	ZrO_2–Y_2O_3	N_2O
	Antimonic acid, HUP (hydrogen-uranylphosphate), Zr $(HPO_4)_2.nH_2O$, PVA/H_3PO_4, Nafion	H_2
	$Zr(HPO_4)_2.nH_2O$, Nafion	CO
	$SrCe_{0.95}Yb_{0.05}O_3$	H_2O
Membranes	Ion-exchange membranes	Cations and anions
	Neutral-carrier membranes	Cations and anions
	Charged carrier membrane	Anions
Organic semiconductors	Polyphenyl acetylene, phthalocyanine, polypyrrole, polyamide, polyimide	CO, CO_2, CH_4, H_2O, NO_x, NO_2, NH_3, chlorinated hydrocarbons

Table 1-2. Materials for various types of classical sensors[18]

Why Nano? Nanomaterials with extremely small feature sizes are the same scale as the critical size for physical phenomena. Fundamental electronic, magnetic, optical, chemical, and biological processes are also different at nano-scale level. However, just because materials can be made into very small scale does not immediately mean that they have any practical use.[35] The fact that these materials can be made at this scale gives them the potential to have some very interesting properties (Table 1-3). Materials at the scale between 1 nm and 100 nm are between the range of quantum effects of atoms and molecules and the bulk properties of materials.[2] It is in the range where many physical properties of materials are controlled by phenomena that have their critical dimensions at the nanoscale. By being able to fabricate and control the structure of nanomaterials, the scientist can influence the resulting properties and, ultimately, design materials to give desired properties. There are over 1500 companies involved in nanotechnology R&D

worldwide (Table 1-4). The number of nanomaterials companies significantly double in the 1990s and the split between types of materials.[36 37]

Field	Property	Scale length
Electronics	Electronic wavelength Inelastic mean free path Tunneling	10–100 nm 1–100 nm 1–10 nm
Magnetics	Domain wall Spin-flip scattering length	10–100 nm 1–100 nm
Optics	Quantum well Evanescent wave decay length Metallic skin depth	1–100 nm 10–100 nm 10–100 nm
Superconductivity	Cooper pair coherence length Meisner penetration depth	0.1–100 nm 1–100 nm
Mechanics	Dislocation interaction Grain boundaries Crack tip radii Nucleation/growth defect Surface corrugation	1–1000 nm 1–10 nm 1–100 nm 0.1–10 nm 1–10 nm
Catalysis	Surface topology	1–10 nm
Supramolecules	Kuhn length Secondary structure Tertiary structure	1–100 nm 1–10 nm 10–1000 nm
Immunology	Molecular recognition	1–10 nm

Table 1-3 characteristic lengths in solid-sate science[2]

Type of product	Number	Primary market focus	Percentage
Nanoparticles	160	Medical/pharmaceutical	30%
Nanotubes	55	Chemicals and advanced materials	29%
Nanoporous materials	22	Information and communication technology (ICT)	21%
Fullerenes	21	Energy	10%
Quantum dots	19	Automotive	5%
Nanostructured materials	16	Aerospace	2%
Nanofibers	9	Textiles	2%
Nanocapsules	8	Agriculture	1%
Nanowires	6		
Dendrimers	5		
Total	321		

Table 1-4 The primary materials product types and primary market focus of nanomaterials company[2]

There are also advantages of designing responsive layers by using polymer nanocomposites. These advantages result mainly from the filler size reduction and increase in surface area.[38,39,40,41] It is important to know that the filler size must be view relative to the size of polymer molecule to capture the full potential impact of nanoscale fillers on composite properties. When fillers are nanoscopic, the unique value-added properties is not normally possible comparing with traditional fillers, such as reduced permeability, optical clarity, self-passivation and increased resistance to oxidation and ablation.[42] Furthermore, many properties are related to the polymer chain which can be expressed as radius of gyration (R_g). Depending on the strength of interaction between the filler surface and the matrix, the polymer chains in close to the filler will be perturbed with respect to those in the bulk. Figure 1-3 shows the ratio of interfacial volume to the particle volume as function of the particle aspect ratio and the ratio of the interfacial thickness to the particle size.[42] However, properties of nanocomposite should not only depend on filler size, but high-aspect-ratio nanofillers will be more efficient for altering transport properties across a composite.

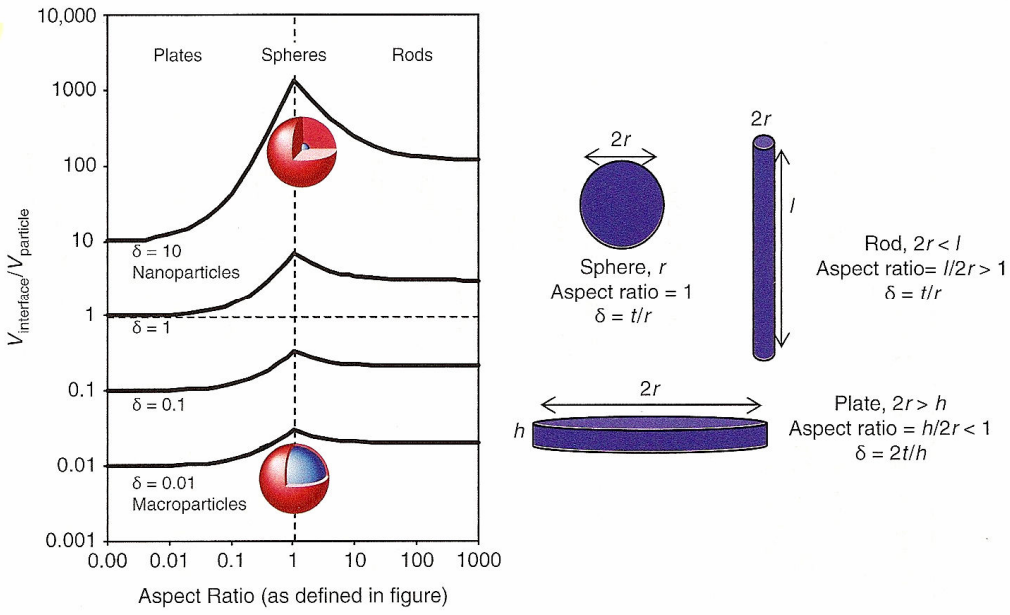

Figure 1-3. The ratio of interface volume of the particle[42]

Fabrication of Nanomaterials Techniques and specific instrumentation for nanomaterials fabrication are still under development and face significant challenges. In general, there are two philosophically distinct routes for fabricating nanomaterials: top-down and bottom up (Figure 1-4).[43] The most common top-down approach involves combination of lithography, etching, and deposition. The top-down approach aims to reduce the structure size of microscopic elements down to the nanometer scale. Small features are patterned in bulk materials to form functional device (ultraprecise surface figuring). The challenges of top-down approach are economic limitation and other scientific challenges (such as making structure with near-atomic perfection). Moreover, while applications continue to push towards higher resolution, the cost of new process for top-down process increases.[44, 45]

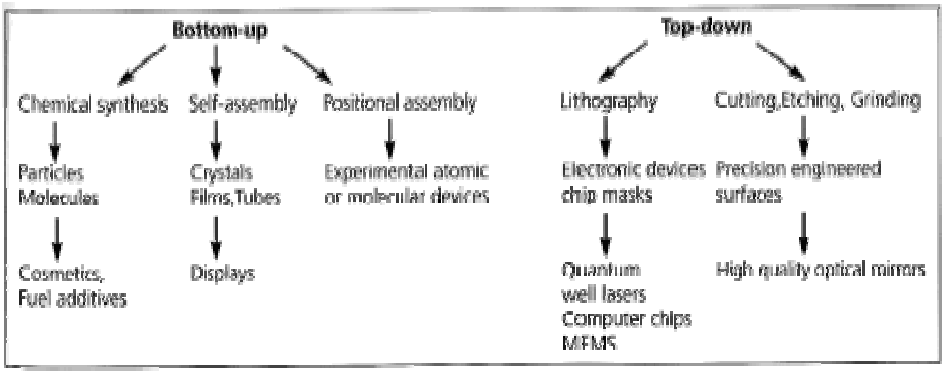

Figure 1-4. Bottom-up and top-down nano manufacturing techniques.[4]

"Bottom-up" techniques simply construct the desired features from fundamental building blocks, usually spontaneously, through self-assembly, without the need for patterning. The structures are assembled from well-defined chemically or physically the nanoscale building blocks and they represent a powerful alternative to conventional top-down method. The advantage of the bottom up approach is possible to seamlessly combine chemically distinct nanoscale building blocks that could not be integrated together in top-down processing and thus obtain unique function and/or combinations of

function in an integrated nanosystem.[46] Three key areas are required for bottom up approach:

- It necessitates nanoscale building block with precisely controlled and tunable chemical composition, structure, size and morphology since there characteristics determine their corresponding physical properties.
- It is critical to explore the limits of functional devices based on building blocks. Nanoscale structure may behave in a way similar to current devices, although it is also expected that new and potentially revolutionary concept will emerge from these building blocks.
- To develop architectures that enable high-density integration with predictable function and systematic assembly methods that can organize building block into these architectures.

From self-assembly to directed assembly of nanoscale sensing layer

An optimized route to a desired target structure for sensing surfaces is to use an assembly procedure that prevents equilibrium by trapping every compound kinetically in a pre-determined spatial arrangement. A variety of strategies have been adopted for deposition of sensing layer to substrate by casting,[47] self-assembly, monolayers,[48] polymer brushes[49], Langmuir-Blodgett (LB)[50,51] and layer-by-layer (LbL) assembly[52,53,54] While these approaches demonstrate the ability to produce sensing layer with reasonable uniform surface profile, the techniques are either high cost or require precisely process controlled and several optimization cycles are frequently required. By carefully designing specific molecular interactions upon various external stimuli, a novel class of responsive polymer coatings can be developed.

1.1 References

[1] Decher, G., Layered Nanoarchitectures via Directed Assembly of Anionic and Cationic Molecules, in Comprehensive Supramolecular Chemistry, Vol. 9, (Ed Sauvage J.-P., Hosseini M. W.), Pergamon Press, New York, 1996.

[2] M. J. Pitkethly, *Nanotoday*, **2004** 20.

[3] Nanoscience and nanotechnologies: opportunities and uncertainties, The Royal Society & The Royal Academy of Engineering, London, 2004.

[4] Pictures were taken from *Danish Environmental Protection Agency* Version 1.0 September 2006. http://www2.mst.dk/common/Udgivramme/Frame.asp?pg=http://www2.mst.dk/udgiv/publications/2006/87-7052-216-2/html/kap05_eng.htm,

[5] J. J. Storhoff, C. A. Mirkin, *Chem. Rev.* **1999**, *99*, 1849.

[6] C. M. Niemeyer, *Angew. Chem. Int. Ed.* **2001**, *40*, 4128

[7] E. Katz, I.Willner, *Angew. Chem. Int. Ed.* **2004**, *43*, 6042.

[8] Y. Yin, A. P. Alivisatos, *Nature* **2005**, *437*, 664.

[9] Y. G. Takei, T. Aoki, K. Sanui, N. Ogata, Y. Sakurai, T. Okanao *Macromolecules* **1994**, *27*, 6163.

[10] K. Ichimura, S.-K. Oh, Nakagawa, *Science* **2000**, *288*, 1624.

[11] L. Lahann, S. Mitragotri, T.-N. Trsn, H. Kaido, J. Dundaram, I. S. Choi, S. Hoffer, G. A. Somorjai, R. Langer, *Science* **2003,** 299, 371

[12] J. Lahann, R. Langer, *MRS Bull.* **2005**, *30*, 185

[13] D. J. Beebe, G. A. Glennys; G. M. Walker, *Ann. Rev. of Biomedical Eng.* **2002** *4*, 261

[14] M. J.Morrison, S. R. Morrison London, *Chemical Sensing with Solid State devices*, Acedemic Press; 1989.

[15] E. C. M. Hermans, *Sens. Actuators* **1985**, *8*, 227

[16] B. Bott, T. A. JONES, *Sens. Actuators* **1986**, *9*, 19.

[17] M. W. Urban, *J. Macromol. Sci., Polym. Rev.* **2006**, *46,* 329.

[18] B. Adhikari, S. Majumdar, *Prog. Polym. Sci.* **2004**, *29*, 699.

[19] T. P. Roussel, *Science* **2002**, *297*, 964.

[20] I. Luzinov, S. Minko, V. V. Tsukruk, *Prog. Polym. Sci.* **2004,** *29*, 635.

[21] C. Creton, *MRS Bull* **2003**, *28*, 434.

[22] V. V. Tsukruk, K. Wahl, Editors, *Microstructure and microtribology of polymer surfaces* **vol. 741**, ACS Symposium Series, Washington, **2000**.

[23] T. M. Birshtein, V. M. Amoskov, *Comput Theor Polym Sci* **2000**, *10* 159

[24] V. N. Bliznyuk, M.P. Everson, V.V. Tsukruk. *J Tribol*, **1998**, *120*, 489.

[25] V. V. Tsukruk, V. N. Bliznyuk, *Langmuir* **1998**, *14,* 446.

[26] R. Mason, C. A. Jalbert, P .A. V. O'Rourke Muisener, J. T. Koberstein, J. F. Elman, T. E. Long, B. Z. Gunesin, *Adv Colloid Interface* **2001**, *94*, 1.

[27]. C. J. Jalbert, J. T. Koberstein, R. Balaji, Q. Bhatia, L. Salvati, Jr., I. Yilgor, *Macromolecules* **1994**, *27*, 2409.

[28] M. O. Hunt, Jr., A. M. Belu, R. W. Linton, J. M. DeSimone, *Macromolecules* **1993**, *26*, 4854.

[29] J. Höpken, M. Möller, *Macromolecules* **1992,** *25*, 1461.

[30] A. Aymonier, E. Papon, *MRS Bull* **2003,** *28,* 424.

[31] A. Vaidya, M. K. Chaudhury, *J Colloid Interface Sci* **2002**, *249*, 235.

[32]. S. Randall Holmes-Farley, R. H. Reamey, R. Nuzzo, T. J. McCarthy, G. M. Whitesides, *Langmuir* **1987**, *3*, 799.

[33] G. M. Whitesides, P. E. Laibinis, *Langmuir* **1990**, *6*, 87.

[34] D. H. Carey, G. S. Ferguson,. *J Am Chem Soc* **1996,** *118*, 9780.

[35] C. Joachim, *Nat. Mater*. **2005**, *4*, 107.

[36] J. S Murday., *AMPTIAC Newsletter*, **2002**, *6*, 5.

[37] Nanoscience and nanotechnologies: opportunities and uncertainties, The Royal Society & The Royal Academy of Engineering, London, **2004.**

[38] R. A. Vaia, H. D. Wagner, *Mater. Today*, **2004,** *7*, 32.

[39] A. Bansal, H. Yang, C. Li, K. Cho, B. C. Benicewicz, S. K. Kumar, L. S. Schadler, *Nat. Mater*. **2005**, *4*, 693.

[40] R. Krishnamoorti, R. A.Vaia, E. P. Giannelis, *Chem. Mater* **1996**, *9*, 1728.

[41] F. W. Starr, T. B. Schroeder, S. C. Glotzer, *Macromolecules*, **2002,** *35,* 4481.

[42] K. I. Winey, R. A. Vaia, *MRS Bull* **2007,** *32,* 314.

[43] C. M. Lieber, Z. L. Wang, *MRS Bull* **2007,** *32***,** 99**.**

[44] J. D. Meindl, Q. Chen, J. A. Davis, *Science*,**2001**, *293*, 2044.

[45] C. M. Lieber, S*ci. Am.* **2001**, *285*, 58.

[46] J. R. Heath, P. J. Kuekes, G. S. Snider, R. S. Williams, *Science*, **1998** , *280*, 1716.

[47] T. Otagawa, M. Madou, S. Wing, J. Rich-Alexander, S. Kusanagi, T. Fujioka, A. Yasuda, *Sens. Act. B.* **1990**, *1*, 319.

[48] C. D. Bain, G. M. Whitesides, *Science*, **1988**, 240, 62.

[49] B. Zhao, W. J. Brittain, *Prog. Polym. Sci.* **2000**, *25*, 677.

[50] K. B. Blodgett, *J. Am. Chem. Soc*. **1934**, *56*, 495.

[51] K. B. Blodgett, I. Langmuir, Phys. Rev. **1937**, *51*, 964.

[52] G. Decher, *Science,* **1997**, *277,* 1232.

[53] C. Jiang, V. V. Tsukruk, *Adv. Mater.* **2006**, *18*, 829

[54] Z. Tang, Y. Wang, P. Podsiadlo, N. A. Kotov, *Adv. Mater.* **2007**, *19*, 906.

CHAPTER 2

SUMMARY OF RESEARCH AND GENERAL DISCUSSION

2.1. Goal and Objectives

The ultimate goal of this research is to provide insight into development of novel highly sensible and flexible responsive polymer nanolayers. The focus of this work is on the design of nano-structured materials based on the employment of polymer methodologies, chemical functionalization, and providing new capabilities by adding nanoparticles/nanowires to tune responsive polymer systems. In addition, the establishment of an innovative design paradigm for multifunctional polymer coatings with inorganic semiconductive nanodevices for improving the sensing performance will be developed. These responsive polymer nanolayers will change surface composition and properties by external triggers such as temperature, pH, solvent exposure, and light. To approach this goal, we will test their fundamental physical properties and microstructures, which are critical for sensing applications.

2.2. Approaches and Thesis Organization

Several steps must be taken to accomplish these goals and reach the ultimate performance of responsive nanolayers. These approaches can be organized into *Research Strategy Map* (shown in Figure 2-1) which includes three phases: design, fabricate (integrate materials), and characterize. The first phase of this study is design phase, which can be broken down into several fundamental steps and it plays key role for this research. Second phase involves fabrication which shows three main foci of responsive nanolayers design and methodologies for this study. Finally, these responsive layers are prepared, designed, and characterized in order to achieve the goal.

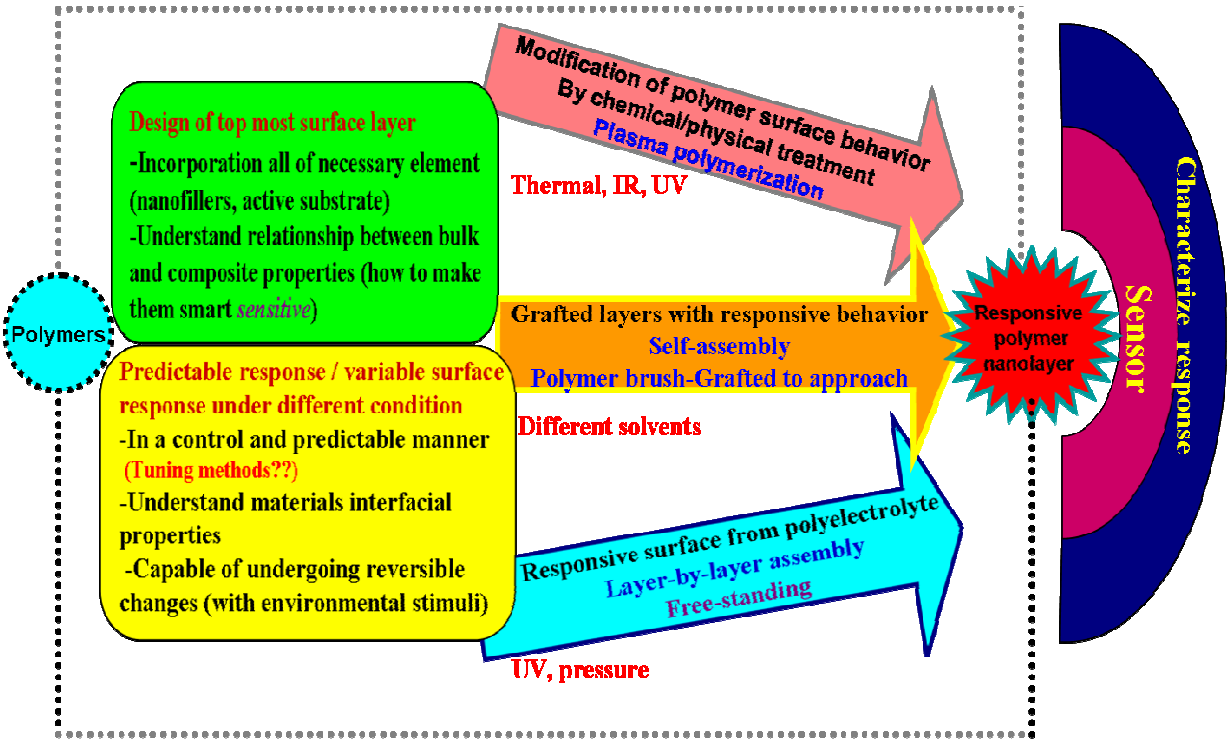

Figure 2-1 Research Strategy Map

Researches here are conducted in several stages with focus on:

I. Stimuli-responsive Y-shaped amphiphilic binary polymer brush nanolayers

- Fabricate stimuli-responsive Y-shaped amphiphilic brushes by using the "grafting to" approach.
- Control selective adsorption of functionalized gold nanoparticles on Y-shaped amphiphilic polymer brush layers.
- Understand the switching behavior and nanomechanical properties of the Y-shaped polymer brush layer under various solvents.

II. Thermally responsive polymer nanocomposite coatings on microcantilevers

- Fabricate thermally responsive homopolymer layers by "grafting to" approach.

- Design polymer nanocomposite assemblies into thermally responsive layers by incorporating reinforcing nanowires and metal nanoparticles which are strongly absorb and respond to a thermal flux.

III. Design and integration of responsive polymer coating on ZnO nanobelt for UV photosensing.

- Design and fabricate new photodetector architectures by exploiting plasma enhanced chemical vapor deposition (PECVD).
- Understand the mechanism of photoconduction in nanobelt/ plasma polymerized polymer structures.

IV. Sculptured LBL ultra thin films as optical gratings

- Design 3D free-standing LbL ultra thin film by microcontact printing method.
- Assemble ulta-thin LbL films composed of a non-conjugated polyelectrolyte and a conjugated polymer.

2.3 Summary of Major Results

2.3.1. Nanoscale stimuli-response polymer surface

Over the last few years, polymer scientists have been involved with the synthesis and application of stimuli-responsive polymer systems.[1] Stimuli-responsive polymer surfaces are capable of sensing subtle changes in their surrounding environment such as pH,[2] surface pressure,[3] temperature,[4] light,[5] electronic potential[6] and solvent quality.[7,8,9] These stimuli-responsive principles can be used for delivering or adsorbing species and applied for nano-electromechanical, bioanalytical, and microfluidic devices. [10,11,12,13,14,15] The research direction for designing stimuli-responsive polymer surface is to obtain suitable internal structures and optimal parameters to create the optimal adaptive response. Some surfaces are designed to respond to a combination of two or more stimuli. Several modification approaches of well-defined surfaces are, e.g. grafting of a stable preformed polymer, direct initiation of polymer chain growth from a surface, polyelectrolyte LbL

deposition, and polymerization within a film. Future developments of novel responsive surfaces need to have multi-stimuli-responsive properties as well as enhance the sensitivities of responsive systems for different sensing applications. The most recent interest is to use natural polymers such as proteins and DNAs which have specific secondary structures and colloidal nanoparticles incorporating stimuli-response systems to create specific structures on the nanoscale. [16,17,18]

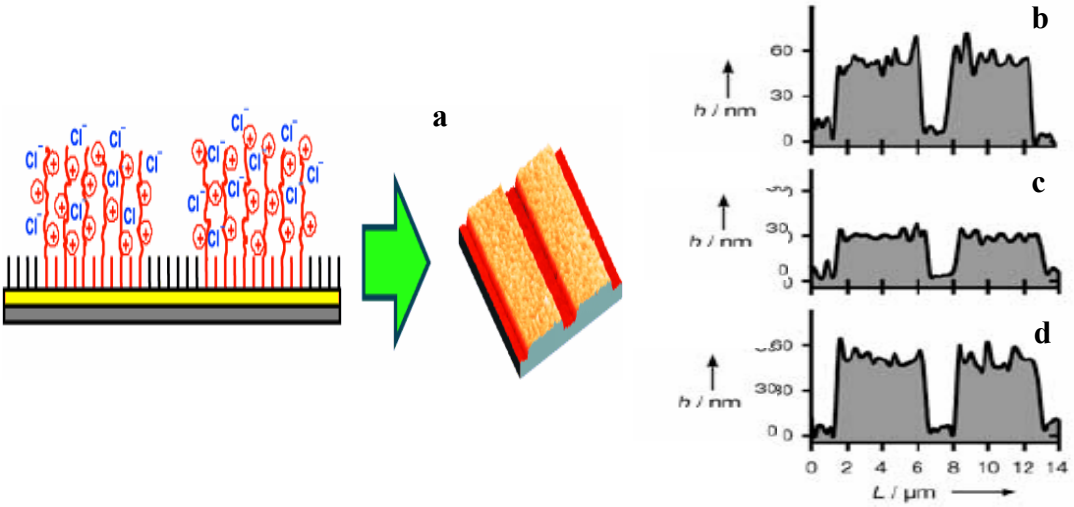

Figure 2-2. (a)The polyelectrolyte brushes can be switched between collapsed or extended states with different surface properties: a step toward the use of surface-confined polyelectrolytes as nanoactuators. Cross-sectional analysis derived from AFM imaging of polyelectrolyte brushes in b) water, c) in NaCl and (d) in water after treatment with NaCl.[24]

Stimuli-responsive polymer surfaces have been fabricated by using a variety of approaches such as the reversible photoisomerization reaction, reversible temperatue-shrink/extension, collapsed/extended ionic-strength sensitive polyelectrolyte brush (Figure 2-2), swelling/collapse of water-soluble grafted polymers, and phase separation in binary grafted brushes or diblock copolymers.[19,20,21,22,23,24] Recently a reversible switching surface has been fabricated from mixed, binary brushes grafted onto a solid substrate.[25,26,27,28,29,30,31] Theoretical consideration predicts that such binary brushes with two incompatible brushes

should form a wide variety of segregated surface layers with various surface micellar structures controlled by chemical attachment, grafting density, and composition.[32,33,34] Such surfaces can be reversibly triggered, patterned, and switched. More recently, a novel binary Y-shaped polymer brush surface has been theoretically simulated and predicted to form smaller characteristic dimensions on "*molecular scale*" with microscopic responsive properties.[35]

Development of stimuli responsive Y-shaped binary polymer brush layer.

For development of a novel responsive polymer film, we fabricated a new type of Y-shaped amphiphilic polymer brush layer tethered to a solid substrate by a "grafting to" approach. We introduced Y-shaped amphiphilic brushes combining two dissimilar, hydrophobic and hydrophilic polymer chains (PS and PAA) attached to a single focal point (Figure 2-3, Prof. E. Zubarev, Rice University). Different conformation changes of dissimilar polymer chains A and B results in dramatic structural reorganization with outstanding switching ability under alternating treatments with different solvents.

The formation of the nanoscale surface structures with organized, patterned morphology had been theoretically predicted for Y-shaped molecules but has been never observed experimentally. Thus, we focused on direct observation of the nanoscale interfacial (at solid-fluid interfaces) structures of Y-shaped binary brushes under different fluids (solvents of different quality). In order to observe the properties of switchable polymer layers between a sticky hydrophilic surface and repellent hydrophobic surface directly in a fluid, we used AFM and surface force spectroscopy (SFS) to probe morphology, microroughness, adhesion, and elastic modulus of the Y-shaped brush layers. We also attempted to tune the frictional force and wear properties of the Y-shaped brushes layers which depend strongly on the morphology and composition of the brushes layers.

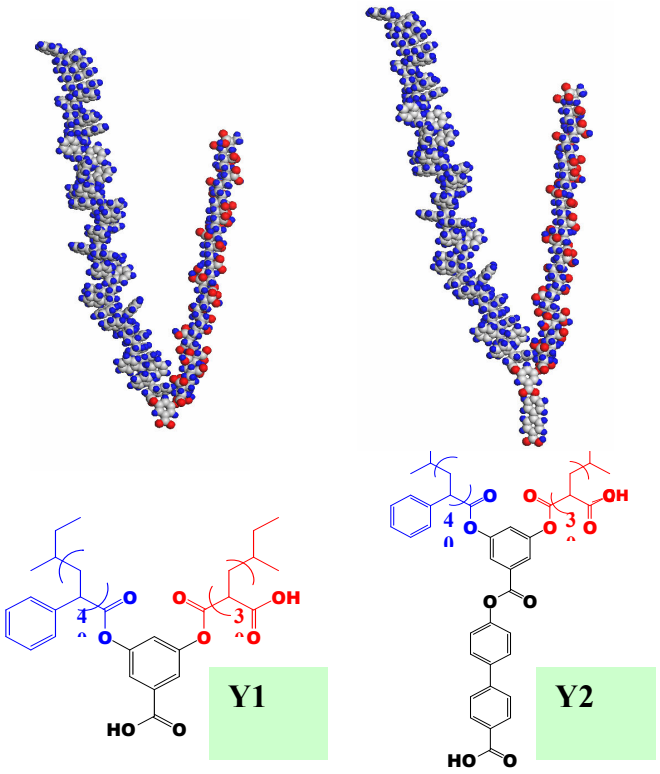

Figure 2-3. Chemical structure and molecular graphics representation of Y-shaped block copolymers with short (Y1) and long (Y2) aromatic functional stem. Molecules contain 40 and 30 monomeric units in PS and PAA arms, respectively.

For the fabrication of the Y-shaped brush layer, a melt/solution were "grafting to" a chemically reactive silicon surface functionalized with epoxy-terminated SAMs as describe below.

SAM formation

All the SAM formation procedures were established in our group and were used in this work.[36,37] The epoyexysilane solutions in toluene were prepared in oven-dried glassware in a nitrogen-purged glovebox (under relative humidity below 10). After the rinsing, the substrates were dried under a stream of dry nitrogen and immediately taken into the nitrogen-filled glovebox and immersed in epoxysilane solutions of 1.5%(v/v) concentrations for different periods of deposition time (from 10 s to 18 h). After the deposition was complete, the modified substrates were removed from solution and rinsed

several times with toluene. To remove unbound deposited polymers, the substrates were additionally placed in toluene in the ultrasonic bath for 20 min. The SAMs formed were dried overnight a stream of dry nitrogen at ambient conditions before measurements.

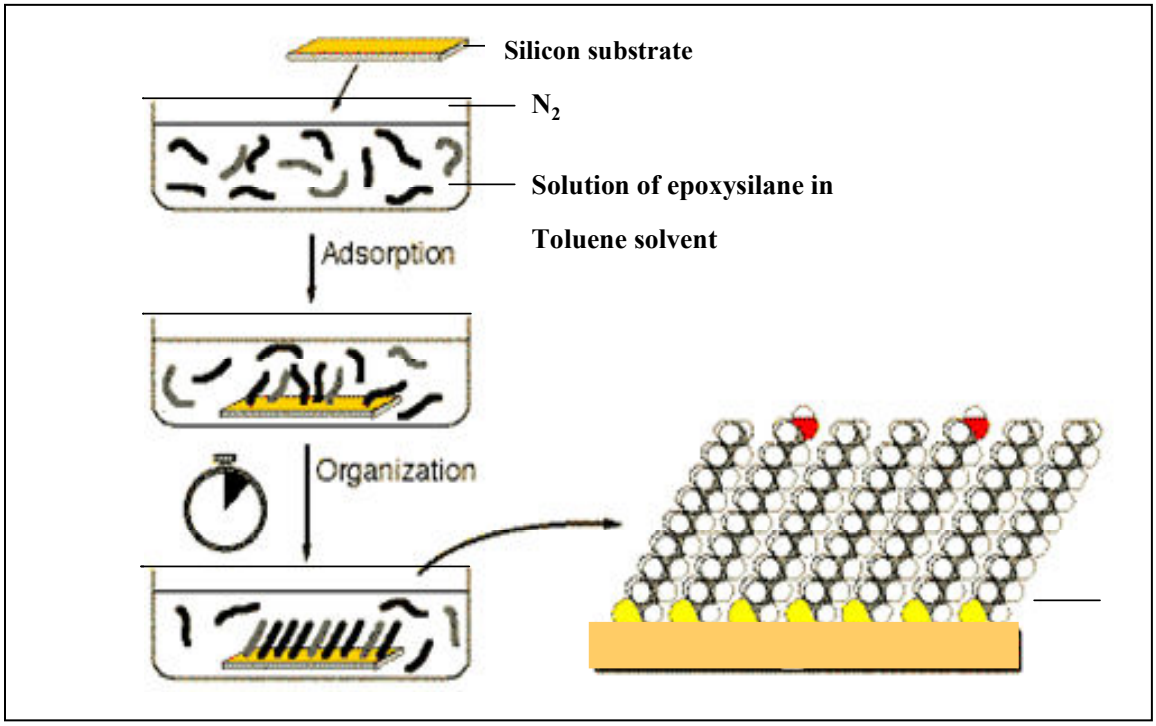

Figure 2-4 Schematic of SAMs formation[38]

Y-shaped polymer layer formation

For all Y-shaped polymers, 18 hrs of grafting time is enough to approach a virtually constant thickness of grafted layer.[36] We investigate the structure of Y-shaped polymer brush with grafting time between 15 min to 18 hrs and grafting temperature between room temperature to 150 ° C to ensure the development of organized microphase structure within the molecular thin film. The challenging of this design is that thin films of polymer have tendency to dewett a surface because of their inherently unstable nature

although polymer brush which can prevent the dewetting effectively due to entanglements between tethered and free polymer chain.[39,40,41]

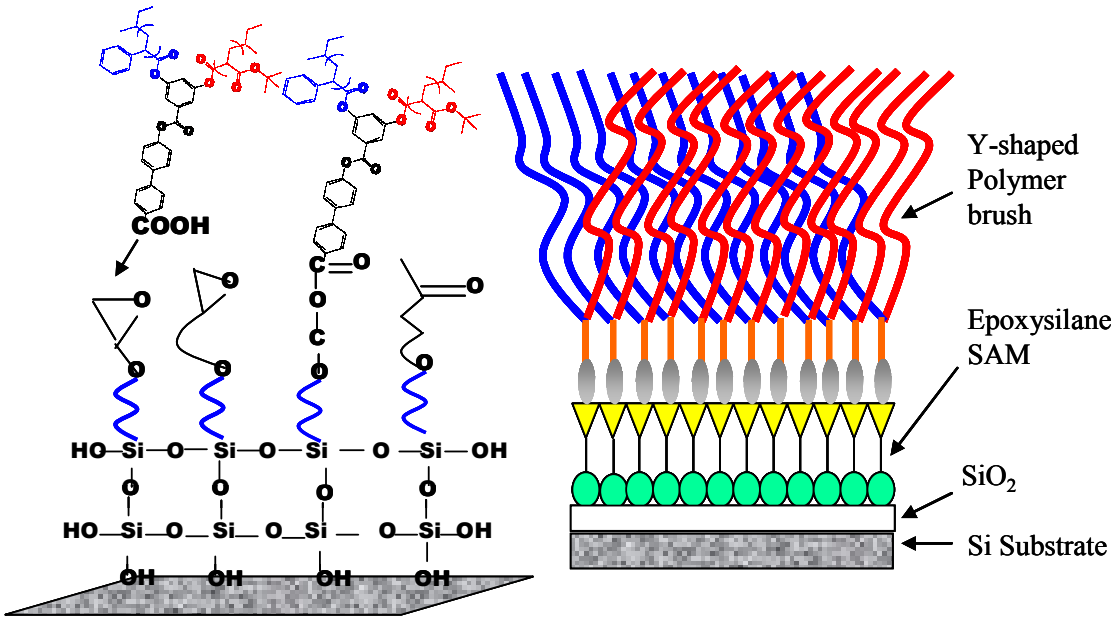

Figure 2-5. Schematic of Y-shaped brushes layer formations.

To change the Y-shaped PS/PtBA composition polymer brush into two very dissimilar arm, we hydrolyzed PtBA arms to hydrophilic poly(*t*-butyl acrylate) PAA arms imparting amphiphilicity to the Y-shaped brush. The grafted PS-PBA polymer brush was hydrolyzed in the mixture of 30% tetrahydrofuran and 70% trifluoroacetic acid for 48 h. The hydrolyzed polymer brush was rinsed with Nanopure water and toluene followed by an ultrasonic bath.

Y-shaped PS-PAA switchable surface properties

To investigate the limits of the surface reorganization of the amphiphilic Y-shaped brushes, PS-PAA brush was treated with different solvents. To investigate of the surface reorganization, the brush was immersed in three different solvents including toluene (good solvent for PS), mixed solvent of 50% methanol and 50% chloroform (nonselective solvent), and water (good solvent for PAA)..

The contact angle values showed apparent changes after three solvent treatments. After toluene treatment, contact angle reached 81° and decrease by 10°° after mix solvent treatment. Ultimately, the contact angle value decrease 20° degree more after exposure of the sample in water. A reorganize (swell and collapse) kinetic can be expected in this manner (Figure 2-6). We also obtained switch properties from surface morphologies. From Figure 2-7, an array of reversible *crater-like* nanoscale features was observed for both Y-shaped brushes after water and toluene treatments. We proposed a model of these segregated pinned micelles and the corresponding reverse micelles (crater-like structures) featuring different segregation states of hydrophobic PS and hydrophilic PAA arms (Figure 2-8). The arms undergo conformational rearrangements in selective solvents in a controlled and reversible fashion. These nanoscale structural reorganizations define adaptive wetting surface.

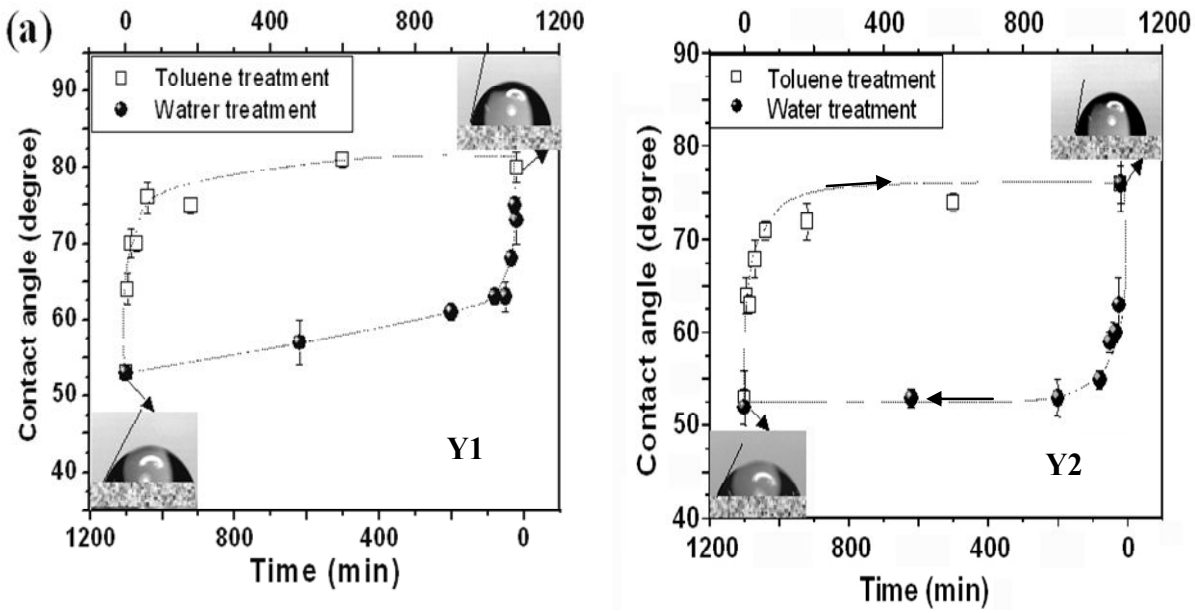

Figure 2-6 Cyclic dynamics of Y-shaped surface wetting properties as a function of solvent treatment time

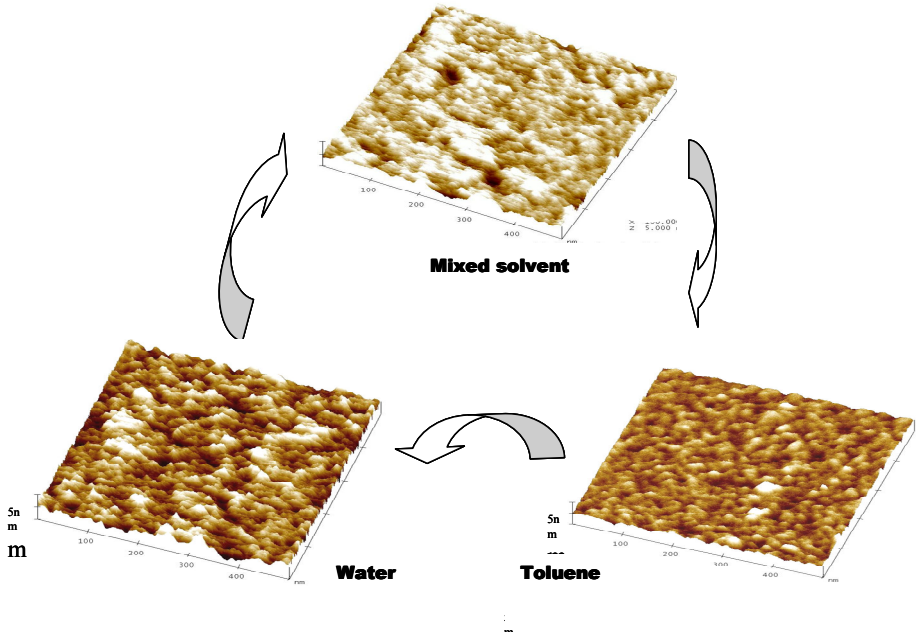

Figure 2-7. Representative 3D topographical images of Y1 brush layer (500 nm x 500 nm x 10 nm) in different solvent.

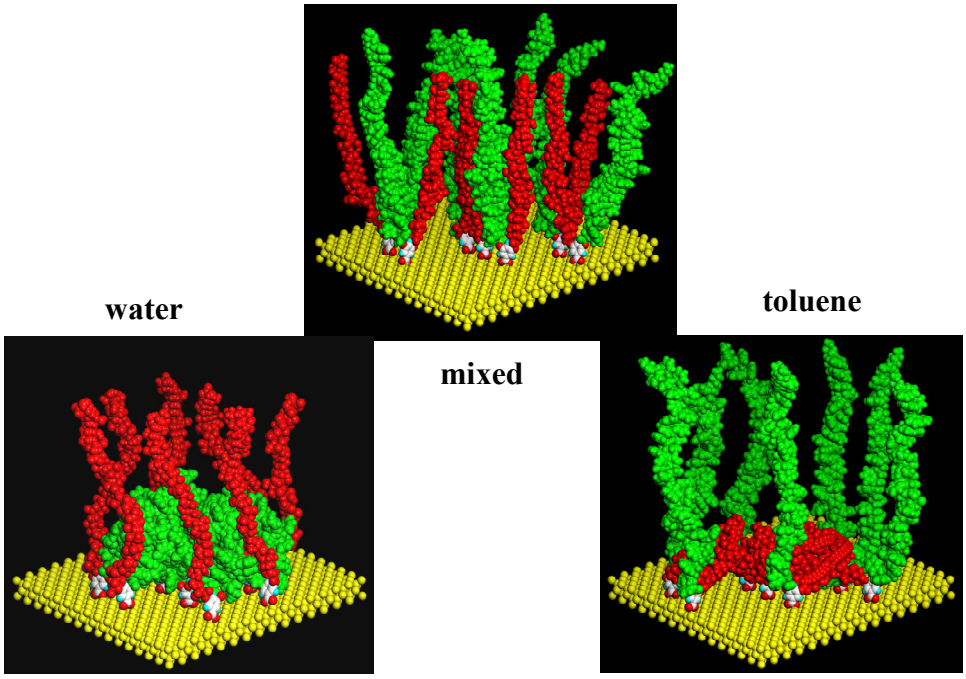

Figure 2-8. Molecular models showing internal molecular organization of an individual cluster comprising 7 Y1 molecules (green and red chains represent PS and PAA arms, respectively)

Y-shaped brush was also imaged in tapping mode in aqueous media to exam the brushes in "real environment" (different solvents). Although oscillation of the cantilever in liquid incurs some disadvantages associated with damping of the cantilever motion by liquid and higher force are need to oscillation, its eventual application in liquid brought the advantages of the technique to relevant environment. Operating AFM under liquid significantly reduces disruptive influence of lateral force and also decrease the energy dissipation by lateral force which causing deformation of soft polymer surface. Atomic force microscopy (AFM) imaging of **Y1** and **Y2** brush layers in toluene (selective solvent for PS arms), water (selective solvent for PAA arms), and mixed solvent of chloroform and methanol (1:1) (good solvent for both arms) revealed non-uniform surface morphology with grainy nanoscale texture (Figure 2-7)..

Force-volume testing of wet polymer brush layers gives direct insight into Y-shaped mechanical properties. Several previous reports demonstrate that AFM force and distance profile of the polymer brush layers are sensitive in different solvents and AFM tip can penetrate the brush.[42,43,44] Surface histograms measured directly in water with a lateral resolution below 10 nm showed *bimodal distribution* of the elastic response for Y-shaped brush layer in water. Compliant surface areas with low elastic modulus (E = 4.3 MPa) and stiffer surface areas with higher elastic modulus (E = 110 MPa) coexisted in brush layer in water. In contrast, the testing of the elastic response of brush layer in toluene which is a good solvent for PS arms showed a uni-modal distribution of the elastic response with the average value of the elastic modulus centered around 4.6 MPa, a characteristic value for a polymer swollen in a good solvent

.

Finally, we used our design for controlling the adsorption of inorganic nanoparticles. The selective adsorption of gold nanoparticles and their surface aggregation on patterned surface are controlled by positively charged gold nanoparticles and PAA arms (Figure 2-7). Surface composition of Y-shaped brush layers, which is a

critical factor in tuning nanoparticles adsorption, undergoes significant surface reorganization on treatment with selective solvents (See Chapter 6).

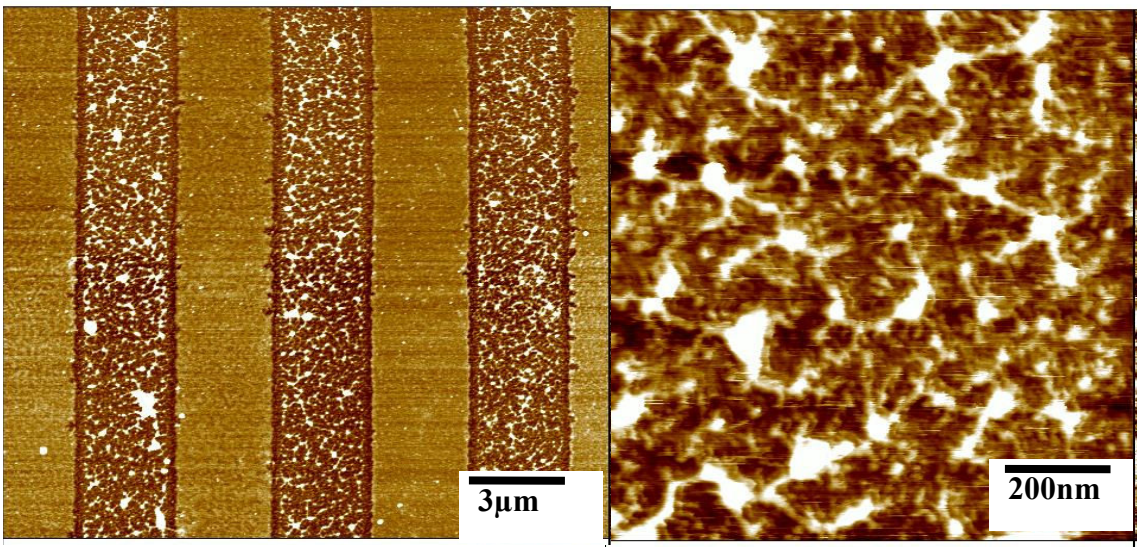

Figure 2-9. AFM image of micropatterned surfaces with adsorbed gold nanoparticles (left) and high-resolution AFM images (right).

2.3.2. Polymer-silicon microcantilever as thermal IR sensors

The highly sensitive microcantilever sensor arrays have a broad range of applicability for detecting physical phenomena and specific chemical and biological interactions which can transduce a number of different stimuli such as atomic forces, temperature/heat, medium viscoelasticity, mass, stress and magnetic field.[45, 46, 47] A decade ago, it had be suggested that standard AFM microcantilever could function as a microcalorimeter, offering femtojoule sensitivity with a new scientific and technical application emerging.[48,49] The main motivation for the application of a microcantilever sensor is miniature dimension, high sensitivity, and direct transduction. Currently, the challenge lies in optimizing cantilever sensors to improve their sensitivity and make possible commercial applications. Optimization of microcantilever sensors can be achieved through suitable design, responsive coating (nanostructured coatings), and readout schemes. Depending on the type of coating materials, microcantilevers can

essentially become a universal platform for detecting a multitude of chemicals, biomolecules, organisms and changes of temperature. [50, 51]

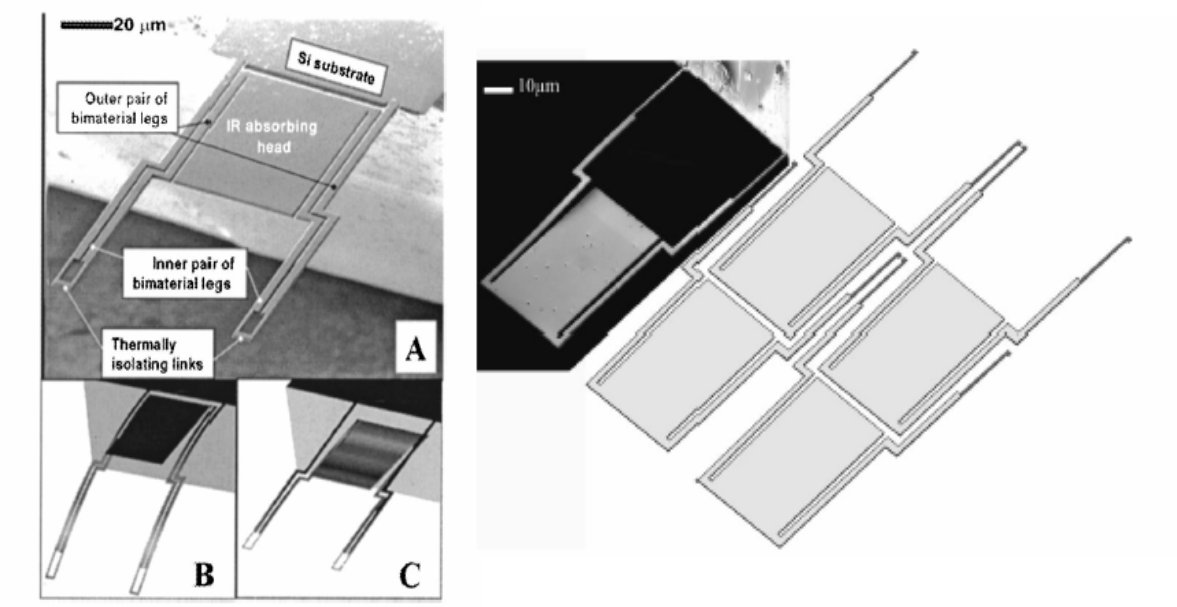

Figure 2-10. Uncooled microcantilever thermal detector.[116, 120]

At present, different techniques have been reported to modify silicon-based microcantilevers with an organic or polymer coating fabricated for different sensing capabilities. For example, microcantilever modification was conducted by using spin coated layers,[52] SAMs,[53] LbL assembly[54, 55], hydrogel layers[56, 57] and polymer brush layers.[58] Microcantilever sensors have been recently introduced for thermal detection and imaging.[59,60,61,62,63] The design uses the well-known phenomenon of temperature-induced bending of bilayered beams composed of two materials with very different thermal expansion coefficients. The most common approach utilizes a silicon substrate with a metallic coating (bimetallic beams), which is usually gold or aluminum, as these materials are readily processable with microfabrication assemblies.[64, 65] Thermally induced stresses result in reversible bending of microcantilevers with measurements of cantilever deflections detected via various readout schemes such as laser beam deflection. These bimetallic microcantilevers are considered to be a promising platform for the microfabrication of highly sensitive uncooled IR detectors.

With sensitive optical or electrostatic readouts, the microcantilever-based devices can show resolution of several tens of mK with thermal sensitivity, S, (beam deflection per K) reaching a hundred nm/K for microcantilevers with the length around several hundred microns. These characteristics are sufficient for the fabrication of medium resolution uncooled IR imaging arrays with promising spatial, thermal, and temporal characteristics.[66,67] However, to make significant progress in the miniaturization of these devices and, most importantly, increasing their sensitivity below the limits of modern cooled solid state sensors (below 10 mK), the thermal sensitivity should be increased significantly. Considering that the difference of thermal expansion coefficients between the two materials constituting the ceramic-metal is limited and the thickness of the metal layer cannot be increased significantly without compromising the sensitivity and uniformity, other materials should be explored in order to enhance the thermal bending ability of beam microstructures.

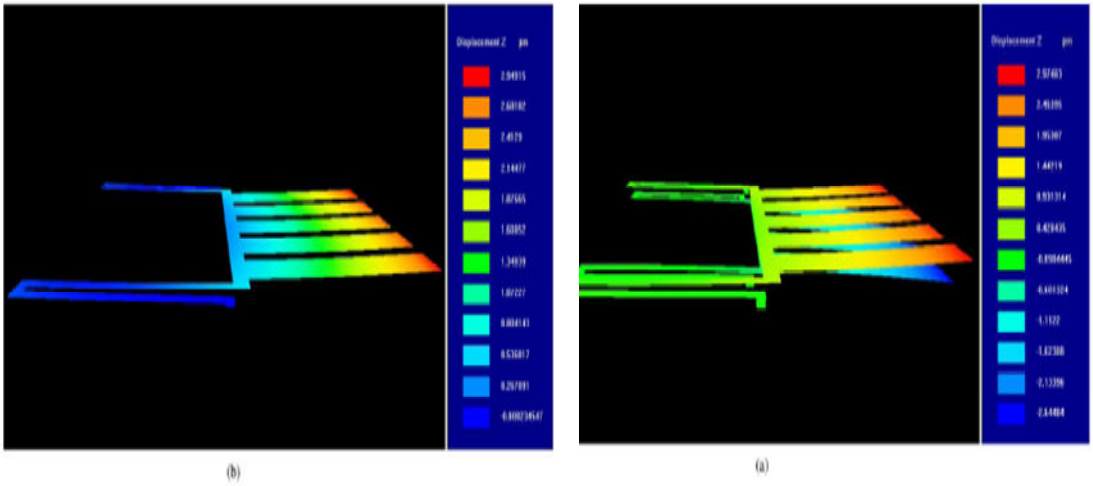

Figure 2-11. Simulation of double- and single-cantilever microbolometer structures upon IR irradiation. (a) Double-cantilever: z = 0.452 _m/K, NETD = 8.6 mK. (b) Single-cantilever: z = 0.227 _m/K, NETD = 13 mK.[68]

Polymers as layers with high thermal expansion have been considered, but they are not easy to apply because of their low mechanical strength and poor chemical affinity to metal surfaces. Moreover, polymer modification of cantilevers leads to damage, and large stresses within the polymer-silicon beams. Previous studies of patterned organic films on microcantilevers provide a variety of tailored properties that could be used for miniaturizing and integrating chemical and physical processes. [69,70]

Development of thermally responsive nanocomposite coatings

The research goal here was to fabricate an optimal compliant polymer or nanocomposite film (multilayered, incorporated nanoparticles or nanotubes) that can greatly enhance the sensitivity of microcantilever. To produce an "optimal" layer, a numbers of parameters should be adjusted. We focused on designing and testing a new generation of enhanced layered microcantilevers with the topmost polymer layer to be strengthened by adding silver nanoparticles and carbon nanotubes with different types of surface distribution. To design a thermally-sensitive microcantilever, we explored a novel strategy by fabricating trilayer ceramic-metal-polymer surfaces with enhanced thermal bending ability by adding the topmost strong polymer nanocomposite layer chemically grafted to the original silicon nitride-gold microcantilever.(Figure 2-12) It is important to notice that the polymer layer is strongly adsorbed only on one side of cantilever to ensure the performance of the bending properties.

The first stage was to produce functional SAMs on gold surface by using a bi-functional linker. The bi-functional linker with amine and thiol terminated molecules (cysteamine) created a covalent bond with a gold surface(Figure 2-12a). The second stage was to use bi-functional linker for grafting of mono- and bi-functionalized polymers by using the spin coating method (Figure 2-12b). The important factor here was not only to choose the two materials with as large as possible mismatch in thermal expansion coefficients but also to consider the polymer materials with high modulus to be able to bend the cantilever. We selected carboxyl-terminated mono- and bi-functionalized PS to attach and create a covalent bond with the amine-functional gold surface. The third stage

was to incorporate different nanoparticles and carbon nanotubes into the polymer layers to increase mechanical strength of these polymer layers (Figure 2-12c). Nanoparticles and carbon nanotube was modified with carboxyl or amino functional groups to facilitate absorption on the polymer surface before they were embedded into layers. The eventual approach is to build up LBL assembly on a gold surface presented in Figure 2-12.

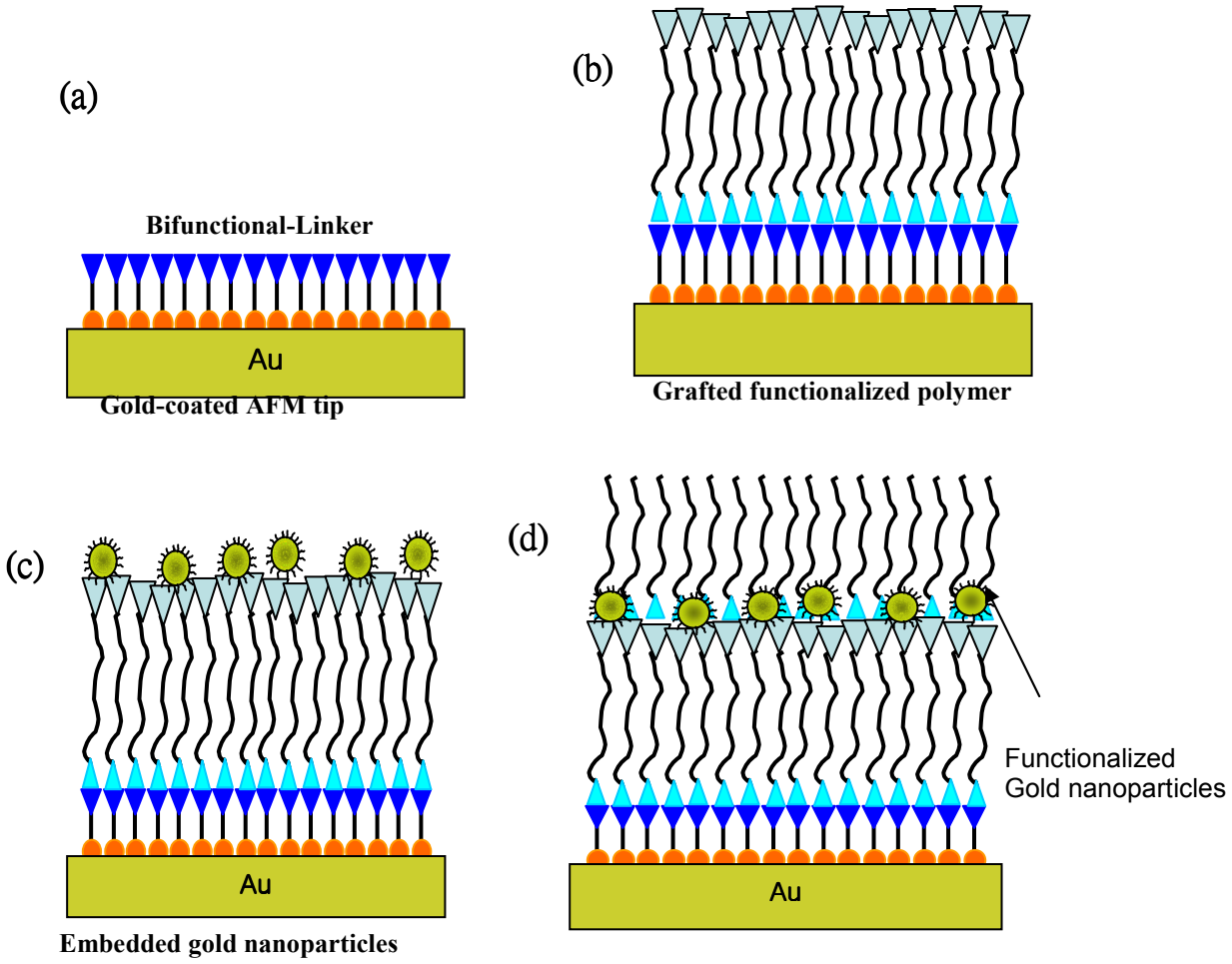

Figure 2-12. A schematic of build up layer-by-layer assembly on a gold coated AFM tip.

Topmost polymer nanocomposite layer has a thermal expansion about two orders of magnitude higher than that at the gold layer in conjunction with a low thermal conductivity. Moreover, polymer materials are in the IR absorption (increase thermal

sensitivity) window and highly polar which facilitates the interaction between polymer and incorporated nano-fillers.

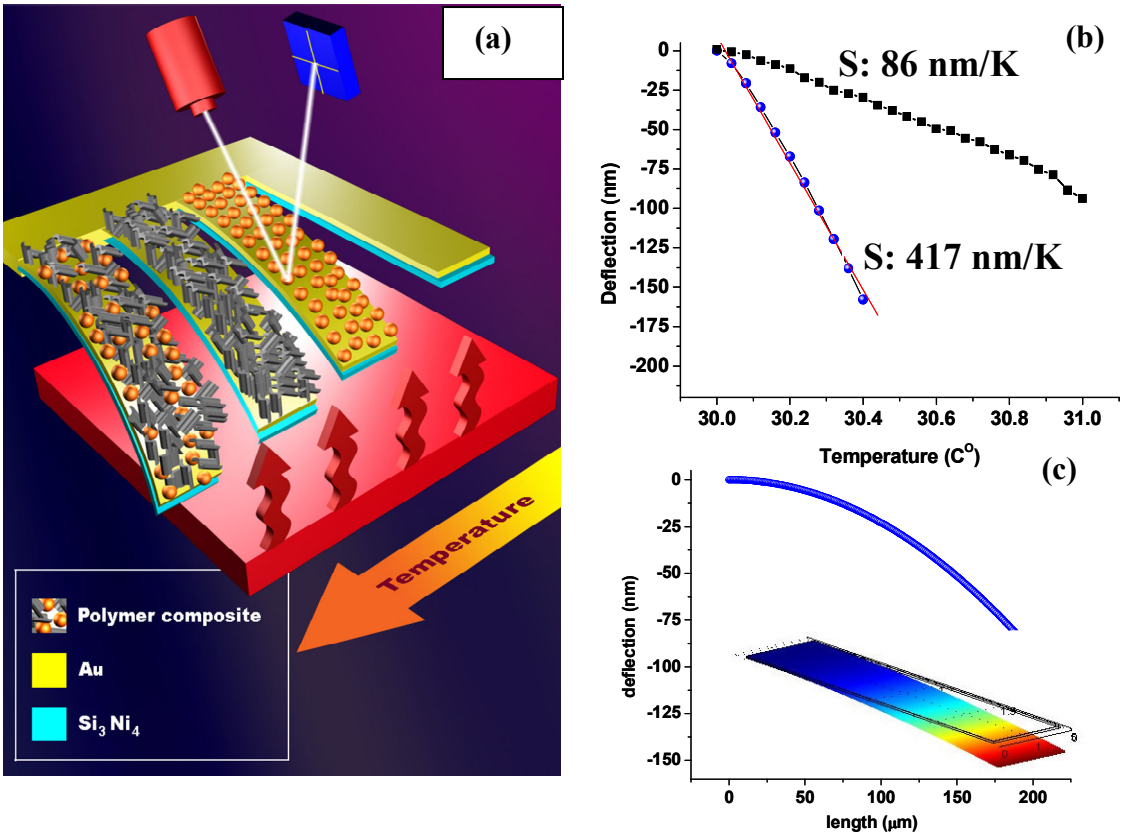

Figure 2-13. (a) A schematics of a microcantilevers with optical readout and trilayered composition. (b)Temperature deflection for microcantilevers (modified with polymer composite-single wall carbon nanotube and silver nanoparticles), squares-unmodified gold-ceramic microntilevers, circles-modified microcantilevers with topmost layers, (c) the simulated profile of the silicon nitride-gold cantilever for 1°C temperature increase and FEA data e for the bent microcantilever.

The results showed polymer layers reinforced with carbon nanotubes and metal nanoparticles provided high thermal stresses that resulted in significant (up to fourfold) increase of thermal sensitivity as compared with conventional ceramic-metal bilayered

microcantilevers. These trilayered polymer-metal-ceramic microcantilevers with dramatically enhanced thermal sensitivity can serve as basis for the next generation of un-cooled IR sensor arrays with the thermal and spatial resolution manifold higher than those currently available.

2.3.3. Nanobelt/wires based photosensing elements

Nanowires (NWs) and nanobelts (NBs) present an essential and broad range of one-dimensional nanostructure at the forefront of nanoscience and nanotechnology. NWs and NBs are typically single-crystalline, highly anisotropic, semiconducting, insulating and /or metallic nanostructures that result from rapid growth along one direction. ZnO exhibits the most diverse and abundant configurations of nanostructures known so far, such as hierarchical nanostructures [71], [72] nanobelts, [73] nanosprings, [74] nanorings, [75] nanobows,[76] and nanohelices.[77] Due to semiconducting and piezoelectric properties of ZnO, numerous studies have demonstrated potential applications in electronics and optoelectronics based on ZnO nanostructures, such as optically pumped nanolaser,[78] nanogenerator, [79] acoustic resonator, [80] piezoelectric gated diode, [81] field-emitter, [82] photodiode, [83] and photoconductor. [84, 85] In particular, ZnO NW photodetetectors and optical switches have been a subject of extensive investigation.[86,87] The conductivity of the ZnO NBs/NWs is extremely sensitive to ultraviolet light exposure. Because of its wide band gap (Eg=3.3 eV) and long lifetime photocarriers, low cost ZnO is attractive feature for the ultraviolet photodetector.

The observed photoconductivity is primarily attributed to the adsorption or desorption of oxygen at the surface of ZnO.[87] The light induced conductivity increase allows to reversibly switch the NWs/NWs between “OFF” and “ON” state (Figure 2-15).[88] To date, despite a great deal of research on the photon sensing using nanowires, only a few of them reporting the improvement of photoresponse of NWs/NBs-based photoconductor.[25,89]

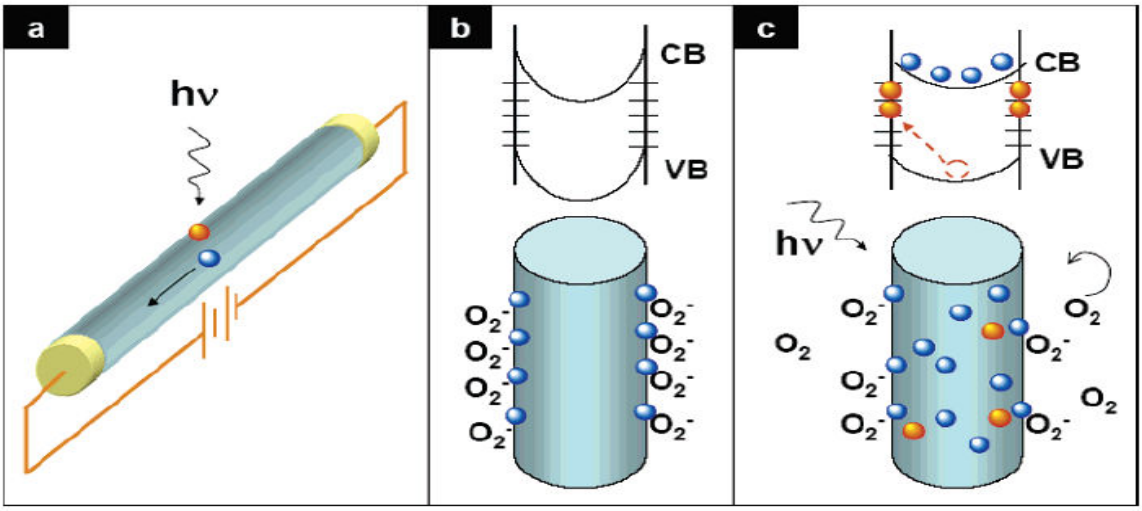

Figure 2-14 Photoconduction in NW photodetectors. (a) Photoconduction in NW photodetectors. (a) Schematic of a NW photoconductor. Upon illumination with photon energy above *E*g, electron-hole pairs are generated and holes are readily trapped at the surface. Under an applied electric field, the unpaired electrons are collected at the anode, which leads to the increase in conductivity. (b and c) Trapping and photoconduction mechanism in ZnO NWs: the top drawing in (b) shows the schematic of the energy band diagrams of a NW in dark, indicating band-bending and surface trap states. VB and CB are the valence and conduction band, respectively. The bottom drawing shows oxygen molecules adsorbed at the NW surface that capture the free electron present in the n-type semiconductor forming a low-conductivity depletion layer near the surface. (c) Under UV illumination, photogenerated holes migrate to the surface and are trapped, leaving behind unpaired electrons in the NW that contribute to the photocurrent. In ZnO NWs, the lifetime of the unpaired electrons is further increased by oxygen molecules desorption from the surface when holes neutralize the oxygen ions.[87]

Development of inorganic–organic hybrid ZnO nanobelt (NB) for UV photosensing.

In this study, we design and fabricate a bilayer polymer/ZnO photoconductor based on ZnO NBs. For NB photodetector design, the synthesized ZnO nanobelts are transferred from the Al_2O_3 substrate to prepatterned Ti/Au electrodes by touching the NB

sample with the electrodes. A single ZnO NB device lying across two electrodes could be achieved easily using this method. To reduce the contact resistance, focused ion beam (FIB) microscopy is employed to deposit conducting mixture of Pt on the contacts between ZnO and Au/Ti electrodes. The prepatterned Au/Ti electrodes for contacting probes of current-voltage (I-V) measurements were fabricated on 100 nm Si_3N_4/Si wafer through a typical process in the literature.[26] Acrylonitrile PECVD was used to deposit gas phase organic monomers on suitable zinc oxide nanobelt. The PECVD chamber was built and housed at Wright Patterson Air Force Base, Ohio. The oxygen plasma treatment was carried out for eliminating the surface contamination of ZnO NB device before depositing PP-AN using PECVD.

Coating of PP-AN (thickness less than 300nm) on the ZnO NB increased its photon conductivity by a factor of 750 in comparison to that of a bare ZnO NB (Figure 2-15). This effect is suggested as a consequence of the high efficiency of exciton dissociation under UV illumination due to efficient electron transfer from valence band of ZnO NB to the PP-AN and then back to the conduction band of ZnO. Emission spectrum of the PP-AN films shows good agreement with the exciton dissociation model that is electron excition from the ground state to the excited state. The rectangular shape of polymer/ZnO nanobelt photosensor was fabricated by exploiting plasma enhanced chemical vapor deposition (PECVD). The photosensing mechanism concluded a consequence of the efficient exciton dissociation under UV illumination due to enhanced electron transfer from valence band of ZnO NB to the photon-excited plasma-polyacrylonitrle (PP-AN) rich on double and triple carbon-nitrogen bonds and then back to the conduction band of ZnO. The study of the PP-AN-functionalized NBs presents a simple and cost-effective approach for significant improving the performance of oxide NW/NB-based devices for photon detection, possibly leading to a motivation for studying the optoelectronic properties of inorganic–organic hybrid nanomaterials.

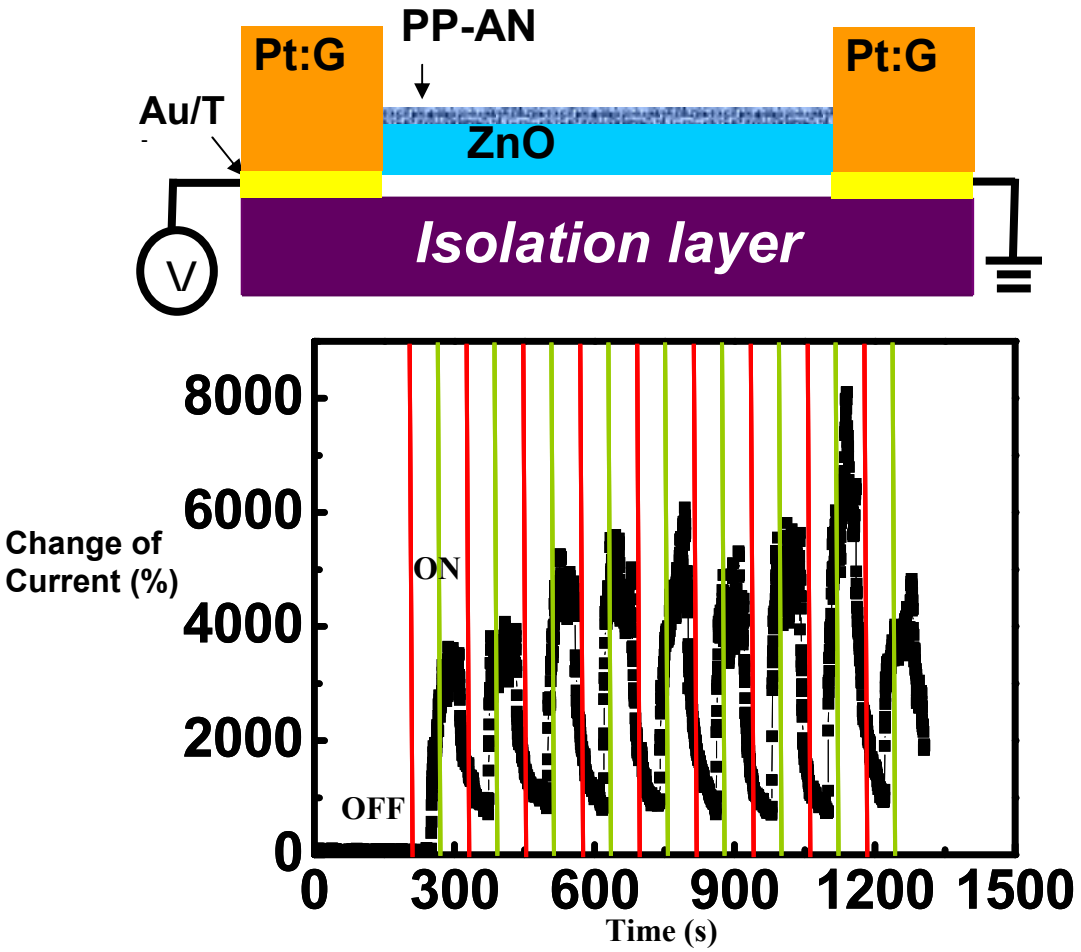

Figure 2-15. The schematic diagram of PP-AN/ZnO NB device (top) and reversible switching of a of PP-AN/ZnO NB between low and high conductivity states when the UV-lamp on and off (bottom).

2.3.3. LBL assembled thin films with optical grating 3D structure

Precise assembly of nanostructured materials into two and three dimensional periodic microscopic arrays were achieved by employing various assembling technologies such as microparticle self-organization,[90] photolithography,[91] holographic lithography,[92] selective chemical etching,[93] ink printing,[94] laser-based polymerization,[95] selective responsive grafting[1], and inversion of bilayers.[96] Soft lithography, such as microcontact printing has been widely applied to tackle this challenge in few steps, with a

submicron resolution, and at low cost.[97,98,99] It has been demonstrated that the most popular fabrication of well-defined nanostructured materials with assembly can be combined with photolithography and microprinting to fabricate complex 2D and 3D structures with modulated distribution of different components.[100,101,102] Examples of micropatterned assembly of nanoparticles, microchannels, antireflective coatings, and Raman arrays have already reported.[103,104,105,106,107,108]

LbL assembly is based on the noncovalent interactions for alternating absorption of multiply charged polyelectrolyte (cationic and anionic species).[109,110] As compared to traditional responsive materials, LbL multilayers allow synergistic interaction between two molecules or enhances organic inorganic interfacial contact. Thus, they have the advantage to highly tailored nanoscale response with a broad range of functional groups incorporated in the layer structure.[111] In addition, LbL systems can make outstanding hosts for optical[112,113], electrical, and electrochemically active material systems which have the ability to incorporate a number of different materials.

Recent investigations of the preparation of *free-standing* LbL films open the door for exploitation of these assemblies as ultrathin membranes with a variety of possible applications (Figure 2-16).[114,115] Free standing membranes can be produced in various ways such as casting,[116] spin-coating,[117] polyelectrolyte multilayer formation using sacrificial layers or dissolvable substrates, polymerization of LB layers, and crosslinking of polymer precursors at an air-water interface. It is worth mentioning that using spin coating results in denser packing of the macromolecules and fewer defects of the multilayer films. The spin-coating method improves the load transfer within the films due to the shear forces created during the spin-coating process and stretch the polymer molecules. Because of the different methods of fabrication, free standing LbL multilayers can have various shapes for example microcapsules[118,119], microtubles,[120] microcubic,[121] microcantilever[122] and planar films.[123] However fabrication of free standing multilayer films has several technical challenges due to their poor mechanical stability, making them less likely candidates for applying on large-scale sensor device

and long-lasting multilayers. For this reason, new design of free standing LbL nanocomposite multilayers should be thought to overcome in more applicable fields.

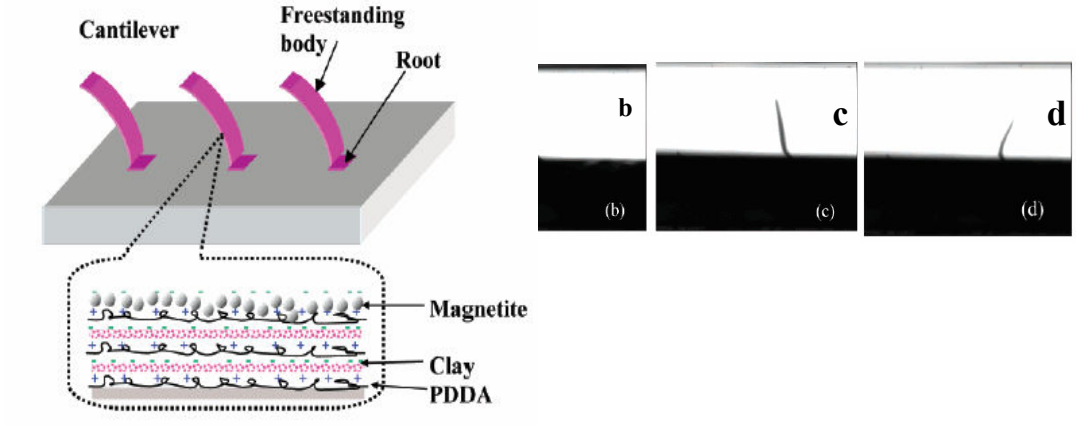

Figure 2-16. Temperature responsive free-standing LbL nanocomposite multilayer membrane[122]

The critical point here is selection of sacrificial layers and solvent which will be related to release process. We attempt to build multilayers of polyelectrolyte/conjugated polymer (poly(2,5-methoxy-propyloxysulfonate phenylene vinylene, MPS-PPV, Dr. Z. Lin, Iowa State University) (Figure 2-17) which is water soluble and can be optically and electrically active with molecular-level control over functionality such as photoluminescence (PL), nonlinear-optical properties, and energy transfer.

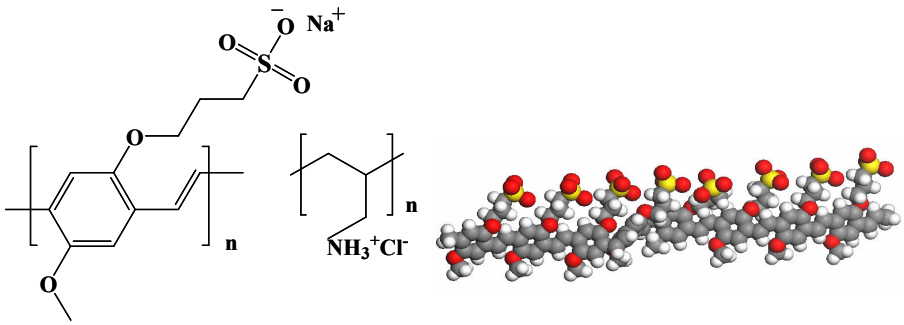

Figure 2-17. Chemical structure of conjugated polymer (poly(2,5-methoxy-propyloxysulfonate phenylene vinylene, MPS-PPV)

We reported on the fabrication of freely suspended polymeric LbL films without any nanofillers with a truly nanoscale thickness (below 20 nm) which demonstrated very robust mechanical properties. For this fabrication, we selected a water soluble conjugated polymer MPS-PPV, (Figure 2-17) which is essentially a rod-like chain with much stronger mechanical properties than usual flexible-chain polyelectrolyte exploited for previous LbL assembly of free-standing films. Moreover, the conjugated nature of the MPS-PPV chains brings intense fluorescent response, which is extremely stable even under large mechanical deformations. These films could be transferred in large pieces to cover an array of holes with different diameters and showed relatively uniform optical appearance. The surface of SA-LbL films was relatively uniform with developed grainy morphology and a microroughness (within 1 μm^2 surface area) below 5 nm which is a typical value for LbL films from conjugated polymers (Figure 2-18). The average thickness of $(MPS\text{-}PPV/PAH)_5$, the thinnest film discussed here in great detail, was 18 ± 2 nm

At next stage of this research, we suggest an easy economical fabrication method by combing top down and bottom up approach to assemble 3D free standing sculptured LbL film. It is well suited to the production of freely standing three dimensional structures with nanometer thickness and a micrometer periodicity (Figure 2-19). First, sacrificial PS micropatterns template were obtained by use of Capillary Transfer Lithography (CTL).[124] A PDMS stamp with the appropriate pattern was brought into conformal contact with the PS on the PDMS substrate and when the PDMS stamp was detached from the PDMS substrate, the patterned polymer layer was trapped inside the recessed regions of the PDMS stamp. The PS pattern formed in this way was then immediately transferred onto sacrificial PS layer by conformal contact of the PDMS mold (Figure 2-19). Finally, LbL multilayers were prepared on PS sacrificial layer by the spin-assisted LbL (SA-LbL) method. Droplets (150 μl) of 0.2% (w/w) MPS-PPV and PAH layers were deposited in an alternating manner. This procedure was repeated until the needed number of polymer bilayers, *n*, was achieved.

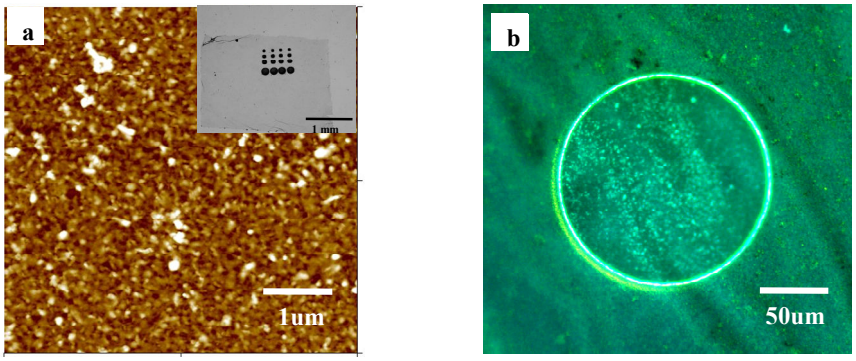

Figure 2-18. (a) AFM topographical image of (MPS-PPV/PAH)$_5$ film (z range is 80 nm) and an optical image of a whole free standing film on an array of holes (inset). (b) Fluorescence image of freely suspended film on a 150 um diameter hole.

The freely suspended LBL multilayer film is shown in Figure 2-20. By dissolving sacrificial PS structured layer, LbL film is freely suspend and enable to transfer on a real sensor device. Tetrahydrofuran (THF) solution was used to dissolve the sacrificial CA layer and result in the release of the LBL multilayer films. The LBL multilayer films were then transferred to Nanopure water where it can then be picked up on a silicon substrate or at the center of microfabrication device.

In these freely-suspended 3D LbL films, the effective modulation of the refractive properties is caused by the topological variation of the local film shape, thus representing a purely structural color effect. A simple and economical spin-assisted LbL deposition on a sacrificial microimprinted substrate was employed here for conjugated polyelectrolytes to generate robust, free-standing sculptured LbL structure with the effective thickness of 60 nm and the 160-nm peak-to-peak modulation of square lattice with 2.5-μm periodicity (Figure 2-20). These films demonstrated efficient optical grating properties and bright structural colors in a reflective mode controlled by the in-plane spacing and the angle of incidence.

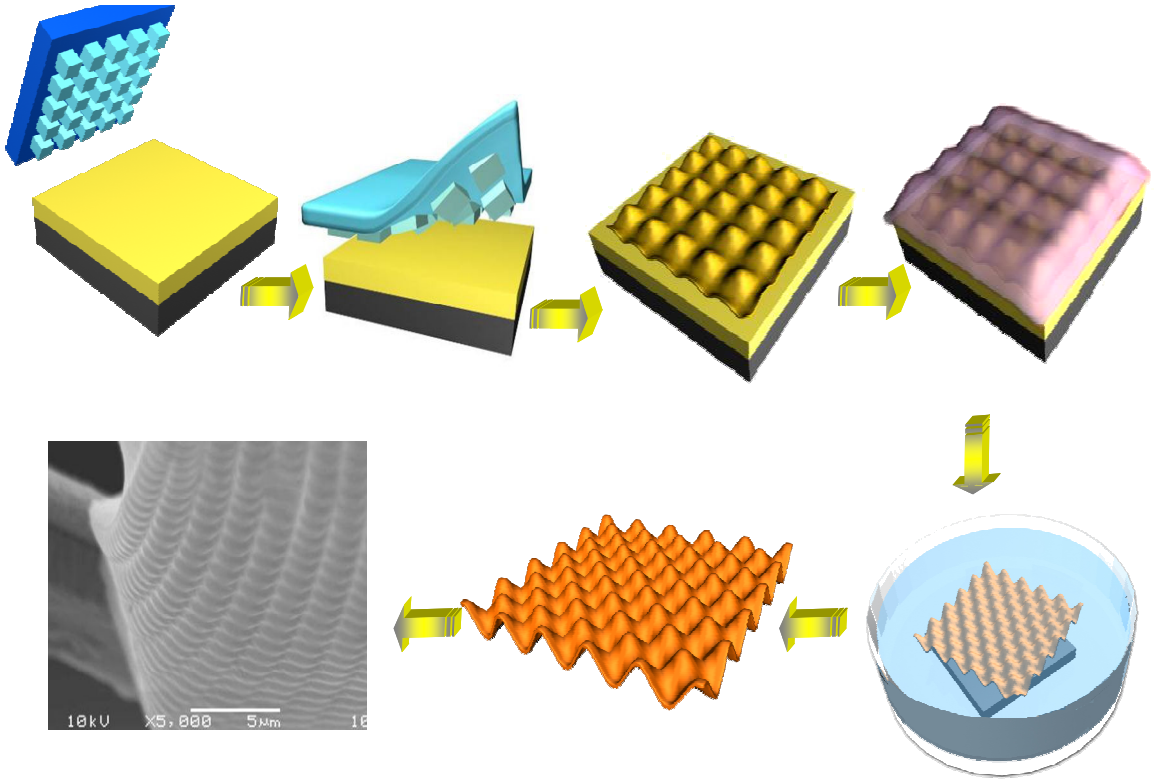

Figure 2-19. Schematic illustration of the route for the fabrication of sculptured LbL films by combining microstamping and sacrificial templates and SEM image of the freely standing film with a square pattern.

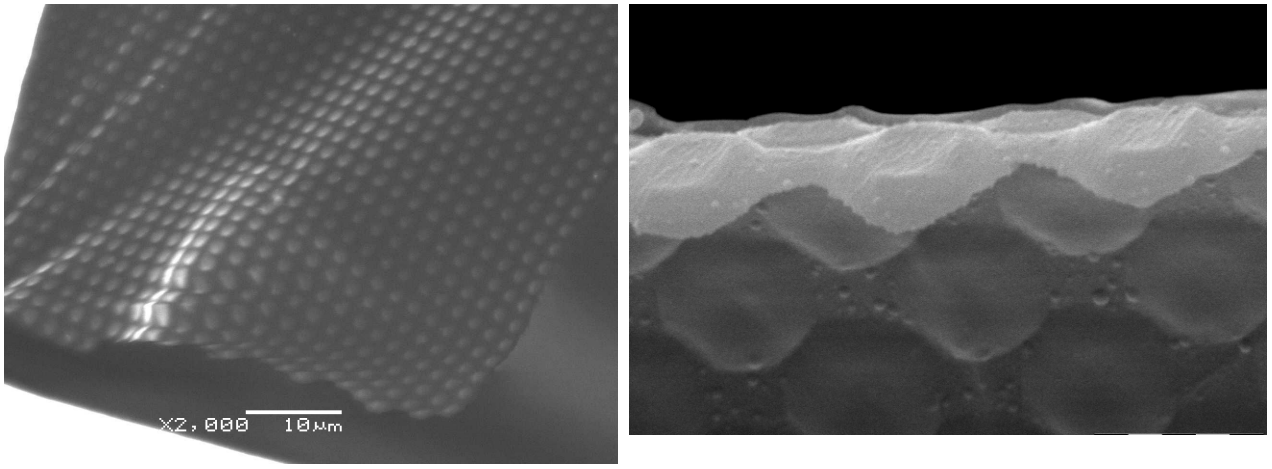

Figure 2-20 SEM image of the piece of the 3D LbL film with characteristic fracturing

Bright coloration was observed for sculptured LbL film transferred on a silicon wafer in a reflection mode in contrast to planar LB films which show weak brownish color due to absorption of conjugated backbones. Our experiments showed that the white light can be reflected by 3D LbL with the intense color changing from blue to red while adjusting the view angle (Figure 2-21). The intensity of the color is remarkable considering that the physical thickness of the LbL film is only 60 nm. Correspondingly, the 2D diffraction pattern is observed under an incident illumination from a He-Ne laser (λ = 632 nm). Bright diffraction spots forming a square lattice can be seen beyond the third order (Figure 2-21b). The diffraction pattern produced by 3D LbL film follows a Fraunhofer diffraction law with positions of individual spots in a reciprocal space defined by the symmetry and spacing of the modulations in real space.[125] Thus, from multiple diffraction orders (m) we estimated the expected distribution of the diffraction spots taking into account the known spacing of the square modulations of 2.4 μm. Under this assumption, excellent coincidence was observed between the experimental positions measured and those estimated from the spacing of the LbL modulations as demonstrated for the (01) direction (Figure 2-21c).

Thus, the modulated refractive properties achieved by the topological variation of the LbL film shape can generate intense structural color effect with bright structural colors and optical grating properties, a phenomenon which can be of interest for light-controlling polymeric microdevices. Overall, this study shows an interesting potential in LbL technology to generate optically-relevant nanostructured materials with the ability to control visible light diffraction beyond one-dimensional modulation of the refractive properties reported before

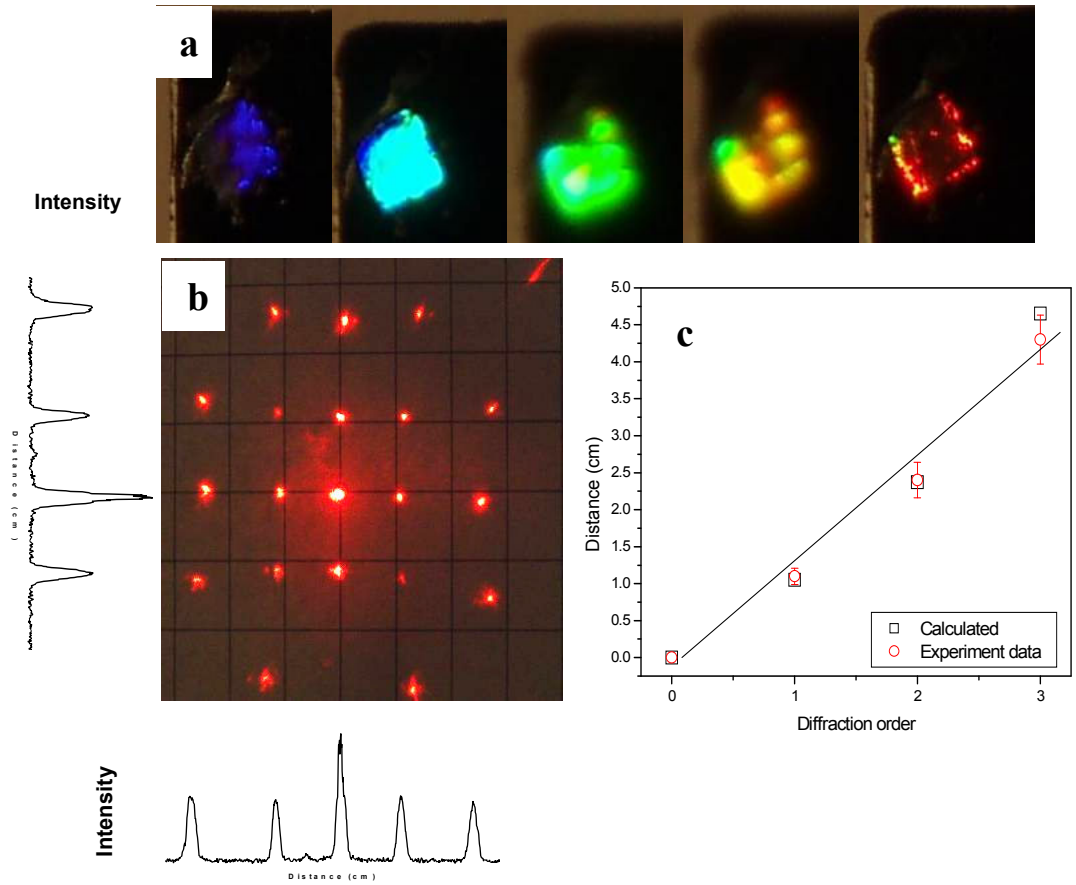

Figure 2-21. a) Sculptured LbL film with different structural colors generated at different viewing angles. b) The diffraction pattern produced by the LbL film in the reflection mode with intensity versus distance profiles. c) The calculated and experimental positions of diffraction spots of different orders along the (01) direction.

CHAPTER 3.

EXPERIMENTAL

3.1 General Consideration

In this work, polymer layers are prepare on two substrates: I. Highly polished single-crystal silicon wafers of {100} orientation cut in pieces of approximately 1.5 × 2 cm^2 before modification. II. Commercially available rectangular and V-shaped Si_3N_4-Au cantilevers with a 60 nm gold layer sputtered on a 600 nm thick silicon nitride beam (Veeco, CA). Surface modification and preparation consists of three stages: (1) surface cleaning (2) SAM formation and (3) polymer layer formation. The silicon wafers are cleaned in a hot piranha solution (30% H_2O_2, 70% concentrated sulfuric acid) and rinsed with nanopure water copiously.[126] The AFM cantilevers are cleaned in a mixture of methanol and chloroform. SAMs are prepared in glove box with less than 1% humidity. For patterned surfaces, preparation of the PDMS stamps and patterning SAMs monolayer is prepared. All sample preparations were performed inside a Cleanroom 100 facility (Laminare Corporation).

Characterization

Surface morphology and micromechanical properties with AFM

Surface morphology of the polymer film was studied on Dimension 3000 and Multimode IIIa microscopes (Digital Instrument, Inc., Santa Barbara). Silicon or silicon nitride tips were used with radius around 20-40 nm and spring constant range of 0.01-50 N/m. Scanning rate was in the range of 0.3-2 Hz depending upon loading condition and scanning size range is from 30 μm to 300 nm. In this research, scanning was done both in ambient and fluid conditions. Scanning in fluid was conducted in both tapping mode and contact mode. Scanning under fluid gives great advantage of image polymer brush in

their native state while imaging them under different solvents. The ability to image solid surfaces in a liquid medium makes AFM an attractive tool in the study of liquid-solid interfacial phenomena. Scanning in fluid minimizes forced exerted on the sample by the tip, in addition to eliminating capillary and adhesion force at the tip-sample joint.

AFM was also be used here to study mechanical, adhesive, and friction properties of the surface of material. Force volume mode allows for the micromapping of mechanical properties of polymer surface with nanometer scale resolution, meanwhile obtaining topograpgical information.[127] Force volume mode which utilize the collection of the force distance curve (FDC) over selected surface area, was used for micromechanical analysis (MMA) of polymer layer.[128] FDC are plots of the deflection of the cantilever versus the extension of the piezoelectric scanner, knowing the cantilever spring constant the deflection can then be converted into force (Figure 3-1).

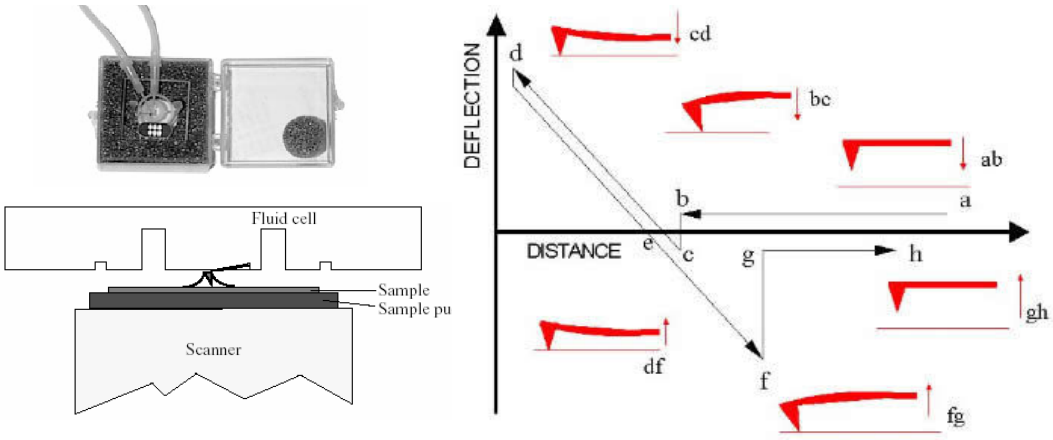

Figure 3-1. AFM fluid cell (top) and the liquid meniscus between tip and sample in fluid (left). Components of an FDC (right): in bc, the "jump to contact", is often due to capillary forces from the moisture layer that covers the tip and the sample surface. Segment fg shows the jump of the cantilever away from the surface, when the cantilever force exceeds the adhesive forces. The force of point f is the total adhesive force between the probe and the sample. Segment a to d is called the first half cycle of the curve while segment d to h is the second half cycle[129]

These curves can be used to measure the vertical force that the tip applies to the sample surface and to study the surface properties of the sample. In this work, data were processed using an MMA software developed in our lab which provides means for calculation of localized elastic modulus, depth profile of elastic modulus, reduced adhesive force, and surface histograms of elastic modulus and adhesive force. Thickness evaluation is also measured with AFM by "scratch" test. Scratches are generated either by stiffness tip multiple scanning with high normal load or with a sharp steel needle at different loads under contact mode. The scratch on the surface was clearly visible in the AFM image to obtain the depth of the scratch taken after the test.

Surface morphology with SEM

SEM was conducted in secondary electron scattering mode at 5 keV (JEOL JSM-6060LV and JEOL 5800LV) and LEO 1530 field emission microscopies. SEM was used to evaluate film morphologies and film thickness.

Photoluminescence spectra and UV-visible spectra

Optical microscopy images of polymers surfaces were obtained using a Leica DM4000 fluorescent microscope equipped with a 5M digital camera. [130] . Photoluminescence spectra were taken on a LEICA DM 4000M microscope and attached CRAIC QDI202 microscopic spectrophotometer. The samples were excited at 365 nm and the emission spectra were collected within 400 - 1000 nm. The independent UV-visible spectra were obtained with a Shimadzu-1601 spectrometer.

Contact Angle Measurement

The static contact angles measurement were conducted with a sessile drop method, measured directly by using a custom-designed optical microscope. For drops that bead up, the contact angle provides a qualitative analysis of the surface energy of the polymer film. Contact angles droplets (1.5~2µl) of Nanopure water were placed randomly on surface

and determined within 1 min after deposition. A microscope interfaced monitor the shape of drop and the contact angle was measure on monitor screen. All reported values are averages from at least five measurements.

Ellipsometry

Ellipsometry (a COMPEL Automatic Ellipsometer (InOmTech, Inc.)) was used to evaluate polymer layer thickness with an angle of incidence 70 ° by changing polarization of light reflected off a surface. The index of refraction for each layer was considered to be constant as "bulk" values.[131] All reported thickness values were averaged over six measurements gathered from different locations.[132]

Sensitivity measurements and thermal tuning

The thermal sensitivity of microcantilevers was measured by utilizing the AFM optical detection system. The microcantilevers with spring constant 0.016-0.031 N/m was brought into within 1μm of the surface of the thermal stage (a Peltier heater, 1x1 cm, ±0.001^{o}C). A laser beam will be focus on the end of the microcantilever and reflected onto the AFM photodiode detector. The deflection of microcantilever is obtained with precision of 0.3 nm (limited by the amplitude of thermal vibrations) after the sensitivity of the photodiode detector of the AFM was independently calibrated. At each temperature step (usually, 0.04-0.05C^{o}), the microcantilevers were kept for about a minute to reach an equilibrium.

The cantilever spring constants were measured using a Multimode AFM equipped with a Picoforce module, which used the well-known thermal tuning.[133] For each measurement the tip was allowed to equilibrate before the photodetector was carefully calibrated. Then, after taking precautions to minimize external noise, the photodetector signal is sampled at frequencies from 0 to 35 kHz. The signal will be filtered with a lock-in amplifier to optimize the signal to noise ratio. Then using the Picoforce software a Lorentzian equation was used to fit the power vs. frequency curves and to obtain the spring constant value.

Finite Element Analysis

Theoretical stresses for the deflected cantilever have been estimated with Finite Element Analysis (FEA) using Structural Mechanics module of a commercial package COMSOL Multiphysics 3.2. The model accounts the material properties including Poisson's ratio, elastic modulus, thermal expansion coefficient, and density.[134]

3.2 References

1 I. Luzinov, S. Minko, V. V. Tsukruk, *Prog. Polym. Sci.* **2004**, *29*, 635.

2 R. Israels, F. A. M. Leermakers, G. J. Fleer, E. B. Zhulina, *Macromolecules* **1994**, *27*, 3249.

3 M. Lee, J.-W, Kim, Y.-S Yoo, S. Peleshanko, K. Larson, D. Vaknin, S. Markutsya, V. V. Tsukruk, *J. Am. Chem. Soc.* **2002,** *124*, 9121.

4 Y. G. Takei, T. Aoki, K. Sanui, N. Ogata, Y. Sakurai, T. Okanao, *Macromolecules* **1994**, *27*, 6163.

5 R. Hall, M. Hara, W. Knoll, *Langmuir* **1999**, *612,* 2551. K. Ichimura, S.-K Oh, M. Nakagawa, *Science* **2000**, *288*, 1624.

6 L. Lahann, S. Mitragotri, T.-N. Trsn, H. Kaido, J. Dundaram, I. S. Choi, S. Hoffer, G. A. Somorjai, R. Langer, *Science* **2003,** 299, 371.

7. P. Auroy, L. Auvray, L. Leger, *Phys. Rev. Lett.* **1991**, *66*, 719.

8 U. Raviv, R. Tadmor, J. Klein, *J. Phys. Chem. B* **2001**, *105*, 8125.

9 G. S. Grest, M. Murat, *Macromolecules* **1993**, *26*, 3108.

10 R. Blossey, *Nat. Mater.* **2003**, *2*, 301.

11 N. Nath, A. Chilkoti, *Adv. Mater.* **2002**, *14*, 1243.

12 A. Lafuma, D. Quere, *Nat. Mater.* **2003**, *2*, 457.

13 D. M. Jones, J. R. Smith, W. T. S. Huck, C. Alexander, *Adv. Mater.* **2002**, *14*, 1130.

14 V. V. Tsukruk, *Adv. Mater.* **2001**, *13*, 95.

15 J. Lahann, S. Mitragotri, T. N. Tran, H. Kaido, J. Sundaram, I. S. Choi, S. Hoffer, G. A. Somorjai, R. Langer, *Science* **2003**, *299*, 371.

16 M. Lemieux, D. Usov, S. Minko, M. Stamm, H. Shulha, V. V. Tsukruk, *Macromolecules* **2003**, *36*, 7244.

17 G. Gorodyska, A. Kiriy, S. Minko, C. Tsitsilianis, M. Stamm, *Nano Lett* **2003**, *3*, 365.

18 S. T. Selvan, J. P. Spatz, H. A. Klok, M. Moller, *Adv Mater* **1998**, *10*, 132

19 V. V. Tsukruk, K. Genson, S. Peleshanko, S. Markutsya, M. Lee, Y. S. Yoo, *Langmuir* **2003**, *19*, 495.

20 V. V. Tsukruk, V. N. Bliznyuk, *Prog Polym Sci* **1997**, *22*, 1089.

21 K. Ichimura, S. K. Oh, M. Nakagawa, *Science* **2000**, *288*, 1624.

22 A. Sidorenko, C. Houphouet-Boigny, O. Villavicencio, D. V. McGrath, V. V. Tsukruk, *Thin Solid Films* **2002**, *410*, 147.

23 U. Raviv, R. Tadmor, J. Klein, *J Phys Chem B* **2001**, *105*, 812.

24 F. Zhou, H. Hu, B. Yu, V. L. Osborne, W. T. S. Huck, W. Liu, *Anal. Chem*. **2007**; *79*, 176.

25 S. Minko, M. Muller, M. Motornov, M. Nitschke, K. Grundke, M. Stamm, *J. Am. Chem. Soc.* **2003**, *125*, 3896.

26 A. Sidorenko, S. Minko, K. Schenk-Meuser, H. Duschner, M. Stamm, *Langmuir* **1999**, *15*, 8349.

27 B. Zhao, W. J. Brittain, W. S. Zhou, S. Z. D. Cheng, *J. Am. Chem. Soc.* **2000**, *122*, 2407.

28 M. Ruths, D. Johannsmann, J. Ruhe, W. Knoll, *Macromolecules* **2000**, *33*, 3860.

29 B. Zhao, W. J. Brittain, *Prog. Polym. Sci.* **2000**, *25*, 677.

30 M. Müller, *Phys. Rev. E.* **2002**, *65*, 030802

31 M. Lemieux, D. Usov, S. Minko, M. Stamm, H. Shulha, V. V. Tsukruk, *Macromolecules* **2003**, *36*, 7244.

32 I. Luzinov, S. Minko, V. V. Tsukruk, *Prog. Polym. Sci.* **2004**, *29*, 635.

33 A. C. Balaz, C. Singh, E. Zhulina, D. Gersappe, *Prog. Coll. Polym. Sci.*, **1997**, *103*, 234.

34 E. Zhulina, A. C. Balazs, *Macromolecules* **1996**, *29*, 2667.

35 Y.-H. Lin, J. Teng, E. R. Zubarev, H. Shulha, V. V. Tsukruk *Nano letter*, **2005**, 5, 491

36 I. Luzinov, D. Julthongpiput, H. Malz, J. Pionteck, V. V. Tsukruk, *Macromolecules* **2000**, *33*, 1043

37 I. Luzinov, D. Julthongpiput, V. V. Tsukruk *Polymer* **2001**, *42*, 2267

38 http://www.ifm.liu.se/applphys/sensor/self.html

39 D. Gan, S. Lu, Z. Wang, *Journal of Colloid and Interface Science* ; **2001**; *239*; 272.

40 R. A. Xie, J. F Douglas, C. C. Han, R. A. Weiss, *Phys. Rev. Lett.* **1998**, *81,* 1251

41 D. N. Leonard, P. E. Russell, S. D. Smith, R. J. Spontak, *Macromol. Rapid Communi.* **2002,** *23*, 205.

42 T. W. Kelley, P. A. Schorr, K. D. Johnson, M. Tirrell, C. D. Frisbie, *Macromolecules* **1998**, *31*, 4297.

43 D. Goodman, J. N. Kizhakkedathu, D. E. Brooks, *Langmuir* **2004**, *20*, 2333.

44 V. Koutsos, E. W. VanderVegte, E. Pelletier,; Stamouli, A.; Hadziioannou, G. *Macromolecules* **1997**, *30*, 4719.

45 R. Raiteri, M. Grattarola, H. J. Butt, P. Skladal, *Sens. Actuator, B*, **2001**, *79,* 115.

46 N. V. Lavrik, M. J. Sepaniak, P. G. Datskos, *Rev. Sci. Instrum.* **2004**, *75*, 2229.

47 C. Ziegler, *Anal. Bioanal. Chem.* **2004**, *379*, 946.

48 J. R. Barner, R. J. Stephenson, M. E.Welland, C. Geberr, J. K. Gimzewski, *Nature* **1994,** *372*, 79.

49 T. Thundat, R. J. Warmack, G. Y. Chen, D. P. Allison, *Appl. Phys. Lett.* **1994**, *64*, 2894.

50 M. Sepanicak, P. Datskos, N. Lavrik, C. Tipple, *Anal. Chem.*, **2002**, *74*, 568.

51 P. G. Datskos, P. I. Oden, T. Thuandat, E. A. Watchter, R. J. Warmack, S. R. Hunter, *Appl. Phys. Lett.* **1996,** *69*, 2986.

52 M. Calleja, J. Tamayo, A. Johansson, P. Rasmussen, L. Lechuga, A. Boisen, *Sens. Lett.* **2003**, *1*, 1.

53 L. A. Pinnaduwage, V. Boiadjiev, J. E. Hawk, T. Thundat, *Appl. Phys. Lett.* **2003**, *83*, 1471.

54 X. Yan, Y. Lvov, H. Ji, A. Singh, T. Thundat, *Org. Biomol. Chem*. **2003**, *1*, 460.

55 X. Yan, X. K. Xu, H. Ji, *Anal. Chem.* **2005**, *77*, 6197.

56 K. Liu, H. F. Ji, *Anal. Sci.* **2004**, *20*, 9.

57 Y. F. Zhang, H. Ji, D. Snow, R. Sterling, G. M. Brown, *Instrum.Sci. Technol*. **2004**, *32*, 361.

58 G. Bambu, G. Kircher, M. Wolkenhauer, R. Berger, J. S Gutmann, *Macromol. Chem. Phys*. **2004**, *205*, 1713.

59 T. Perazzo, M. Mao, O. Kwon, A. Majumdar, J. B. Varesi, P. Norton, *Appl. Phys. Lett.* **1999**, *74*, 3567.

60 C. Jongeun, J. Yamaguchi, S. Morales, R. Horowitz, Y. Zhao, A. Majumdar, *Sens. Actuators, A*. **2003**, *104*, 132.

61 L. R. Senesac, J. L. Corbeil, S. Rajic, N. V. Lavrik, P. G. Datskos, *Ultramicroscopy* **2003**, *97*, 451.

62 Y. Zhao, M. Mao, R. Horowitz, A. Majumdar, J. Varesi, P. Norton, J. Kitching, *J. Microelectromech. Syst.* **2002**, *11*, 136.

63 C. Escriba, E. Campo, D. Estève, J. Y. Fourniols, *Sens. Actuators, A* **2005**, *120*, 267.

64 P. G. Datskos, M. J. Sepaniak, C. A. Tipple, N. Lavrik, *Sens. Actuators, B* **2001**, *76*, 393.

65 P. G. Datskos, N. Lavrik, S. Rajic, *Rev. Sci. Instrum*. **2004**, *75*, 1134.

66 J. R. Barnes, R. J. Stephenson, C. N. Woodburn, S. J. O'Shea, M. E. Welland, T. Rayment, J. K. Gimzewski, Ch. Gerber. *Rev. Sci. Instrum.* **1994**, *65*, 3793.

67 J. K. Gimzewski, C. Gerber, E. Meyer, R. R. Schlitter, *Chem. Phys. Lett.* **1994,** *217*, 589.

68 B. Li, *Sens. Actuators, A* **2004**, *112*, 351.

69 M. A. Unger, H. P. Chou, T. Thorsen, A. Scherer, S. R. Quake, *Science* **2000**, *288*, 113.

70 B. Zhao, J. S Moore, D. J. Beebe, *Anal. Chem.* **2002**, *74*, 4259.

71 J. Y. Lao, J. G. Wen, Z. F. Ren *Nano Lett.* **2002**, *2*, 1287.

72 M. H. Huang, S. Mao, H. Feick, H. Q Yan, Y. Y. Wu, H. Kind, E. Weber, R. Russo, P. D. Yang, *Science* **2001**, *292*, 1897.

73 Z. W Pan, Z. R. Dai, Z. L. Wang, *Science* **2001**, *291*, 1947

74 X. Y. Kong, Z. L. Wang, *Nano Lett.* **2003**, *3*, 1625.

75 X. Y. Kong, Y. Ding, R. Yang, Z. L. Wang, *Science* **2004**, *303*, 1348.

76 W. L. Hughes, Z. L. Wang *J. Am. Chem. Soc.* **2004**, *126*, 6703.

77 P. X.Gao, Y. Ding, W. J.vMai, W. L.Hughes, C. S. Lao, Z. L. Wang *Science* **2005**, *309*, 1700.

78 M. H. Huang, S. Mao, H. Feick, H. Q. Yan, Y. Y. Wu, H. Kind, E. Weber, R. Russo, P. D. Yang, *Science* **2001**, *292*, 1897.

79 Z. L. Wang, J. H. Song *Science* **2006**, *312*, 242.

80 B. A. Buchine, W. L. Hughes, F. L. Degertekin, Z. L. Wang, *Nano Lett.* **2006**, *6*, 1155.

81 J. H. He, C. L. Hsin, J. Liu, L. J. Chen, Z. L. Wang, *Adv. Mater.* **2007**, *19*, 781.

82 Y. B. Li, Y. Bando, D. Golberg *Appl. Phys. Lett.* **2004**, *84*, 3603.

83 He, J. H.; Ho, S. T.; Wu, T. B.; Chen, L. J.; Wang, Z. L. *Chem. Phys. Lett.* **2007**, *435*, 119.

84 K. Keem, H. Kim, G. T. Kim, J. S. Lee, B. Min, K. Cho, M. Y. Sung, S. Kim, *Appl. Phys. Lett.* **2004**, *84*, 4376.

85 Z. Y. Fan, P. C. Chang, J. G. Lu, E. C. Walter, R. M. Penner, C. H. Lin, H. P. Lee *Appl. Phys. Lett.* **2004**, *85*, 6128-6130.

86 H. Kind, H. Yan, B. Messer, M. Law, P. Yang, *Adv. Mater***. 2002**, *14*, 158.

87 C. Soci, A. Zhang, B. Xiang, S. A. Dayeh, D. P. R. Aplin, J. Park, X. Y. Bao, Y. H. Lo, D. Wang, *Nano. Lett.*, **2007**, *7*. 1003.

88 S. J. Tans, R. M. Verschurern C. Dker, *Nature* **1998,** *393* 49.

89 H. Kind, H. Yan, B. Messer, M. Law, P. Yang, *Adv. Mater*, **2002**, *14*, 158.

90 M. H. Lu, Y. Zhang, *Adv. Mater.* **2006**, *18*, 3094.

91 S. Y. Lin, J. G. Fleming, *Nature* **1998**, *394*, 251.

92 J.-.H. Jang, C. K. Ullal, T. Choi, M. C. Lemieux, V. V. Tsukruk, E. L. Thomas, *Adv. Mater*, **2006**, *18*, 2123.

93 S. Noda, K. Tomoda, N. Yamamoto, A. Chutinan, *Science* **2000**, *289*, 604.

94 G. M. Gratson, M. Xu, J. A. Lewis, *Nature* **2004**, *428,* 386.

95 M. Campbell, D. N. Sharp, M. T. Harrison, R. G. Denning, A. J. Turberfield, *Nature* **2000**, *404*, 53.

96 J. Léopoldès, P. Damman, *Nat. Mater*. **2006** *5*, 957.

97 a) E. Kim, Y. Xia, G. M. Whitesides, *Nature* **1995**, *376*, 581. b) J. Zaumseil, M. A. Meitl, J. W. P. Hsu, B. R. Acharya, K. W. Baldwin, Y.-L. Loo, J. A. Rogers, *Nano Lett.* **2003**, *3*, 1223.

98 G. M. Whitesides, E. Ostuni, S. Takayama, X. Y. Jiang, D. E. Ingber, *Annu. Rev. Biomed. Eng.* **2001**, *3*, 335.

99 K. Y. Suh, Y. S. Kim, H. H. Lee, *Adv. Mater*. **2001**, *13*, 1386.

100 M. Mrksich, *Chem. Soc. Rev.* **2000**, *29*, 267.

101 *Langmuir-Blodgett Films* (Ed: G. Roberts), Kluwer Academic Norwell MA 1990.

102 G. Decher, *Science* **1997**, *277*, 1232.

103 J. Park, L. D. Fouche, P. T. Hammond, *Adv. Mater.* **2005**, *17*, 2575.

104 C. Jiang, S. Markutsya, V. V. Tsukruk, *Langmuir* **2004,** *20*, 882.

105 C. Jiang, H. Ko, V. V. Tsukruk. *Adv. Mater.* **2005**, *17,* 2127.

106 J. A. Hiller, J. D. Mendelsohn, M. F. Rubner, *Nat. Mater*, **2002**, *1*, 59

107 F. Hua, T. Cui, Y. M. Lvov, *Nano Lett.* **2004**, *4*, 823.

108 C. Jiang, V. V. Tsukruk, *Adv. Mater.* **2006**, *18*, 829.

109 G. Decher, *Science,* **1997,** *277*, 1232.

110 G. Decher, J. B. Schlenoff, *Multilayer Thin film*, WILEY-VCH:Weinheim, **2003**.

111 S. A. Sukhishvili, *Curr Opin Colloid Interface Sci*, **2005**, *10*, 37.

112 Z. Liang, O. M. Cabarcos, D. L. Allara, Q. Wang, *Adv. Mat*. **2004,** 16, 823.

113 D. Zhou, A. Bruckbauer, C. Abell, D. Klenerman, D-J Kang, *Adv. Mat* .***2005,*** *17* 1243.

114 A. A. Mamedov, N. A. Kotov, M. Prato, D, M. Guldi, J. P. Wicksted, A. Hirsch, *Nat. Mater*, **2002,** *1*, 190.

115 C. Jiang, S. Markutsya, Y. Pikus, V. V. Tsukruk, *Nat. Mater*. **2004**, *3*, 721.

116 M. H. Lm, D. G. Ast. Adv. Mater, **2001,** *13* 718.

117 S. Porel, S. Sngh, S. S. Harsha, D. N. Rao, T. P. Radhakrshnan, *Chem. Mater*, **2005**, *17*, 9.

118 A. A. Antipov, G. B. Sukhorukov, *Adv. Colloid Inter. Sci*, **2004**, *111*, 49.

119 S. C. Peyratout, L. Dahane, *Angew Chem Int. Ed*. **2004,** *43,* 3762.

120 Y. G. Guo, J-S. Hu, H-P. Liang, L.J.Wan, C-L.Bai, *Adv. Funct. Mater*. **2005**, *15*, 196.

121 D. Silvano, S. Krol, A. Diaspro, O, Cavalleri, A. Glozzi, *Microscopy Res. Tech.* **2002**, *59*, 536.

122 F. Hua, T. Cu, Y. M. Lvov, *Nano Lett*. **2004***, 5*, 823.

123 A. A. Mamedov, N. A. Kotov, Langmuir, **2000**, *16*, 5530.

124 H. Ko, C. Jiang, V. V. Tsukruk, *Chem. Mater.* **2005**, *17*, 5489.

125 D. Winoto, S. H, Carr, *Macromolecules* **1996,** *29*, 5149.

126 V. V. Tsukruk, I. Luzinov, D. Julthongpiput, *Langmuir*, **1999**, *15,* 3029.

127 Tsukruk, V.V. *Rubber Chem. Technol.* **1997**, *70*, 430. Tsukruk, V. V.; Reneker, D. H. *Polymer*, **1995***, 36*, 1791.

128 Tsukruk, V. V.; Sidorenko, A.; Gorbunov, V. V.; Chizhik, S. A. *Langmuir* 2001, *17*, 6715.

129 www.veeco.com

130 Foster, B. in Comprehensive Desk Reference of Polymer Characterization and Analysis Brady, R.F Jr. (Ed.) Oxford University Press: New York, **2003**.

131 R. M. A. Azzam and N. M. Bashara, *Ellipsometry and Polarized Light*, Elsevier Science Pub Co (**1987**)

132 I. Luzinov, D. Julthongpiput, A. Liebmann-Vinson, T. Cregger, M. D. Foster, V.V. Tsukruk, Langmuir **2000**, *16*, 504.

133 J. L. Hutter, J. Bechhoefer, *Rev. Sci. Instrum*. **1993**, *64*, 1868.

134 *Structural Mechanics Module Model User's Guide for Femlab3*, COMSOL AB,

CHAPTER 4
OBSERVING NANOSCALE FLUIDIC FLIP-FLOPS: SWITCHABLE Y-SHAPED BRUSHES IN SELECTIVE SOLOVENTS

A paper published in Nano Letter 2004, 126, pp 9675-9684

Yen-Hsi Lin, Jinag. Teng, E. R. Zubarev, H. Shulha, V. V. Tsukruk *

Department of Materials Science & Engineering, Iowa State University, Ames, 50011 IA

Abstract

Direct, in-fluid observation of the surface morphology and nanomechanical properties of the mixed brushes composed of Y-shaped binary molecules PS-PAA revealed nanoscale network-like surface topography formed by coexisting stretched soluble PAA arms and collapsed insoluble PS chains in water. Placement of Y-shaped brushes in different fluids resulted in dramatic reorganization ranging from soft repellent layer covered by swollen PS arms in toluene to an adhesive, mixed layer composed of coexisting swollen PAA and collapsed PS arms in water. These binary layers with the overall nanoscale thickness can serve as adaptive nanocoatings with stimuli-responsive properties.

Introduction

Nanoscale switchable surfaces bring a new dimension in adaptive, stimuli responsive micromechanical and microfluidic devices and sensors. Responsibe organic and polymer layers hold a great promise in designing of nano-electromechanical, bioanalytical, and microfluidic devices with adaptive surface elastic, adhesive, and adsorbing properties.

♦ Primary researcher; carried out most of experiments, writer of all drafts.

[1,2,3,4,5,6] The macroscopic responses of such smart surfaces result from the reorganization of the structure or composition of the topmost layer. This reorganization controls the physical properties important in applications of colloid stabilization, drug delivery, chemical gates, and tuning nanotribological properties of tailored surfaces.[7,8] Surface composition and, hence, the surface energy, friction, and wettability can be "tuned" in reversible manner. This approach provides a means for the fabrication of "smart surfaces" with on-demand switchable properties such as self-cleaning abilities and switching from ultrahydrophobic to ultrahydrophilic behavior and vice versa.[6,7] Reversible switching of surface properties has been recently observed for mixed, binary brushes grafted to a solid substrate.[9,10,11,12,13,14,15] Theoretical consideration predicted that such binary brushes should form a wide variety of segregated surface layers with various surface micellar structures controlled by chemical attachment, grafting density, and composition.[16,17,18]

Recently, we have introduced a novel type of Y-shaped, binary, amphiphilic brushes combining two dissimilar, hydrophobic and hydrophilic polymer chains (polystyrene (PS) and polyacrylic acid (PAA)) attached to a single focal point grafted to a silicon surface (Figure 4-1).[19] Our initial results pointed to intriguing surface properties and unusual surface nanostructures with outstanding switching ability under alternating treatments with different solvents.[20,21] All studies reported for these and other Y-shaped brushes[22] have been conducted for post-treated, dry surface layers in the air under an assumption of the identity of their "frozen-in" state to that occurring at a solid-fluid interface. However, actual surface morphology and properties of these nanoscale surfaces under fluids remains unexplored. Moreover, the formation of the nanoscale surface structures with organized, patterned morphology has been theoretically predicted for Y-shaped molecules [16] but has been never observed experimentally.

Here, we report on the first *direct observation* of the nanoscale interfacial (at solid-fluid interfaces) structures of Y-shaped binary brushes (see chemical formulas in Figure 1) under different fluids (solvents of different quality) accompanied by concurrent evaluation of their nanoscale surface properties with force spectroscopy (elastic response

and adhesive properties). Our studies showed that the surface reorganization of Y-shaped brush layers in different fluids results in switching from uniform, repellant, and complaint surface covered by swollen PS arms in toluene to heterogeneous, adhesive, and mixed surface composed of swollen PAA and collapsed PS arms in water.

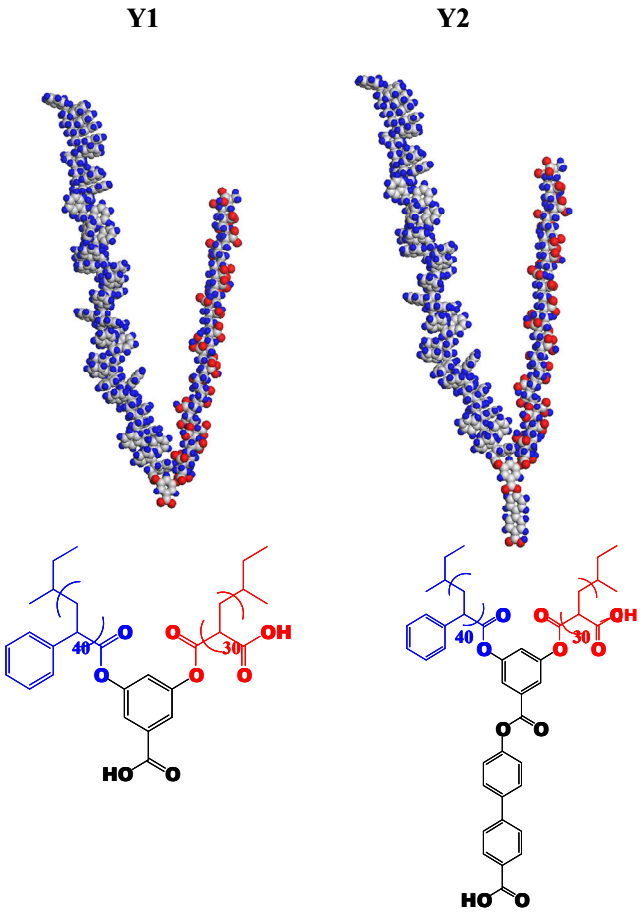

Figure 4-1. Chemical structure and molecular graphics representation of Y-shaped block copolymers with short (Y1) and long (Y2) aromatic functional stem. Molecules contain 40 and 30 monomeric units in PS and PAA arms, respectively

Results and discussion

Surface morphology in fluids.

Atomic force microscopy (AFM) imaging of **Y1** and **Y2** brush layers in toluene (selective solvent for PS arms), water (selective solvent for PAA arms), and mixed solvent of chloroform and methanol (1:1) (good solvent for both arms) revealed non-uniform

surface morphology with grainy nanoscale texture (Figure 4-2). The average thickness of the brush layers determined from a scratch test in fluid was close to 6 nm for brush layers in different solvents. This value was much higher than the effective thickness of 1.4 and 1.9 nm measured for **Y1** and **Y2** brush layers in dry state. This significant (fourfold) increase in brush layer thickness in selective solvents indicates the arms swelling and the formation of truly brush-like structure with significantly stretched chains as predicted for densely grafted polymer chains in brush regime. [20]

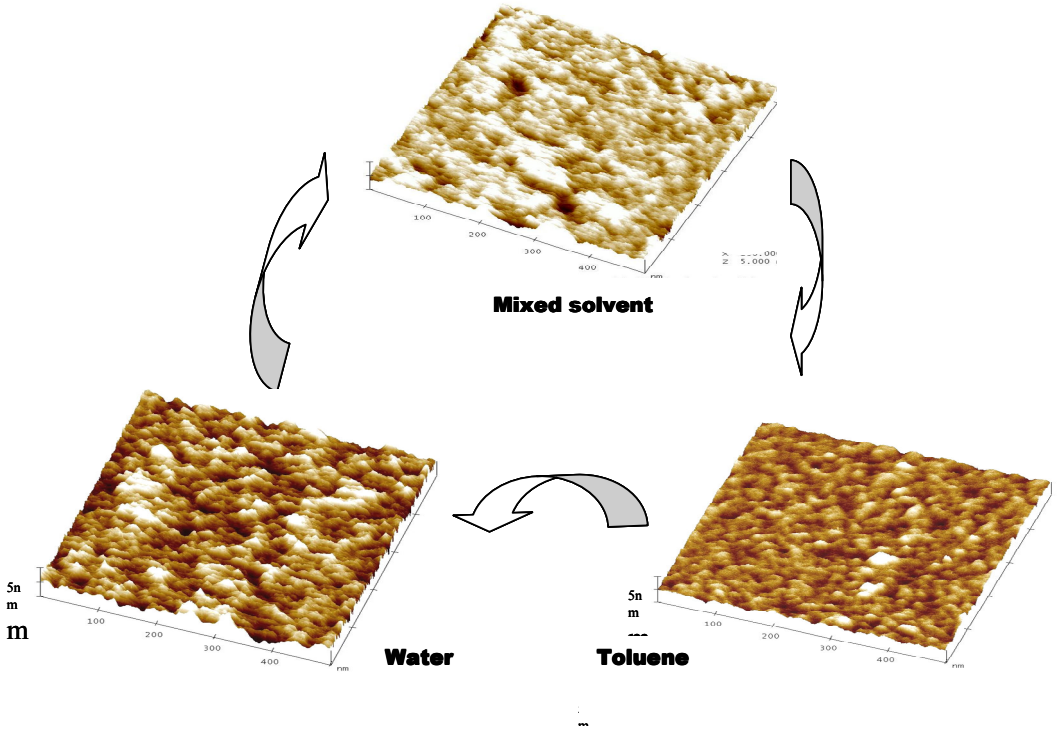

Figure 4-2. Representative 3D topographical images of Y1 brush layer (500 nm x 500 nm x 10 nm) in different solvents.

The surface microroughness evaluated within 500 nm x 500 nm areas reached 0.7 nm in water and 0.44 nm in toluene for **Y1** brush layer and 1.6 nm in water and 0.26 nm in toluene for **Y2** brush layer. Contrary to the expectation, the overall surface microroughness in water was consistently higher than in the dry state (0.7 vs 0.3 nm for **Y1** and 1.6 nm vs 0.7 nm for **Y2**). [20] The significant increase of the surface microroughness (more than twofold) in water as compared to the dry state reflects more non-uniform molecular topography after the placement of the brush layers in a selective solvent. This phenomenon

is caused by a vertical extension of PAA arms swollen in a good solvent with PS chains remaining in a collapsed state as demonstrated in molecular models in Figure 3. In fact, in air (a bad solvent for both arms) both dissimilar arms remain in the collapsed state (although in different configurations) even after treatments with selective solvents. On the other hand, lower surface microroughness for both brush layers in toluene (comparable to the dry state) can be associated with swollen longer PS arms fully "screening" collapsed PAA arms (see models in Figure 4-3). Finally, higher surface microroughness observed in the mixed solvent reflects concurrent swelling of both long-chain PS arms and short-chain PAA arms (Figure 1).

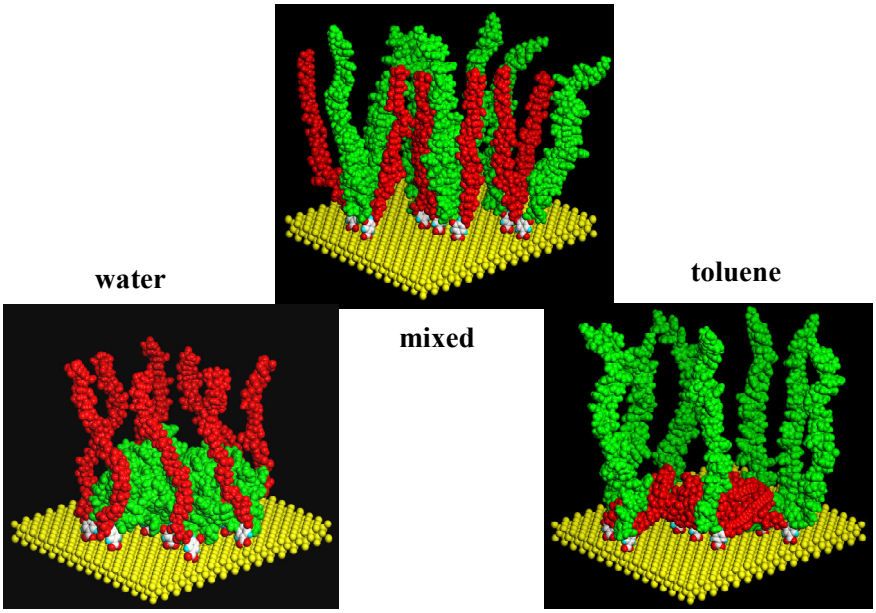

Figure 4-3. Molecular models showing internal molecular organization of an individual cluster comprising 7 Y1 molecules (green and red chains represent PS and PAA arms, respectively) in different solvents corresponding to the images in Figure 2.

Close inspection of high-resolution AFM images obtained for **Y1** brushes directly in different solvents revealed a random network of elevated ridges running across the surface (Figure 4-4a). This network is getting more ordered for **Y2** brush layer with occasionally seen local ordering expanding over a hundred nanometers across (Figure 4b). 2D Fourier transform image of this surface topography confirmed the presence of weakly

ordered network with six-fold symmetry with a cell periodicity close to 20 nm and positional correlations expanding over several adjacent cells.

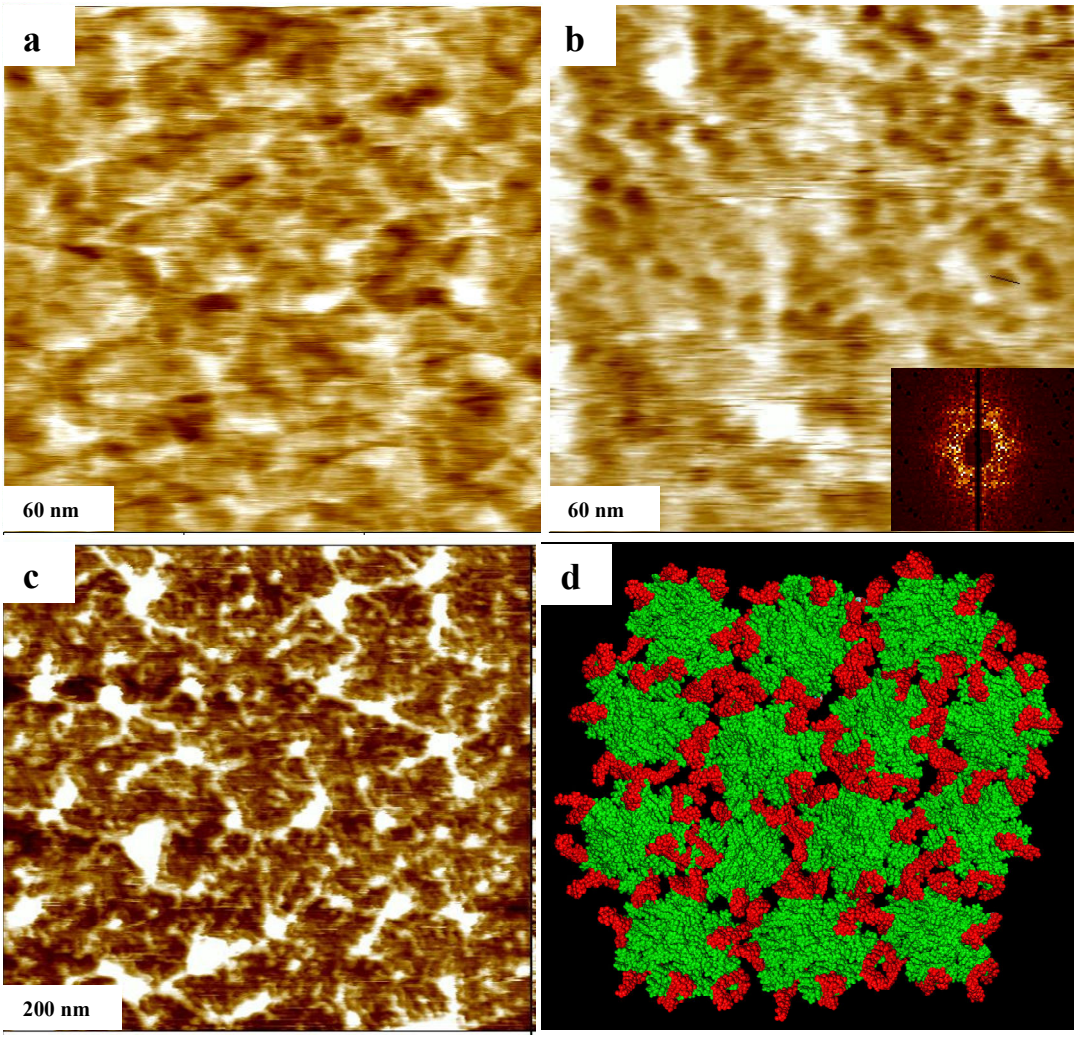

Figure 4-4. High-resolution AFM topographical images for Y1 (a) and Y2 (b) brush layers in water (insert shows corresponding 2D FFT image), Y1 brush layer in dry state decorated with adsorbed modified gold nanoparticles (d), and corresponding molecular model of PS and PAA nanophases distribution within the layer (d).

We suggest that this nanoscale topography is formed by extended PAA arms in water elevated above the collapsed counterpart (PS chains). They aggregate and form elevated, irregular ridges running along the borders between PS nanophases as represented schematically in corresponding molecular models in Figure 4-4d. In this multi-cluster

model, the red chains representing PAA arms elevated above collapsed PS domains composed of seven densely packed PS arms.[21] This molecular packing should result in the average cell size of 10-15 nm and an increasing number of grafted molecules in a cluster (e.g., doubling) will expand the cell size to 20-25 nm or close to that observed experimentally. The PAA composition of these ridges is additionally confirmed by studying selective adsorption of positively charged modified gold nanoparticles with a diameter of 5 nm as will be described in detail elsewhere (Figure 4-4c). In fact, we observed a strong preferential adsorption of the gold nanoparticles strictly along the ridges as guided by Columbic interactions between oppositely charged PAA arms and gold nanoparticles.

Short-range ordered nanoscale patterning observed here has been predicted by theoretical models for grafted Y-shaped molecules.[16] The lateral dimension of network cells is controlled by the level of nanophase separation between PAA and PS arms attached to the same grafting points as suggested in the molecular model (Figure 4-4c). Finally, we should note that although the elements of the ordered nanoscale patterning predicted by the theory and visualized by molecular modeling can be found for certain interfacial conditions, their complete characterization remains very difficult because of a technical challenge of collecting the high-resolution images of very compliant surface in the course of AFM scanning in fluid.

Nanoscale surface properties in fluids.

Significant changes in the surface properties (e.g., contact angle) were detected in the study of the Y-shaped brush layers in the dry state in our previous studies.[20,21] An actual surface reorganization under different fluids has never been detected before not only for Y-shaped but for any other type of switchable binary brush layers.[23] Thus, we probed the nanoscale properties of **Y1** brush layer (results for **Y2** layer are similar) by measuring the elastic response (the elastic modulus) and the adhesion (pull-off forces) directly within selective solvents, namely water and toluene (Figure 4-5).

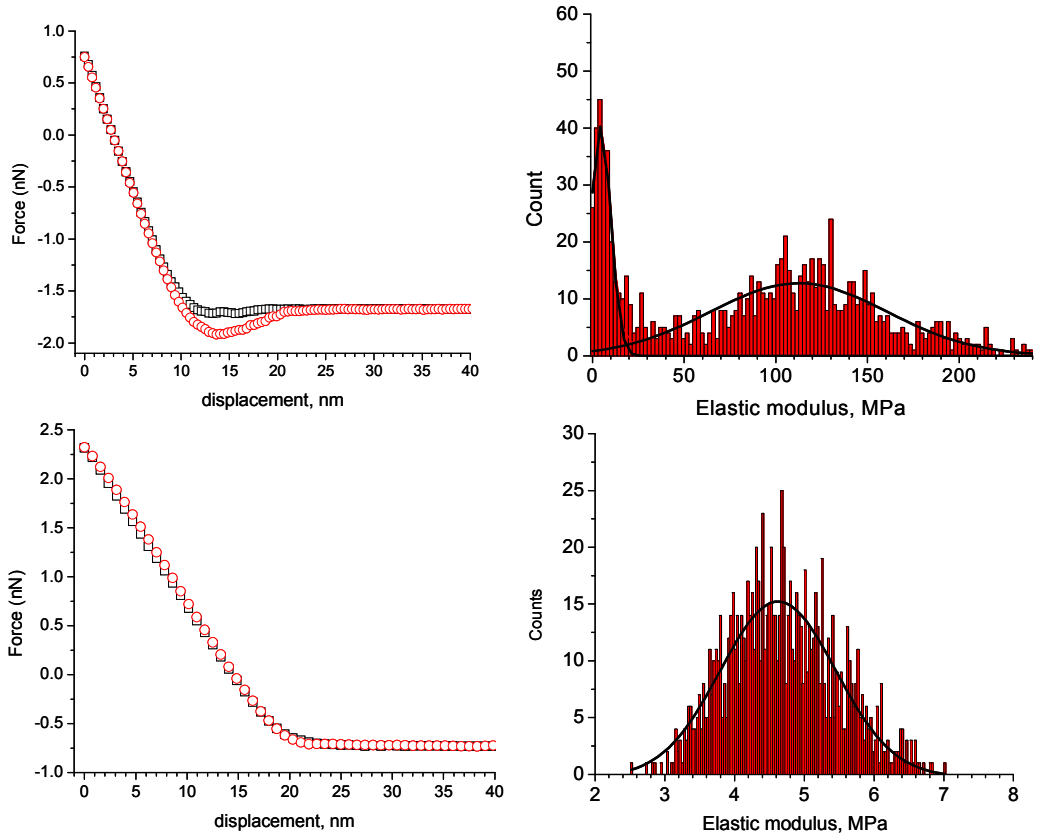

Figure 4-5. Results of nanomechanical probing of Y1 brush layer in different solvents, toluene (a,c) and water (b,d): (a, b) representative force distance curves and (c,d) surface distribution of the elastic moduli. Squares are approaching cycle and circles are retracing cycle.

Force-distance measurements confirmed the repulsive character of **Y1** brush layer in toluene with no detectable adhesive loop observed for a retracing cycle (Figure 4-5a). This behavior is expected for weakly interacting surface such as a hydrophilic silicon tip and hydrophobic surfaces.[24,25] In fact, in toluene the hydrophobic PS arms dominate the topmost surface layer. In a strike contrast, very significant adhesive forces were detected for the silicon tip interacting with the same Y-shaped brush layer placed in water. The pull-off forces reached 500 pN which is a very high value for interactions in fluid (Figure 4-4b). This level of adhesive force is expected for strong interactions between a tip with hydroxyl groups and a hydrophilic surface layer.[24,25] In fact, PAA arms are predominantly

extended above in water (Figure 4-3). Changes in adhesive forces detected directly in fluids are fully reversible and confirm the surface structural reorganization proposed for these Y-shaped brushes based on results for post-treated brush layers in the dry-state. [20] The overall thickness of the brush layer determined from multilayered modeling of the loading curves in indentation regime was close to 6 nm confirming the thickness independently obtained from the scratch test.

The analysis of force-distance curves in accordance with a modified Hertzian model for multilayered surfaces [29] allowed us to evaluate the surface distribution of the elastic moduli, *E*, for brush layers directly in selective solvents (Figure 4-5c,d). Surface histograms measured directly in water with a lateral resolution below 10 nm showed *bimodal distribution* of the elastic response for Y-shaped brush layer in water (Figure 4-5c). Compliant surface areas with low elastic modulus (E = 4.3 MPa) and stiffer surface areas with higher elastic modulus (E = 110 MPa) coexisted in brush layer in water. Both values of the elastic modulus were much lower than that estimated for the dry brush layer from similar nanomechanical mapping (430 MPa). The lower value of the elastic modulus calculated is close to that observed for highly swollen polymers (e.g., polyelectrolytes in good solvent[26]) and can be assigned to the surface areas with PAA arms aggregated in ridges as observed in topographical images in water. However, even in this state, with extended shorter PAA arms, the collapsed but longer PS arms still occupy up to 35% of total surface in accordance with cluster models discussed earlier.[20] The presence of these surface areas with uncovered collapsed PS clusters with higher elastic modulus causes the appearance of the stiffer surface areas and, thus, bimodal elastic response.

In contrast, the testing of the elastic response of **Y1** brush layer in toluene which is a good solvent for PS arms showed a uni-modal distribution of the elastic response with the average value of the elastic modulus centered around 4.6 MPa, a characteristic value for a polymer swollen in a good solvent (Figure 4-5d). Unlike previous case, this surface distribution indicates that the surface fraction of longer PS arms swollen in toluene is sufficient to completely cover the surface, thus, preventing the surface exposure of

collapsed PAA arms with higher elastic modulus. In addition, strong interaction between PAA chains and the hydrophilic silicon substrate may cause their uniform spreading in the immediate vicinity of the substrate.

Conclusions

In conclusion, direct, in-fluid observation of the surface morphology of the nanoscale binary brushes composed of Y-shaped amphiphilic molecules in a variety of selective and non-selective solvents revealed their grainy surface topography formed by coexisting stretched soluble arms in the brush regime and collapsed insoluble chains. Nanoscale patterning with short-range positional ordering predicted by theoretical models was directly observed for Y-shaped brush in water. Surface reorganization of Y-shaped brushes resulted in dramatic changes from uniform, repellent, compliant layer covered by swollen PS arms in toluene to an adhesive, mixed layer composed of coexisting swollen PAA and collapsed PS arms. The observed changes facilitate dramatic switching of macroscopic surface characteristics "frozen-in" in the post-treated, dry state leading to the controllable variation of the contact angle. [20] We believe that these Y-shaped binary surface layers with efficient switchable properties in different fluids and the overall thickness not exceeding several nanometers can serve as adaptive coatings for nanofluidic channels with stimuli-responsive properties. The specific molecular architecture and the length (~10 nm) of the grafted Y-shaped molecules is believed to be responsible for the observed nanophase separation and weak periodicity of nano-sized domains in water. This hydrophobic-hydrophilic contrast may allow for size- and shape-selective adsorption of various molecular species ranging from inorganic clusters to biological matter. The nanoscale thickness of these switchable surface layers firmly grafted to the silicon surfaces well below the thickness of conventional surface coatings (hundred nanometers) can be critical for advanced applications such as controlling fluidic flow or selective adsorption within channels with a diameter below 100 nm that remains unachievable by any synthetic or lithographic techniques.

Experimental

The synthesis of the Y-shaped molecules presented in Figure 1 and the fabrication of chemically grafted layers are described in detail elsewhere. [19,20] Molecular models were built with Materials Studio as described in detail earlier. [20] Atomic force microscopy (AFM) studies in tapping mode were performed on a Multimode Nanoscope IIIa microscope (Digital Instruments, Inc.) equipped with a fluid cell according to procedures adapted in our lab. [27] Probing of surface nanomechanical properties was conducted directly in fluids after allowing for the equilibration with solvents with usual force spectroscopy approach by using cantilevers with characterized spring constants and tip radii. [28] Force Volume mode within 300 nm x 300 nm randomly selected surface areas was applied. The data processing and calculation of the elastic modulus and surface histograms were carried out in accordance with multilayered contact mechanics model described earlier. [27,29]

Acknowledgements

We acknowledge support by the National Science Foundation, CMS-0099868 and DMR-0308982 Grants. The authors thank M. Lemieux for fruitful discussions.

References

1 R. Blossey, *Nat. Mater.* **2003**, *2*, 301.

2 N. Nath, A. Chilkoti, *Adv. Mater.* **2002**, *14*, 1243.

3 A. Lafuma, D. Quere, *Nat. Mater.* **2003**, *2*, 457..

4 D. M. Jones, J. R. Smith, W. T. S. Huck, C. Alexander, *Adv. Mater.* **2002**, *14*, 1130.

5 V. V. Tsukruk *Adv. Mater.* **2001**, *13*, 95.

6 J. Lahann, S. Mitragotri, T. N. Tran, H. Kaido, J. Sundaram, I. S. Choi, S. Hoffer, G. A. Somorjai, R. Langer S*cience* **2003**, *299*, 371.

7 Y. Ito, Y. Ochiai, Y. S. Park, Y. Imanishi *J. Am. Chem. Soc.* **1997**, *119*, 1619.

8 P. Mansky, Y. Liu, E. Huang, T. P. Russell, C. Hawker *Science* **1997**, *275*, 1458.

9 S. Minko, M. Muller, M. Motornov, M. Nitschke, K. Grundke, M. Stamm *J. Am. Chem. Soc.* **2003**, *125*, 3896.

[10] A. Sidorenko, S. Minko, K. Schenk-Meuser, H. Duschner, M. Stamm, *Langmuir* **1999**, *15*, 8349.

[11] B. Zhao, W. J. Brittain, W. S. Zhou, S. Z. D. Cheng *J. Am. Chem. Soc.* **2000**, *122*, 2407.

[12] M. Ruths, D. Johannsmann, J. Ruhe, W. Knoll, *Macromolecules* **2000**, *33*, 3860.

[13] B. Zhao, W. J. Brittain, *Prog. Polym. Sci.* **2000**, *25*, 677.

[14] M. Müller, *Phys. Rev. E.* **2002**, *65*, 030802.

[15] M. Lemieux, D. Usov, S. Minko, M. Stamm, H. Shulha, V. V. Tsukruk, *Macromolecules* **2003**, *36*, 7244.

[16] I. Luzinov, S. Minko, V. V. Tsukruk, *Prog. Polym. Sci.* **2004**, *29*, 635.

[17] A. C. Balazs, C. Singh, E. Zhulina, D. Gersappe, **1997**, *103*, 234.

[18] E. Zhulina, A. C. Balazs, *Macromolecules* **1996**, *29*, 2667.

[19] J. Teng, E. R. Zubarev, *J. Am. Chem. Soc.* **2003**, *125*, 11840.

[20] D. Julthongpiput, Y. H. Lin, J. Teng, E. R. Zubarev, V. V. Tsukruk, *Langmuir* **2003**, *19*, 7832.

[21] D. Julthongpiput, Y. H. Lin, J. Teng, E. R. Zubarev, V. V. Tsukruk *J. Am. Chem. Soc.* **2003**, *125*, 15912.

[22] B. Zhao, *Polymer* **2003**, *44*, 4079.

[23] R. C. Advincula, W. J. Brittain, K. C. Caster, & J. Ruhe, *Polymer Brushes.*; Wiley: Weinheim, 2004.

[24] A.Noy, D. V. Vezenov, C. M. Lieber, *Ann. Rev. Mater. Sci.* **1997**, *27*, 381.

[25] V. V. Tsukruk, V. N. Bliznyuk *Langmuir* **1998**, *14*, 446.

[26] A. Fery, F. Dubreuil, H. Mohwald, *New J. Phys.* **2004**, *6*, 1.

[27] V. V. Tsukruk, *Rubber Chem. Technol.* **1997**, *70*, 430.

[28] A. Kovalev, H. Shulha, M. Lemieux, N. Myshkin, V. V. Tsukruk *J. Mater. Res.* **2004,** *19*, 716.

[29] V. V. Tsukruk, A. Sidorenko, V. V.Gorbunov, S. A. Chizhik, *Langmuir* **2001**, *17*, 6715.

CHAPTER 5
MICROTRIBOLOGICAL AND NANOMECHANICAL PROPERTIES OF SWITCHABLE Y-SHAPED AMPHIPHILIC POLYMER BRUSHES

A paper published in Advanced Functional Materials 2005, 15, pp 1529-9684

Melburne C. LeMieux [a], Yen-Hsi Lin [a], Pham Duc Cuong, Hyo-Sok Ahn[1], Eugene R. Zubarev [a], Vladimir V. Tsukruk [a]

[a] Materials Science and Engineering Department, Iowa State University, Ames, IA 50011
[b] Tribology Research Center, Korean Institute of Science and Technology, Seoul 136-791 Korea

Abstract

We have characterized the morphology and nanomechanical properties of surface grafted nanoscale layers consisting of Y-shaped binary molecules with one polystyrene (PS) arm and one poly(acrylic acid) (PAA) arm. We examined these amphiphilic brushes in fluids (*in situ* visualization), and measured their microtribological characteristics as a function of chemical composition. AFM based nanomechanical testing has shown that the nanoscale reorganization greatly influences the adhesion and elastic properties of the nanoscale brush layer. A bimodal distribution of the elastic modulus in water was observed due to mixed chemical composition of the topmost layer. Unlike, the top layer is completely dominated by PS in toluene. As a result of this reorganization, the Y-shaped brush layer exhibited dramatic variation of the friction and wear properties after exposure to different solvents. Unexpectedly, the tribological properties were enhanced for a hydrophilic and polar, PAA dominated surface, which showed lowed friction

---

♦ Assistant researcher, did most of experiments, assistant writer of all drafts, revised final figures and final inside cover image

coefficient and higher wear stability despite higher adhesion and heterogeneous surface composition. We suggest that this unusual behavior is caused by the presence of a thicker water layer on the PAA-enriched surface acting as a boundary lubricant, combined with the glassy state of the PAA chains.

Introduction

Numerous examples of polymer brushes reported in the literature [1] clearly demonstrate their potential to create a new generation of materials whose properties could be tuned in a reversible manner upon changes in the local environment. External stimuli, such as subtle changes in chemical species[2], pH[3], temperature[4], pressure[5], and light[6] interacting with the brush have been shown to dramatically change the surface morphology, composition, and properties. Brushes based on block copolymers covalently attached to solid substrates[7], as well as mixed brushes[8] are particularly intriguing examples in that respect. This is because the variety of surface morphologies possible greatly increases. Surface composition and hence properties such as surface energy, adhesion, friction, and wettability have the possibility of being "tuned" to the necessary state.[9]

The interplay of interchain interactions and the penalty of entropic elasticity leads to the lateral phase separation and a characteristic "rippled" morphology as was initially predicted by theory[10,11] and later confirmed experimentally.[8c, 12] The presence of a selective solvent causes significant conformational rearrangements and the solvent-brush interactions promote the "perpendicular" microphase separation.[13] In that case the top layer composed of soluble chains covers collapsed insoluble blocks. Thus, the morphology of a given brush, due to the high grafting density and uniformity in thickness and morphology, may undergo remarkable changes upon the smallest fluctuations in solvent conditions. In fact, very recent studies by Möller et al.[14] have shown that even the presence of solvent vapor can change the shape of brush-like macromolecules from an extended wormlike conformation to a compact globule, and vice versa.

The morphology of block copolymer brushes also depends on which particular point tethers the macromolecule to the substrate. Several researchers predicted the formation of many unusual morphologies and nanopatterns if a block copolymer was attached to a solid surface through its junction point that connects two incompatible blocks.[15,16] Such Y-shaped macromolecules were later synthesized[17], and successfully grafted to silicon substrates as described elsewhere.[18,19] We observed unique "crater-like" morphology that could be switched reversibly to "pinned micellar" structures after treatment of the amphiphilic PS-PAA brushes with selective solvents. However, the fundamental question remained as to whether the same morphologies existed in the presence of selective solvents. In our preliminary report, we described the conditions for atomic force microscopy (AFM) imaging of a PS_{40}-PAA_{30} Y-shaped brush in fluids, but how the observed morphological changes affect engineering properties such as mechanical and tribological properties remains unrevealed.[20] These covalently bound nanoscale layers show a dramatic switching of morphology and surface roughness by sensing the local environment. Because of this, they have great potential as prospective materials in microfluidic devices that require "smart" surfaces, as well as for controlling the adsorption of protein or inorganic nanoparticles due to our design approach of switching between a sticky hydrophilic surface, to a repellant hydrophobic surface layer. In general, this report addresses a largely unexplored field of characterizing the properties of switchable polymer layers *directly in* fluid. Such knowledge is imperative since the applications listed above, and most of the foreseen applications of polymer nanolayers, especially in biotechnology and microfluidic fields, involve implementing them in fluidic environments.

Here we explore how the chemical composition of the Y-shaped molecules chemically grafted to a silicon surface affects the morphology, microroughness, adhesion, and elastic modulus *in the presence* of selective solvents. In addition, we report the unique measurements of microtribological properties of the Y-shaped brush layers in which the frictional forces and wear were found to strongly depend on the morphology and composition of brush layer with much better wear stability unexpectedly found for

more polar layer with mixed chemical composition. Microtribological properties may be reversibly tuned by solvent treatment.

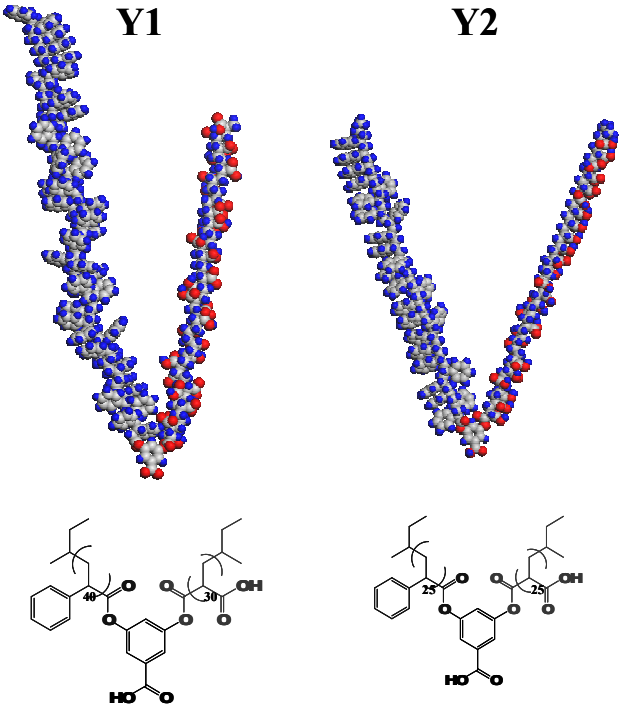

Figure 5-1. Molecular model and chemical structure of Y1 (left) and Y2 (right) arms and the short anchoring junction (functional aromatic group). Y1 consists of 40 PS and 30 PAA monomeric units while Y2 is symmetrical with 25 units each

Results and discussions

Surface morphology of amphiphilic Y-brushes in selective solvents.

Upon grafting, the Y-shape molecules formed a clean, homogeneous surface with a surface microroughness below 0.4 nm in the dry state. This value of surface roughness, measured over a 1x1 μm^2 area, was far below the contour length of both PAA and PS arms ranging from 25 to 40 monomeric units (6-10 nm), respectively, meaning the grafted layers exhibit molecular smoothness. The dry thickness of the PS-PAA grafted layer was 1.4 and 1.9 ± 0.2 nm for **Y1** and **Y2** respectively (Table 5-1), as measured

independently by ellipsometry and the AFM scratch tests. The medium grafting density (Table 5-1), typical of the "grafting to" approach, corresponds to a distance of 3.5 nm between anchor locations of the Y-shape molecules. This indicates the arms are slightly deformed (constrained), as is typical of the brush regime.[21] The effect of PS versus PAA composition in **Y1** and **Y2** is observed by contact angle measurements after treatment with toluene. Brushes based on molecule **Y1**, which has chemical composition of (PS_{40}-PAA_{30}) have contact angle of 73°, while the symmetric **Y2** brush (PS_{25}-PAA_{25}) has a contact angle of 61° (Table 5-1). The lower value of **Y2** is a reflection of a lower composition of the hydrophobic PS chains at the surface compared to **Y1** brushes.

Table 5-1. Parameters of the Y-shaped PS-PAA grafted layers in air

Brush	As-synthesized thickness (nm)	microroughness (nm)	Contact angle after water (°)	Contact angle after toluene (°)	Grafted amount (mg/m^2)	Grafting density (chains/nm^2)
Y1	1.4 ± 0.20	0.37 ± 0.1	54 ± 2	73 ± 2	1.42	0.11
Y2	1.9 ± 0.22	0.27± 0.1	50 ± 2	61 ± 2	1.95	0.20

The morphology of the grafted layers was characterized by *in-situ* AFM under toluene and water (Fig. 5-2). The thickness of the brushes in each selective solvent measured by the AFM scratch tests in fluid averaged 5.5 ± 0.5 nm for all surfaces as demonstrated for **Y1** brush layer with cross-sections obtained directly in different solvents (Fig. 5-2a,b). This is nearly four times higher than the dry-state thickness (Table 5-1) and represents a typical brush-like state when the chains swell away from the surface due to entropic effects and the resulting osmotic pressure. Due to the extremely small size of the structural features in these layers, from the 1x1 μm^2 AFM images alone, it remains unclear whether the brush is switching between a topmost layer dominated by PS blocks in toluene, to a PAA-dominated top layer under water. However, there are rather significant differences in roughness of the brush measured in toluene and that in water, which can be observed in the high-resolution 3D images presented in Figure 3. Notably, the roughness measured by AFM is two to three times higher in water than in toluene (Table 5-2).

Table 5-2. Physical properties of the Y-shaped layers in different solvents

Brush/ **Environment**	**microroughness (nm)**	**Average stable friction coefficient (μ)**	**Normalized pull-off force (pN/nm)**	**Elastic modulus (MPa)**
Y1 **in Toluene**	**0.44 ± 0.2**	**0.35***	**< 0.5**	**4.6**
Y1 **in Water**	**0.73 ± 0.3**	**0.21***	**20**	**Crater rim: 4.3** **Crater pit: 110**
Y2 **in Toluene**	**0.27 ± 0.1**	**0.55***	**< 0.5**	**22**
Y2 **in Water**	**0.90 ± 0.1**	**0.35***	**39**	**Crater rim: 2.2** **Crater pit: 125**

For **Y1** in water, the hydrophobic PS chains cannot be covered completely by PAA whose volume fraction is nearly 2 times lower than that of bulky PS arms (34 vs. 66 %). Similar observation was made for **Y2**, although the volume fraction of PAA chains in this brush is slightly lower (30 %) causing an even larger disparity in coverage. The layering of PAA over the PS arms is incomplete in both brushes in water leading to higher heterogeneity and surface microroughness. On the other hand, in toluene, which is a good solvent for PS, surface roughness is lower suggesting that a more homogenous top layer is present. In fact, longer PS arms can shield the layer of collapsed PAA chains, which have a lower volume fraction and a greater affinity to the hydrophilic silicon substrate.

Molecular modeling of the Y-shaped PS-PAA brushes explains the observed switching of the morphology (Fig. 5-3). Here, we modeled seven Y-shaped molecules on a hexagonal lattice spaced 3.5 nm apart, which represented an experimentally determined distance between the anchor points. Using a force-field minimization and taking the factors described above into account, the model revealed a more vertical layering of PS over PAA in toluene (Fig. 5-3), producing a continuous PS surface. On the other hand,

due to the lower extent of PS collapse in water, the PAA arms cannot form a complete homogeneous layer over PS, thereby forming the crater-like structure similar to what was observed in the dry state.[19] However, this morphology is more amplified in the presence of selective solvent as the hydrophilic PAA chains stretch out in the direction perpendicular to the surface. This crater-like morphology is responsible for the threefold increase in the surface microroughness as the brush is transferred from toluene to aqueous environment. These data demonstrate high switchability of this important parameter, and the stimuli-responsive nature of the Y-shaped amphiphilic brushes (Table 5-2).

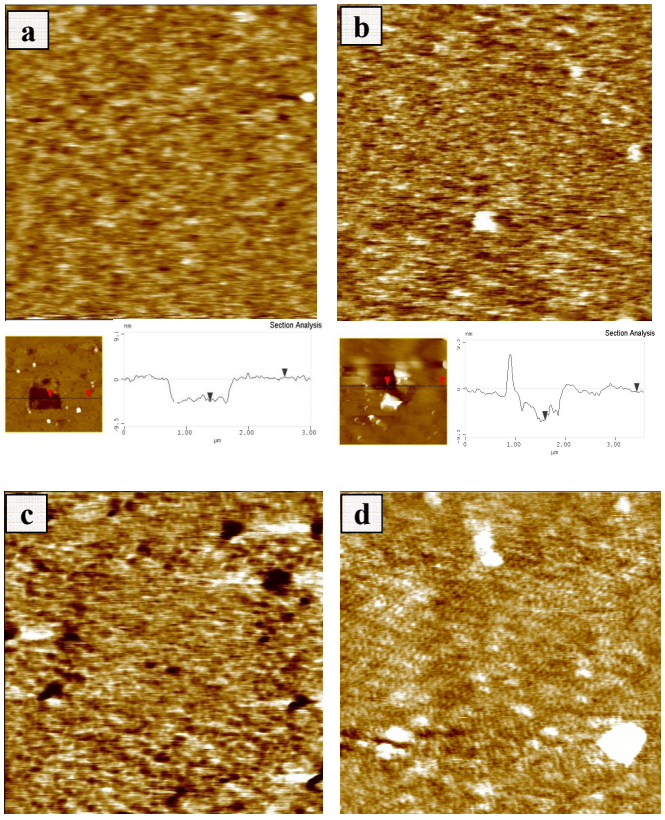

Figure 5-2. 1 x 1 μm^2 AFM topography images in fluids for Y1 in toluene (a) and water (b), bottom insets show hole produced within layer and corresponding cross-sections used for depth measurements; Y2 in toluene (c) and water (d). For all images Z-scale is 5 nm.

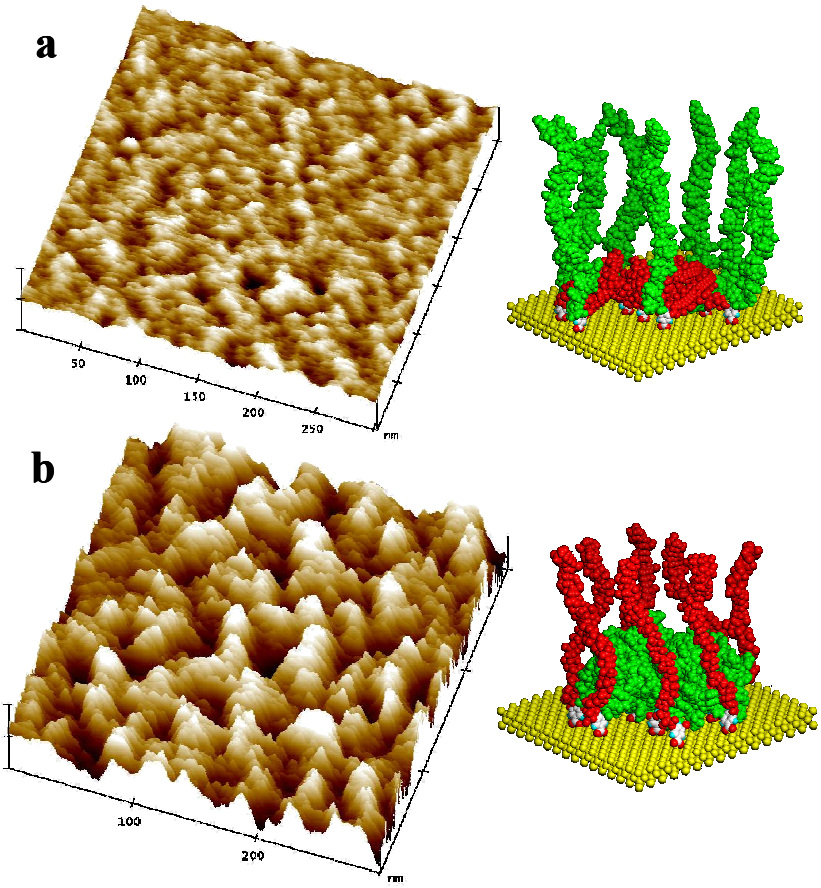

Figure 5-3. High-resolution (300 x 300 nm^2) tapping mode AFM topography images represented in 3D. Shown here is Y2 in toluene (a) and in water (b). Corresponding molecular models are shown as well

Nanoscale mechanical properties.

The observed conformational rearrangements should affect the mechanical properties of the brushes and their measurement in the presence of solvent gives a unique opportunity to assess these characteristics as a function of solvent-solute interactions (water or toluene) and chemical composition of the brush (**Y1** vs. **Y2**). No detectable adhesive forces were observed for both brushes in toluene (Fig. 5-4). This, along with the repulsive nature of the force-distance curves (FDCs), is typical for a surface of hydrophobic PS chains, which dominate the topmost surface layer. In contrast, for **Y1** in water, there was a noticeable pull-off force from the retraction curve of the FDC (Fig. 5-4). Typical values of this adhesion force ranged from 200 to 400 pN. This relatively

high level of adhesion is expected because the hydrophilic PAA arms are extending from the surface in water, and can directly interact with the hydrophilic silicon oxide AFM tip. For **Y2**, the level of adhesion in water was even higher with values ranging from 500 – 700 pN, which indicates strong tip-surface interactions with more PAA chains participating (Fig. 5-4).[22] Overall adhesives forces (normalized to the AFM tip radius) in water were twice as large for the **Y2** brush layer than the **Y1** layer (Table 5-2). This stronger adhesion with the **Y2** brush layer in water confirms the higher effective concentration of the PAA chains on the surface of the **Y2** brush layer (and interacting with the AFM tip) as can be expected from volume composition of the molecules (PAA_{Y1} = 34%, PAA_{Y2} = 41%). In addition, greater probing instabilities were introduced into the topography and AFM images when scanning the asymmetric brushes (**Y1**) as compared to Y-brushes with symmetric arms (**Y2**). These instabilities are caused by the tip interacting with two very different arms (like PS and PAA) simultaneously in **Y1**.[19] This is a remarkable observation considering the fact that the phase separation in these brushes can only occur at the nanoscale as it is limited by the length of the incompatible arms (~10 nm). The sensitivity of adhesive properties implies that small changes in chemical composition of the grafted Y-shaped molecules control the morphology in the presence of solvent.

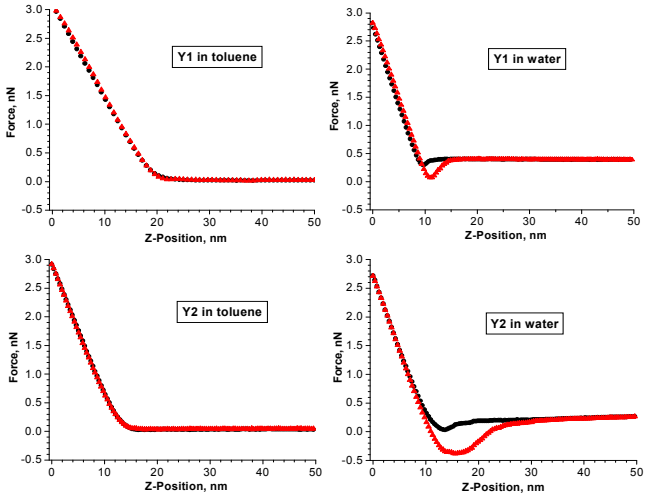

Figure 5-4. Representative FDCs (deflection scale converted to real force) for the Y-brushes in selective solvents. The circles represent the approaching curve and the triangles are the retrace curve for the FDCs.

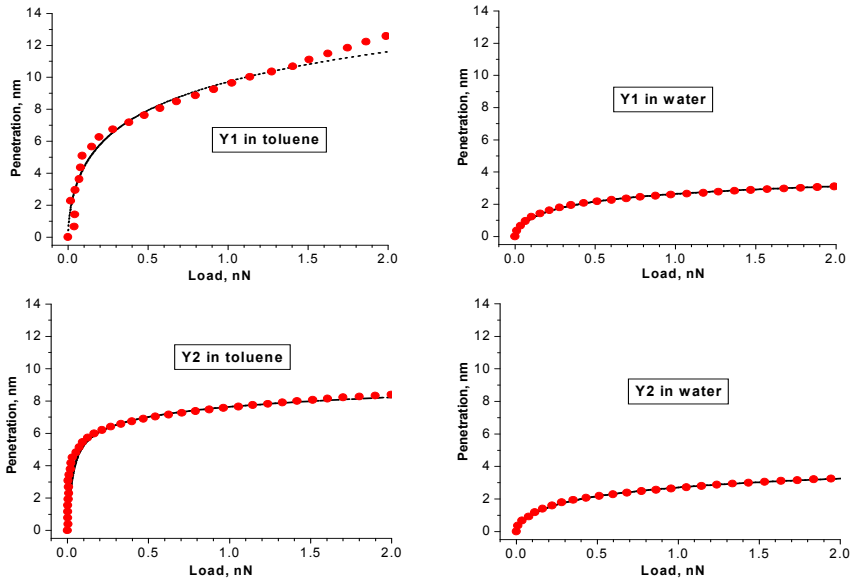

Figure 5-5. Representative load-penetration curves for the Y-brushes in selective solvents. The black line in the load-penetration curves is a simulated fit

Nanomechanical compression properties of the brush layers in-fluid can be evaluated from load-penetration data reflecting elastic indentation of the layers under normal load (Fig. 5-5). Loading curves were calculated from the FDCs using the modified layered Hertzian model.[23,24] Penetration through the layer requires very little force below 2 nN since PS arms are swollen in toluene. Both curves for **Y1** and **Y2** in toluene deviate from conventional Hertzian behavior by leveling off beyond some compression due to the presence of the stiff silicon substrate. Apparent maximum layer indentation reaches 8 nm for **Y2,** and is slightly higher with **Y1** because of the longer PS and PAA arms in **Y1**. The black lines in Figure 5-5 are the best fit from a multilayered model based on Hertzian loading, which allows evaluation of the elastic modulus and layer thickness.[35] An actual layer thickness derived from this analysis was close to 6 nm, which agrees well with the independent AFM scratch test in selective solvents. The elastic modulus was less than 25 MPa for both brush layers indicating the surface presence of swollen PS arms (Table 5-2).

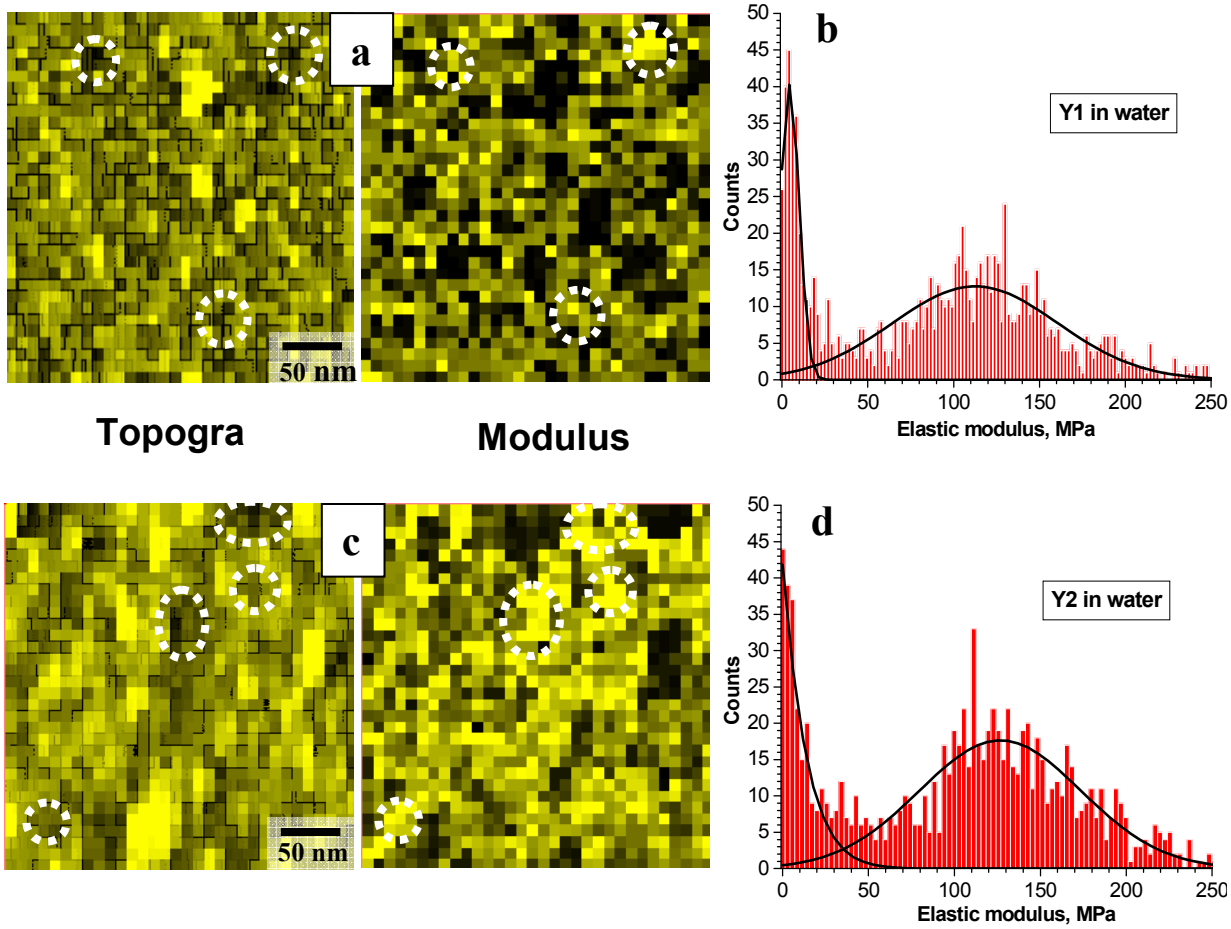

Figure 5-6. Simultaneous topography and force mapping over a 300 x 300 nm^2 area with 32x32 pixel resolution for FDCs. Resulting force-volume maps for Y1 in water (a) give a bimodal distribution (b) of the elastic modulus. For topography and modulus maps, the brighter the color, the higher the heights and the relative value of the modulus, respectively. Red circles in topography indicate low points (or pits) in topography, which correspond to the collapsed PS, and they correlate to the high points in the modulus map indicative of the hard, glassy PS chains in a bad solvent (water). The topography and modulus maps for Y2 (c) exhibit the same behavior also resulting in a bimodal distribution of the elastic modulus (d).

In water, a different shape of the load-penetration curves is observed with apparent indentation depth not exceeding 3 nm (Fig. 5-5). This change can be related to shorter PAA arms, resulting in a smaller thickness of a PAA layer over the collapsed PS

phase (Figure 5-3). The collapsed PS layer is impenetrable in this conformation relative to the soft AFM tip used in fluidic force measurements.

The concurrent surface mapping of topography and the elastic modulus represents a powerful tool to identify domain structure of brushes, and to obtain quantitative results describing their stiffness with nanoscale resolution using AFM measurements in fluid. The topography and elastic modulus distribution maps in Figure 6 result from taking 1024 FDCs over a 300 x 300 nm^2 area directly in solvent with resolution below 10 nm. The analysis of the FDCs for **Y1** and **Y2** brushes in water with a Hertzian model to extract the exact modulus resulted in bimodal histograms of surface distributions for both layers (Fig. 5-6b, 6d). Both bimodal distributions obtained in fluid (water) show one peak at around 5 MPa, coming from the swollen PAA, and another peak at around 110 MPa, which is the apparent elastic modulus of the collapsed PS domains. Exact values from the Gaussian fits are given in Table 2 where the individual moduli from the "crater pit" (PS) and the "rim" (PAA) was distinguished for the water state. Close investigation of the topography and modulus maps allows one to correlate the low points in the topography (PS pits) with high points in the elastic modulus (see red circles in Fig 5-6a, 6c). Furthermore, the high points in topography (PAA) match very closely to the low elastic modulus values in the modulus map. This force mapping confirms the presence of both arms on the surface in the water state, which leads to the higher surface roughness (Table 5-2).

On the other hand, the surface distribution of the elastic modulus for **Y1** and **Y2** in toluene is unimodal (deviations within 20%) with much lower values of the apparent elastic moduli (Fig. 5-7a, 7b). However, the most interesting observation is the 5 fold increase in stiffness between **Y1** (4.6 MPa) and **Y2** (22 MPa) brushes (Table 5-2). This significant rise in stiffness occurs in spite of the fact that the volume fraction of PS only decreases from 66 to 59 %, respectively. The decreased compliance of **Y2** brush layer can be attributed to shorter arms and higher grafting density resulting in larger space constraints for arms compressed by the AFM tip. These findings clearly demonstrate that

even subtle variation in the chemical composition has a profound impact on the mechanical and surface properties of switchable Y-shaped brushes in fluids. The homogeneous character of brush layers swollen in toluene points out that the PS chains completely screen the PAA arms and forms a continuous smooth surface layer over PAA, confirming our previous suggestion made based on initial roughness analysis and molecular modeling (Fig. 5-3).

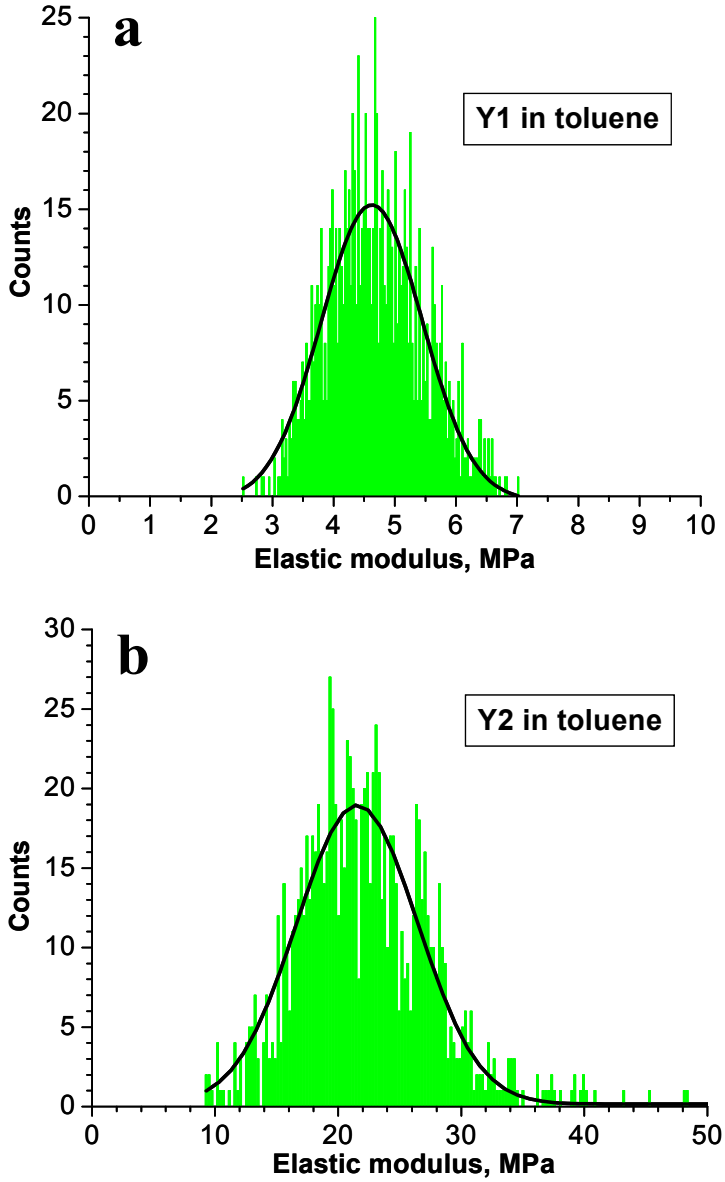

Figure 5-7. Resulting surface histograms for Y1 in toluene (a) and Y2 in toluene (b).

Microtribological properties of brush layers.

The friction coefficient (μ) of **Y1** and **Y2** measured against the sliding glass ball after exposure to toluene and water is dramatically affected by the surface composition of the layer (Fig. 5-8). For the **Y1** brush layer treated with water, the friction coefficient remains stable throughout the course of the test (1000 sliding cycles) with an average value of μ=0.21 (Fig 5-8a, Table 5-2). In contrast, the friction coefficient of **Y1** after toluene treatment is unstable and nearly twice as high as after water exposure. The same trend is also observed for **Y2** in which the toluene-treated sample was even more unstable and total failure occurred after 700 cycles (Fig. 5-8b). The averaged friction coefficient of **Y2** after toluene exposure is μ = 0.55, whereas after water treatment it is only 0.35 (Fig. 8b, Table 5-2). It is worth to note that although the absolute values of the friction coefficient for brush layers studied here are higher than usual values for polymeric and organic layers with optimized morphology (0.1 and below) [25,26] they are on a par with the friction coefficients found for many bulk glassy and rubbery polymers.[27]

The PS-dominated surface, being hydrophobic with low surface energy, would be expected to have a lower friction coefficient than a surface with ~60 % coverage of the high surface energy PAA layer.[28] However, one should consider the viscoelasticity of short PS chains and their glass transition temperature. It is well know that T_g of high molecular weight polystyrene is around 100°C, but it starts to decrease rapidly when the molecular weight becomes lower than 20 kDa. According to Flory[29], the T_g of PS with M_n=4100 g/mol (**Y1**) is approximately 50°C, and it drops to nearly 40°C when M_n=2600 g/mol (as in **Y2** brush). In addition, the presence of the collapsed PAA chains beneath PS chains can create conditions for increasing contact area thus facilitating higher friction forces. On the other hand, even a small amount of toluene trapped in these brushes may further decrease the T_g of PS arms (the samples dried at room temperature without annealing can contain residual solvent). However, considering that the friction coefficient is also significantly higher than that measured for PS homobrushes with similar chain length measured under identical conditions (0.3-0.4) [8d] we can exclude solvent effect on Y-brush behavior and suggest significant contribution from junction

point and PAA presence into lowering glass transition temperature. Therefore, we suggest that the PS chains in **Y1,** and especially the **Y2** brush, may be above their T_g and possess an appreciable amount of segmental mobility and viscoelastic properties in the contact area under significant shear stresses. As a result, a notable dissipation of energy would occur in these layers explaining the observed high friction coefficients. This hypothesis would be consistent with the experimental data that sliding over the **Y2** brush with shorter PS chains (lower T_g) generates greater frictional forces than in the **Y1** sample (Table 5-2).

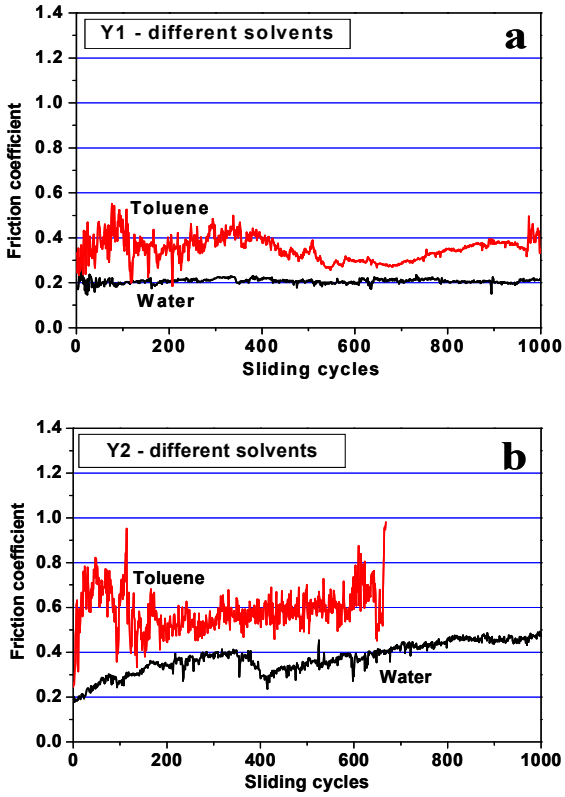

Figure 5-8. Microtribological data showing friction coefficient (μ) versus the number of sliding cycles comparing Y1 in toluene (red) and water (black) (a); and Y2 in toluene and water (b). Tests were conducted at 30% RH, with a normal load of 200 μN.

The difference in friction and adhesive properties also translates to significant difference in wear stability of brush layers with different compositions. This difference

manifests itself in different chemical composition and surface morphology of the initial and worn surface areas. Figure 5-9 presents AES depth profiles of the chemical composition in the **Y1** and **Y2** brush layers before and after the wearing test (after exposure to water). Apparently, molecules with shorter arms (**Y2**) experienced a huge loss of polymeric material represented by the decrease in carbon content and an increase in the silicon signal indicating removal of the organic materials and exposure of the underlying silicon oxide layer along with wear silicon particles (Fig. 5-9a, 9b). This is due to the lower molecular weight and depressed T_g of the top layer, which still has a large PS volume fraction. The abrasion resistance of **Y2** brush was significantly lower as well.

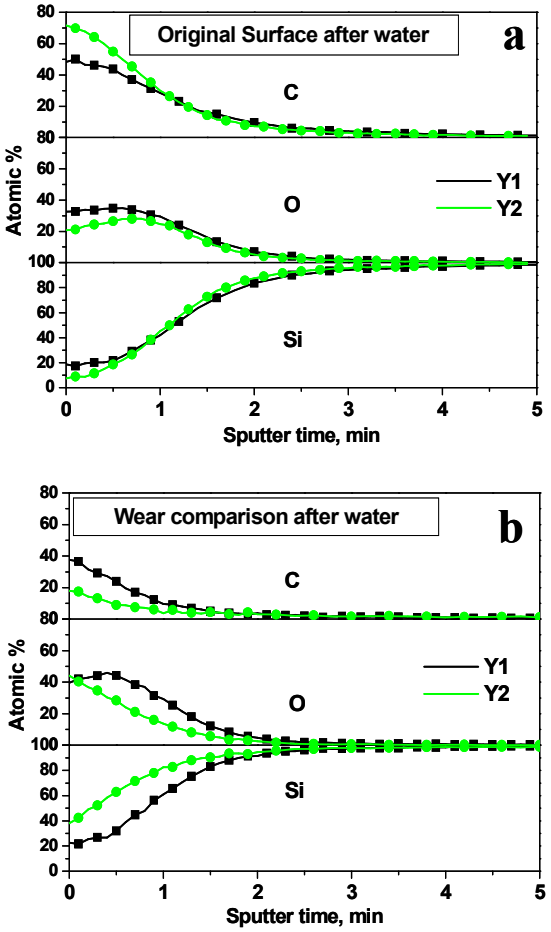

Figure 5-9. AES concentration profiles comparing the wear of Y1 and Y2 after water exposure. The original surface is shown in (a), while the worn area is given in (b).

The lower friction coefficient of PAA-enriched surfaces is a surprising result considering that these surfaces show much higher adhesion against hydrophilic glass and tip surfaces with silicon dioxide composition. As known, classical theories of sliding contact mechanics and experimental results have led researchers to believe that generally stiff hydrophobic surfaces should exhibit the best tribological properties.[27,30] However, very recent work shows that at the micro and nanoscale, these theories break down because micro- or nanoscale contacts are dominated by capillary forces.[31] Water molecules adsorb on any surface exposed to air, becoming confined in these contacts. This thin layer (several monolayers depending upon humidity) is known to reduce friction since it acts as a lubrication layer and can prevent direct solid contact with the surface. Ahn et al. showed that the friction coefficient of a *hydrophilic* surface *decreased* with increasing humidity and even exhibited better tribological properties than more hydrophobic surfaces.[31] We suggest that for both **Y1** and **Y2** brush layers studied here, the low friction response after water exposure is caused by the presence of a thicker water film covering the glassy PAA, which is the topmost layer. With a PAA dominated surface possessing high water affinity, a more complete water layer forms. On the other hand, unlike PS chains in which T_g scales with M_n, for PAA chains with the low molecular weight studied here, a glass transition temperature still remains very high, close to 97°C.[32] Therefore, after treatment with water, a *glassy* PAA phase predominantly occupies the topmost surface layer reducing the contact area and, thus, friction forces.

The data presented in Figure 10 additionally supports this suggestion. The **Y1** brush layer, after water exposure, has a lower coefficient of friction at 80% RH compared to that at 30% RH (Fig. 5-10a). The wear properties are also better at 80% RH based on the AES depth profiles of the chemical composition. Compared to an original untested surface, the surface tested at 80% RH showed no decrease in carbon content, whereas the surface tested at 30% RH had a substantial loss of carbon content in the layer (Fig. 5-10b), which is evidence of polymer removal from the sliding area. AES also detected more

oxygen on the surface tested at 30% RH implying partial oxidation of the worn polymeric layer (Fig. 5-10b).

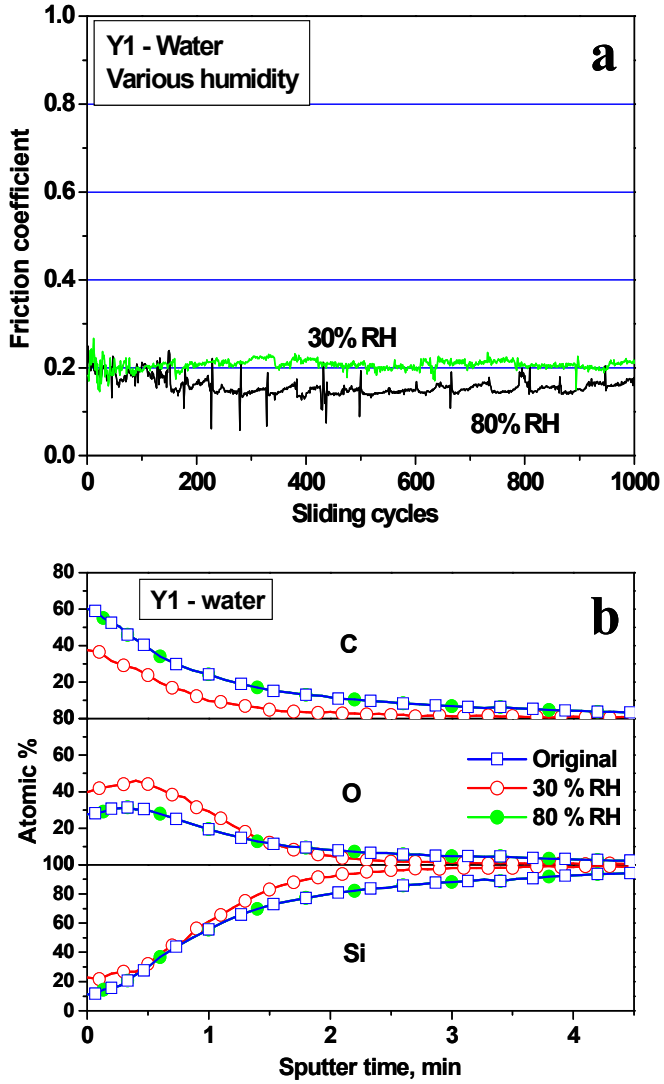

Figure 5-10. Data showing the effect of humidity on the microtribological properties. Friction coefficient as a function of sliding cycles is shown for Y1 (a) comparing results at 30% RH (green line) and 80% RH (black line). The AES depth profiles (b) reveal the higher material loss (in the form of less carbon for these polymeric materials) at 30% RH, compared to an original (untested) portion of the Y1 brush.

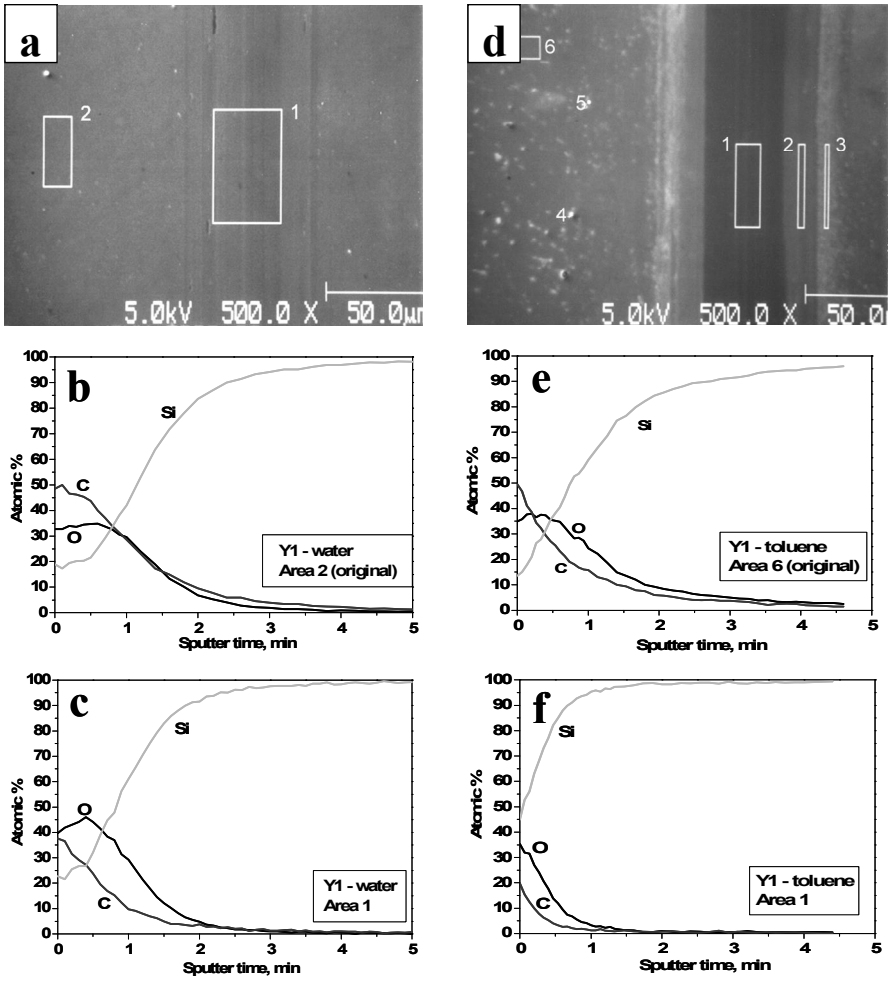

Figure 5-11. SEM images of the wear tracks from the microtribometer after testing Y1 in water (a) and toluene (d). In (a), Area 2 represents the accompanying AES analysis (b) of the original non-tested surface, while Area 1 is where the analysis of the worn area was taken from (c). For (d), the AES analysis from the original area (e) corresponds to Area 6, while the worn area analyzed (f) represents Area 1 in the SEM image

Finally, we compared the wear behavior of **Y1** brush layer after water and toluene exposure. SEM images of the wear tracks showed a striking contrast between different states (Fig 5-11a, 11d). After water exposure, there is very little visible damage to the surface in the sliding area. However, after toluene exposure, there is significant damage to the brush layer after testing under the same conditions, clearly visible in the SEM

image (Fig. 5-11d). The composition profiles comparing the initial and worn surfaces after water (Fig. 5-11b, 11c) and toluene exposure (Fig. 5-11e, 11f) are consistent with the SEM data. A much greater depletion of the carbon for the toluene-treated brushes, along with an increased silicon signal observed at low sputtering times, indicates nearly complete removal of the brush layer treated that was switched in toluene. After switching of brush layer by water treatment, a significant fraction of carbon is preserved within the worn area under similar conditions despite some visible wearing (Fig. 5-11c). Obviously, the switching of morphology and chain reorganization in response to selective solvents also correlated to changes in frictional behavior of the layer, an encouraging result for prospective NEMS applications in which the frictional behavior can be tuned in fluidic surroundings.

Conclusion

In conclusion, we have characterized the morphology and nanomechanical properties of the Y-shaped amphiphilic brushes in fluids as a function of chemical composition, and measured, for the first time, their tribological characteristics. AFM based nanomechanical testing has shown that the nanoscale reorganization greatly impacts the adhesion and elastic properties of the surface layer. This led to a bimodal distribution of the elastic modulus in water controlled by the relative amounts of PS and PAA on the surface. On the other hand, nanomechanical probing of the surface in toluene revealed a top layer completely dominated by PS. As a result of this reorganization, which agreed well with the molecular simulations, the Y-shaped brush exhibited variation of the friction and wear properties after exposure to different solvents. Unexpectedly, the microtribological properties were enhanced for a hydrophilic, PAA dominated surface, which showed low friction coefficient and higher wear stability despite higher adhesion and heterogeneous surface composition. We suggest that this unusual behavior is caused by the presence of thicker water layers on/within the PAA-enriched surface acting as a boundary lubricant, combined with the glassy state of the PAA chains in dry state.

Experimental

The chemical structure of the synthesized Y-shaped molecules **Y1** and **Y2** is presented in Figure 1, and the fabrication of chemically grafted layers is described in detail elsewhere.[17,18] The Y-shape brushes have one polystyrene (PS) arm, which is the hydrophobic component, and one poly(acrylic acid) (PAA) arm, which is hydrophilic, with varying number of monomeric units. **Y1** has asymmetric composition with longer chains (PS_{40}–PAA_{30}) while **Y2** is a symmetrical molecule (PS_{25}–PAA_{25}) as verified by NMR.[18] The Y-shaped molecules attached to a functional stem-like segment which is capable of covalent grafting to a functionalized silicon surface. The polymers were spin-coated from a 1.5 %wt. toluene solution onto the silicon wafers functionalized with the epoxysilane self-assembled monolayers.[33] The coated wafers were annealed at grafting temperatures ranging from 120˚C to 150˚C for 6 hours to enable the end groups to graft to the substrate. The initial microroughness of functionalized wafers did not exceed 0.2 nm within 1 μm x 1 μm surface area. Post-grafting hydrolysis of poly(*t*-butyl acrylate) arms imparts amphiphilicity to the brush. Molecular models and simulations were carried out using Materials Studio.[18] To switch the brushes, samples were immersed in good selective solvents for at least 12 hours to ensure full chain reorganization as verified with our previous study on switching kinetics.[19] Toluene is used as a good solvent for PS and water is used as a good solvent for PAA.

AFM studies in tapping mode under fluid were performed on a MultiMode (Nanoscope IIIa) microscope (Veeco Metrology) equipped with a fluid cell according to procedures adapted in our lab.[34] The fluid cell was modified with fluoro-elastomer tubing that would neither dissolve in organic solvents nor deposit any contamination on the sample. Probing of the surface nanomechanical properties was conducted directly in fluids after allowing for the equilibration with solvents using the usual force spectroscopy approach described previously.[35] Force-distance curves were obtained using the force-volume mode in 32x32 pixel arrays within 300x300 nm surface areas. The samples were scanned in tapping mode before and after force measurements to assure that no contamination, plastic deformation, or physical damage occurred during the application of

force. The data processing and calculation of the elastic modulus from the surface distributions of over 1000 force-distance curves were carried out in accordance with a multilayered Hertzian contact mechanics model described earlier.[35,36] For quantitative results, great care was taken to analyze the AFM tip characteristics. We used V-shaped cantilevers with a normal spring constant calculated to be 0.06 – 0.1 N/m.[37] Tip profile and radius (around 20 nm) was monitored by scanning a gold nanoparticle calibration standard.[38] The sensitivity of the system was measured before and after force measurements to ensure stability.

For microtribology studies, a custom-built microtribometer, effectively an oscillation friction and wear tester[39], was used to evaluate the frictional characteristics and to study the wear resistance of the Y-shaped brushes after treatments with the selective solvents. Before testing, the brushes were "switched" by exposure to the selective solvent for 12 hours, dried in ambient air under room temperature for 5 min., and immediately tested in the dry state. We used a 3 mm diameter glass ball (micro-roughness less than 1 nm) as the sliding counterpart over the stationary sample. The ball was ultrasonically cleaned in acetone and methanol for 30 min and dried with nitrogen prior to tests. The glass ball, mounted in a carrier head, was oscillated with an applied normal load of 200 μN, which corresponded to a maximum Hertzian pressure of 34.3 MPa. The sliding speed was 330 μm/s and the stroke length was 1.6 mm. The tests were conducted in a humidity-controlled chamber at 5%, 30%, and 80% relative humidity (RH). The chemical composition of the surfaces was probed with Auger electron spectroscopy (AES) on a PHI-670 instrument. AES surface analysis was performed using a field emission gun with an accelerating voltage of 5 kV and a current of 0.0185 μA. The working potential for depth sputtering was 1 kV using Ar-ion. Under this working condition, the sputtering rate was 7Å/min when calibrated against SiO_2.

References

[1] a) *Polymer Brushes* (Eds: R.C. Advincula, W.J. Brittain, K.C. Caster, J. Rühe), WILEY-VCH, Weinheim, Germany **2004**. b) B. Zhao, W.J. Brittain, *Prog. Polym. Sci*. **2000**, *25*, 677. c) B. Zhao, W.J. Brittain, W. Zhou, S. Z. D. Cheng, *J. Am. Chem. Soc.* **2000**, *122*, 2407. d) I. Luzinov, S. Minko, V.V. Tsukruk, *Prog. Polym. Sci.* **2004**, *29*, 635. e) A. Halperin, M. Tirrell, T.P. Lodge, *Adv. Polym. Sci.* **1992**, *100*, 31. f) T.P. Russell, *Science* **2002**, *297*, 964.

[2] a) G.S. Grest, M. Murat, *Macromolecules* **1993**, *26*, 3108. b) V. Koutsos, E.W. van der Vegte, G. Hadziioannou, *Macromolecules* **1999**, *32*, 1233. c) X. Guo, A. Weiss, M. Balluff, *Macromolecules* **1999**, *32*, 6043.

[3] Y. Ito, Y. Ochiai, Y.S. Park, Y. Imanishi, *J. Am. Chem. Soc.* **1997**, *119*, 1619.

[4] M.E. Harmon, D. Kuckling, C.W. Frank, *Langmuir* **2003**, *19*, 10660. b) B. Yang, W. Yang, *J. Mem. Science* **2003**, *218*, 247. c) H. Tu, C.E. Heitzman, P.V. Braun, *Langmuir* **2004,** *20,* 8313.

[5] M. Lee, J.-W. Kim, Y.-S. Yoo, S. Peleshanko, K. Larson, D. Vaknin, S. Markutsya, V.V. Tsukruk, *J. Am. Chem. Soc.* **2002**, *124*, 9121.

[6] M. Irie, *Adv. Polym. Sci.* **1990**, 94, 27. b) L. Ionov, M. Stamm, S. Minko, F. Hoffmann, T. Wolff, *Macromol. Symp.* **2004,** *210*, 229.

[7] a) B. Zhao, W.J. Brittain, *Macromolecules* **2000**, *33*, 8813. b) J.-B. Kim, W. Huang, M.L. Bruening, G.L. Baker, *Macromolecules* **2002**, *35*, 5410. c) E.B. Zhulina, C. Singh, A.C. Balazs, *Macromolecules* **1996**, *29*, 8254.

[8] a) A. Sidorenko, S. Minko, K. Schenk-Meuser, H. Duschner, M. Stamm, *Langmuir* **1999**, *15*, 8349. b) S. Minko, S. Patil, V. Datsyuk, F. Simon, K.J. Eichorn, M. Motornov, D. Usov, I. Tokarev, M. Stamm, *Langmuir* **2002**, *18*, 289. c) M. LeMieux, D. Usov, S. Minko, M. Stamm, H. Shulha, V.V. Tsukruk, *Macromolecules* **2003**, *36*, 7244. d) M.C. LeMieux, D. Julthongpiput, K.N. Bergman, P.D. Cuong, H.-S. Ahn, Y.-H. Lin, V.V. Tsukruk, *Langmuir* **2004**, *20*, 10046.

[9] a) M. Motornov, S. Minko, K.J. Eichorn, M. Nitschke, F. Simon, M. Stamm, *Langmuir* **2003**, *19*, 8077. b) J.-F. Joanny, *Langmuir* **1992**, *8*, 989. c) J. Klein, Y. Kamiyama, H. Yoshizawa, J.N. Israelachvili, G.H. Fredrickson, P. Pincus, L.J.

Fetters, *Macromolecules* **1993**, *26*, 5552. d) L. Léger, E. Raphaël, H. Hervet, *Adv. Polym. Sci.* **1999**, *138*, 186. e) T. Kreer, M.H. Muser, *Wear* **2003**, *25,* 827.

[10] a) S.T. Milner, *Science* **1991**, *251*, 905. b) A.C. Balazs, C. Singh, E. Zhulina, S.-S. Chern, Y. Lyatskaya, G. Pickett, *Prog. Poly. Sci.* **1997**, *55*, 181. c) B. Zhao, W.J. Brittain, *Macromolecules* **2000**, *33*, 342.

[11] J.F. Marko, T.A. Witten, *Phys. Rev. Lett.* **1991**, *66*, 1541.

[12] a) B. Zhao, *Langmuir* **2004**, *20*, 11748. b) B. Zhao, R.T. Haasch, S. MacLaren, *Polymer* **2004**, *45*, 7979.

[13] a) S. Minko, M. Müller, D. Usov, A. Scholl, C. Froeck, M. Stamm, *Phys. Rev. Lett.* **2002**, *88*, 035502-1. b) M. Müller, *Phys. Rev. E* **2002**, *65*, 030802-1. c) G.E. Yakubov, B. Loppinet, H. Zhang, J. Rühe, R. Sigel, G. Fytas, *Phys. Rev. Lett.* **2004**, *92*, 115501-1.

[14] M.O. Gallyamov, B. Tartsch, A.R. Khokhlov, S.S. Sheiko, H.G. Börner, K. Matyjaszewski, M. Möller, *Chem. Eur. J.* **2004**, *10*, 4599.

[15] a) C. Singh, A.C., Balazs, *Macromolecules* **1996**, *29*, 8904. b) E.B. Zhulina, A.C. Balazs, *Macromolecules* **1996**, *29*, 2667.

[16] A. Stamouli, E. Pelletier, V. Koutsos, E. van der Vegte, G. Hadziioannou, *Langmuir*, **1996**, *12*, 3221.

[17] J. Teng, E.R. Zubarev, *J. Am. Chem. Soc.* **2003**, *125*, 11840.

[18] D. Julthongpiput, Y.-H. Lin, J. Teng, E.R. Zubarev, V.V. Tsukruk, *Langmuir* **2003,** *19*, 7832.

[19] D. Julthongpiput, Y.-H. Lin, J. Teng, E.R. Zubarev, V.V. Tsukruk, *J. Am. Chem. Soc.* **2003**, *125*, 15912.

[20] Y.-H. Lin, J. Teng, E. R. Zubarev, H. Shulha, V. V. Tsukruk, *Nano Lett.*, **2005**, 5, 491.

[21] S.J. Alexander, *J. Phys.* **1977**, *38*, 977.

[22] W. Zhang, X. Zhang, *Prog. Polym. Sci.* **2003,** *28,* 1271.

[23] Z. Huang, S.A. Chizhik, V.V. Gorbunov, *J. Mat. Sci.* **1998**, *33*, 4905.

[24] H. Shulha, A. Kovalev, N. Myshkin, V. V. Tsukruk *Eur. Polym. J.* **2004**, *40,* 949.

[25] V. V. Tsukruk, *Adv. Mater.,* **2001***, 13,* 95.

[26] A. Sidorenko, H.-S. Ahn, D.-I. Kim, H. Yang, V. V. Tsukruk, *Wear* **2002**, *252*, 946.

[27] *Microstructure and Microtribology of Polymer Surfaces* (Eds. V. V. Tsukruk, K. Wahl) ACS Symposium Series, Washington DC, v.741, **2000**.

[28] *Fundamentals of friction: macroscopic and microscopic processes* (Eds: I.L. Singer, H.M. Pollack) KLUWER ACADEMIC, Boston **1992**.

[29] T.G. Fox, P.J. Flory, *J. Chem. Phys.* **1950**, *21*, 581.

[30] H. Ahn, D. Julthongpiput, Doo-In Kim, V. V. Tsukruk, *Wear* **2003,** *255,* 801.

[31] D.I. Kim, H.S. Ahn, D.H. Choi *Appl. Phys. Lett,* **2004,** *84*, 1919.

[32] J.M.G. Cowie, I.J. McEwen, M.T. Garay, *Eur. Polym. J.* **1987**, *23*, 917.

[33] I. Luzinov, D. Julthongpiput, A. Liebmann-Vinson, T. Cregger, M. D. Foster, V. V. Tsukruk, *Langmuir*, **2000**, *16*, 504.

[34] V.V. Tsukruk, *Rub. Chem. Technol.* **1997**, *70*, 430.

[35] A. Kovalev, H. Shulha, M. LeMieux, N. Myshkin, V.V. Tsukruk, *J. Mater. Res.* **2004**, *19*, 716.

[36] V.V. Tsukruk, A. Sidorenko, V.V. Gorbunov, S.A. Chizhik, S. A., *Langmuir* **2001**, *17*, 6715.

[37] J.L. Hazel, V.V. Tsukruk, *Thin Solid Films* **1999**, *339*, 249.

[38] a) V.V. Tsukruk, V. Gorbunov, *Microsc. Today* **2001**, 01-1, 8. b) M. Radmacher, R.W. Tillmann, H.E. Gaub, H.E., *Biophys. J.* **1993**, *64*, 735.

[39] D. Julthongpiput, H. Ahn, D. Kim, V.V. Tsukruk, *Tribol. Lett.* **2002**, *13*, 35.

CHAPTER 6
CONTROLLING SELECTIVE ADSORPTION ON PATTERENED GRADIENT Y-SHAPED AMPHIPHILIC BRUSHES

A paper published in Responsive Polymers (Book chapter), Ed. Blackwell Professional, 2006

Y. H. Lin, J. Teng, E. R. Zubarev, S. Peleshanko, V. V. Tsukruk

Department of Materials Science & Engineering, Iowa State University, Ames, 50011 IA

Abstract

We demonstrated that by tuning the grafting density and by applying different solvent treatments to the micropatterned Y-shaped PS-PAA brushes,the density and the type of the surface adsorption of gold nanoparticles can be varied in a wide range creating surface micropatterns with a variable contrast. The selective adsorption of gold nanoparticles and their surface aggregation are controlled by Coulombic interactions between positively charged gold nanoparticles and PAA arms. Surface composition of Y-shaped brush layers which is a critical factor in tuning nanoparticles adsorption undergoes significant surface reorganization upon treatments with selective solvents which is affected by the grafting density. Mixed state of the Y-shaped brush layers provided the best conditions for surface adsorption and aggregation in the form of nanoscale clusters of Au particles.

Introduction

The fabrication of robust surface layers from mixed, binary brushes grafted to a solid substrate was reported in a number of recent publications.

♦ Primary researcher; carried out most of experiments, writer of all drafts.

[1,2,3,4,5,6,7,8] Surface composition of these brush layers and, hence, their adsorption properties can be "tuned" to a desired physical state.[9,10] A novel type of such binary brushes, so-called Y-shaped brushes, combining two dissimilar polymer chains (polystyrene (PS) and polyacrylic acid (PAA)) attached to a single focal point were introduced in our previous publications (Figure 6-1).[11,12,13] Their ability to change surface morphology and, thus, the surface wettability has been demonstrated. Such reorganizations are crucially important for the controlling the surface properties such as nanotribological behavior (adhesion and friction, as will be reported elsewhere) and selective ability to adsorb and retain inorganic nanoparticles with appropriate chemical composition.

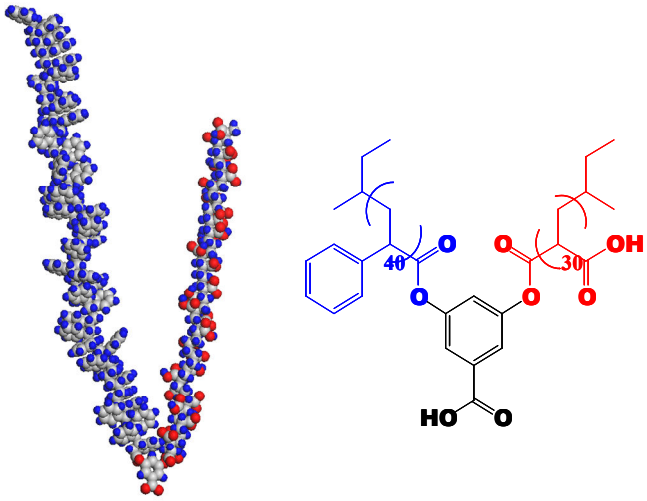

Figure 6-1. Chemical structure and molecular graphics representation of Y-shaped block copolymers with short aromatic functional stem. Molecules contain 40 and 30 monomeric units in PS and PAA arms, respectively.

In this communication, we report on the first example of controlled selective adsorption of positively charged gold nanoparticles on micropatterned Y-shaped brush layer with exposed negatively charged PAA arms in selected surface areas alternating with "neutral" areas. We demonstrated that the type and density of selective adsorption (e.g., individual or aggregated nanoparticles) are influenced by the grafting density of the Y-shaped layers and their conformational rearrangements in selective solvents. Corresponding

changes in surface morphology are visualized through surface micropatterning with a gradient of grafting density.

Experimental

The synthesis of the Y-shaped molecules presented in Figure 1 and the fabrication of chemically grafted layers followed to their hydrolization to PS-PAA are described in detail elsewhere.[11,12] Gradient surface layers were fabricated by placing the patterned substrate in temperature gradient during grafting routine according to an approach proposed by Karim et al. (Figure 2).[14,15] Temperature gradient from 150^{o}C at the edges to 25^{o}C at the center of the substrate provided the variation from dense grafting at the edges to loose grafting at the center. Micropatterning with alternating methyl-terminated octadecyltrichlorosilane (OTS) self-assembled monolayer (SAM) and epoxy-terminated ((3-glycidoxypropyl) trimethoxysilane, GPS) SAM surface areas with a spacing of 10 □m was conducted according to usual microstamping procedure combined with SAM grafting.[16,17] Y-shaped brushes were grafted to the epoxy-terminated surface areas while leaving untouched OTS protected areas, thus, creating alternating PS-PAA Y-shaped brush and OTS areas (Figure 6-2). Gold nanoparticles with a diameter of 5 nm were modified with poly(diallylimethylammonium chloride, M_w = 100, 000) (Aldrich) to induce positive surface charge according to the procedure.[18] Nanoparticle adsorption was conducted in 0.1M α,α,α-tris-(hydroxymethyl)-methylamine (TRIS) buffer (pH=9) for an hour . The samples after adsorption were washed several times with TRIS buffer and ethanol to remove weakly tethered gold nanoparticle. Atomic force microscopy (AFM) studies in tapping mode were performed on a Multimode and Dimension 3000, Nanoscope IIIa microscopes (Digital Instruments, Inc.) according to procedures adapted in our lab.[19] Optical microscopy was performed using a Van Guard 1282 microscope in epi-fluorescence mode. A JEOL JSM-6060LV was used for scanning electron microscopy (SEM) studies.

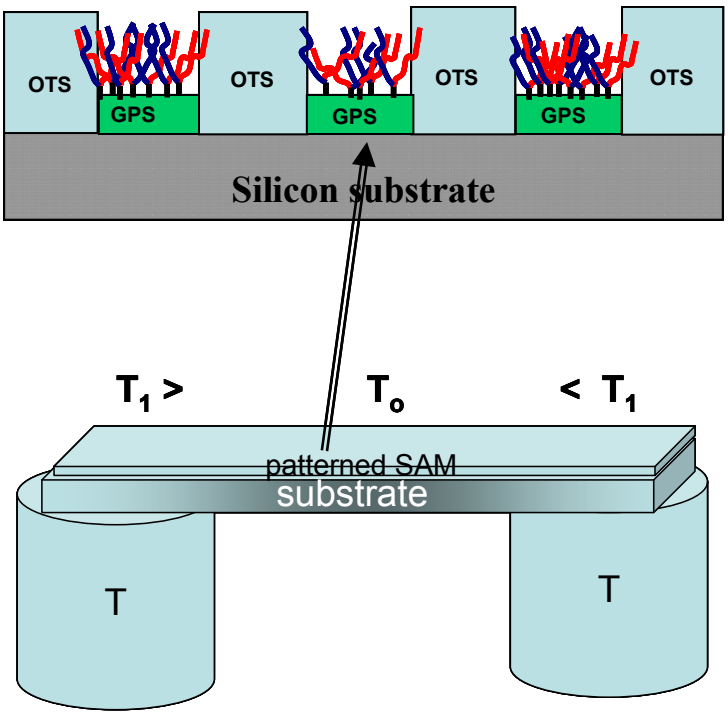

Figure 6-2. Schematics of gradient grafting routine in temperature gradient (bottom) and expected topography of micropatterned surface with alternating OTS and GPS layers and Y-shaped brushes grafted on GPS surfaces (top).

Results and discussion

The topography of the micropatterned surface displayed a clear alternation of the elevated stripes with sharp boundaries and smooth surfaces that measured about 3 □m in width for the elevated areas (Figure 6-3a). This regular pattern is formed by the alternating OTS and epoxy-terminated SAMs with different elevations caused by the difference in the length of the alkylsilane molecules forming the monolayers (Figure 6-2). The difference in heights between these areas was measured from the corresponding cross-sections and was found to be about 1.8 nm (Figure 3). This value was fairly close to that expected (1.4 – 1.9 nm) for difference between the known thicknesses of OTS (2.3-2.5 nm) and GPS (0.6-0.9 nm) SAMs. The chemical grafting of the Y-shaped molecules to the GPS SAMs in deep grooves between the OTS areas resulted in their effective "filling", which was easy to follow by collecting the topographical images in different surface locations (Figure 6-3). In

fact, in the densely drafted region (the edges of the specimens), we observed almost completely smoothened surface topography indicating the total thickness of Y-shaped layers grafted to the GPS surface of about 1.8 nm. This value indicates vertical grafting of the arms (brush regime) in a collapsed state (dry conditions) and is close to their thickness on the uniform substrates as was measured earlier.[13] In contrast, Y-shaped brushes with a lower grafting density "refilled" the GPS grooves only partially, leaving a detectable initial footprint with the height difference of about 1 nm in the central regions of the specimen (Figure 6-3c). This difference indicates the effective thickness of the loosely packed Y-shaped brush layers of 0.8 nm and, thus, very low density of grafting which results in virtually flat arrangement of the brush arms (pancake-like regime).

Adsorption of the gold nanoparticles was probed on both water and toluene pre-treated micropatterned surfaces. The gold nanoparticles did not adhere to the surface dominated by PS arms (Y-shaped brush areas) and methyl groups (OTS areas) after toluene treatment. However, a dense gold monolayer was observed on the patterned surface after preceding water treatment (see SEM and fluorescence microscopy images of patterned surfaces for long-range contrast in Figure 6-4). In this case, the negatively charged PAA arms dominated the surface of the Y-shaped brushes and strong Coulombic interactions became responsible for selective adsorption of positively charged gold nanoparticles on predominantly negatively Y-shaped surface areas. The density of gold monolayers is high enough to create excellent contrast persisting over large range in lateral dimensions (>200 μm) as detected by fluorescence optical microscopy and SEM (Figure 6-4). Virtually no gold nanoparticles were observed on methyl-terminated OTS surfaces alternating with Y-shaped brush areas, and this selectivity of the nanoparticles adsorption dramatically enhanced the periodic contrast.

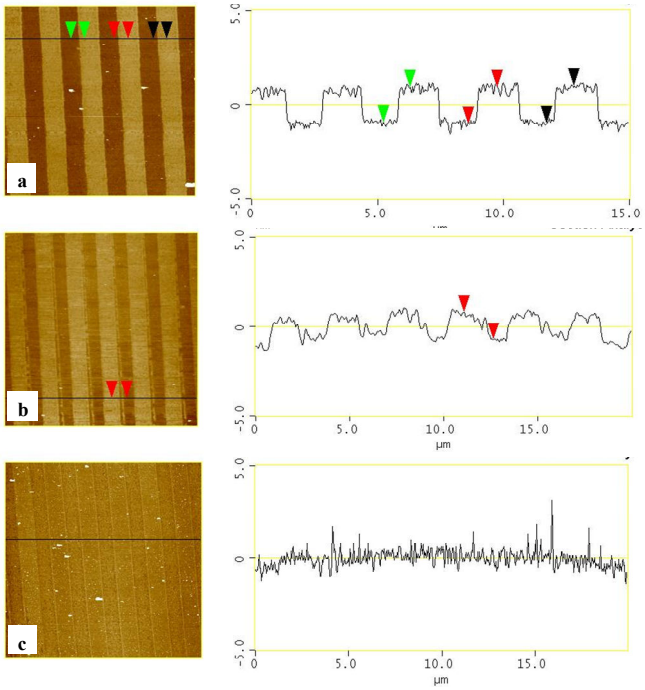

Figure 6-3. AFM images and corresponding cross-sections of initial micropatterned OTS-GPS surface (a), micropatterned OTS-GPS surface with high (b, the edge of the sample) and low (c, the center of the substrate) densities of Y-shaped brush grafting.

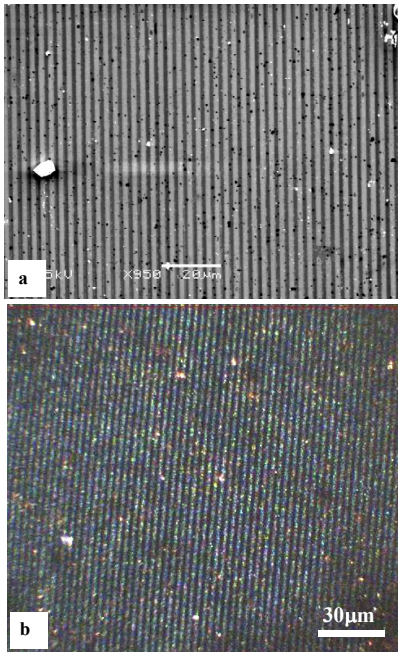

Figure 6-4. Large-scale images of micropatterned surface: (a) SEM; (b) fluorescence microscopy.

The AFM imaging showed a medium to high density of the packing of individual gold nanoparticles and their aggregates on the surface of PS-PAA brushes (Figure 6-5). The phase contrast between OTS areas and gold-coated Y-shaped brush areas showed very different adhesive and elastic properties of purely organic and neutral (OTS) and organic-inorganic highly charged (gold nanoparticles-Y-shaped brushes) surface areas even if though the overall thickness was nearly the same and close to 2.3 nm (Figure 6-5). The overall density of nanoparticles packing was slightly higher for the micropatterned surface in the central location with lower grafting density of Y-shaped layers and the morphology of the adsorbed nanoparticles layer was very different.

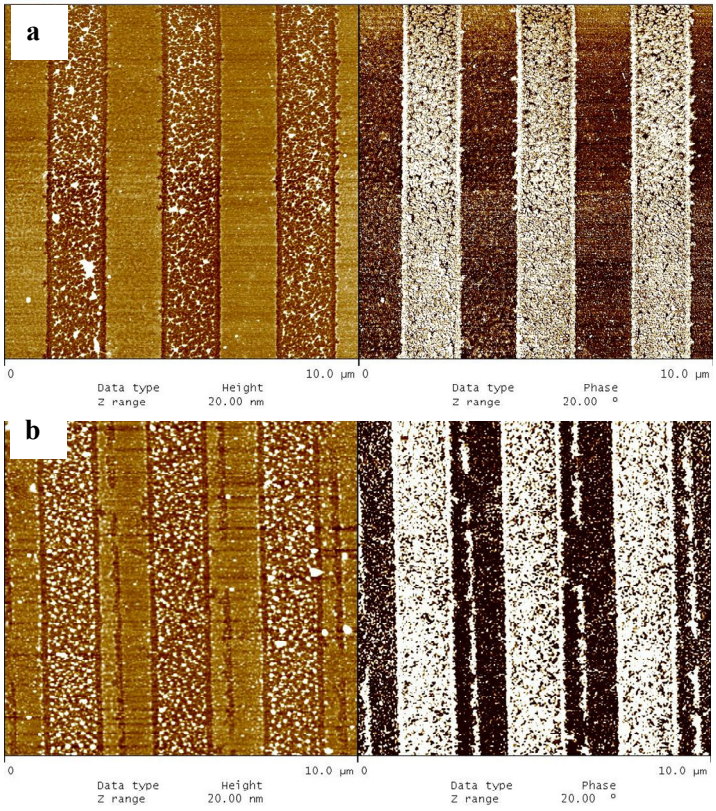

Figure 6-5 AFM images of micropatterned surfaces with adsorbed gold nanoparticles (left-topography and right-phase) for densely (a) and loosely (b) grafted Y-shaped brush layers.

In fact, higher-resolution AFM images showed very different aggregation behavior of gold nanoparticles adsorbed on high and low density Y-shaped brush layers (Figure 6-6). The densely populated gold nanoparticles and their surface aggregates are observed on loosely packed Y-shaped brush layers with lateral sizes of the nanoparticles aggregates in the range of 30-100 nm (after correction for the tip dilation) indicating a large aggregation number reaching several hundred nanoparticles per aggregate (Figure 6-6a). By way of contrast, a low concentration of nanoparticles was observed in densely packed Y-shaped surface areas (Figure 6-6b). Gold nanoparticles were sparsely distributed on the surface in a chain-like manner forming a low-density network. The lateral sizes of the adsorbates were below 15 nm indicating a very low number of aggregated nanoparticles in a single cluster not exceeding several tens. In both cases, the height of the aggregates did not exceed 5-6 nm (Figure 6-7) that corresponds to a single monolayer of gold nanoparticles with a diameter of 5 nm.

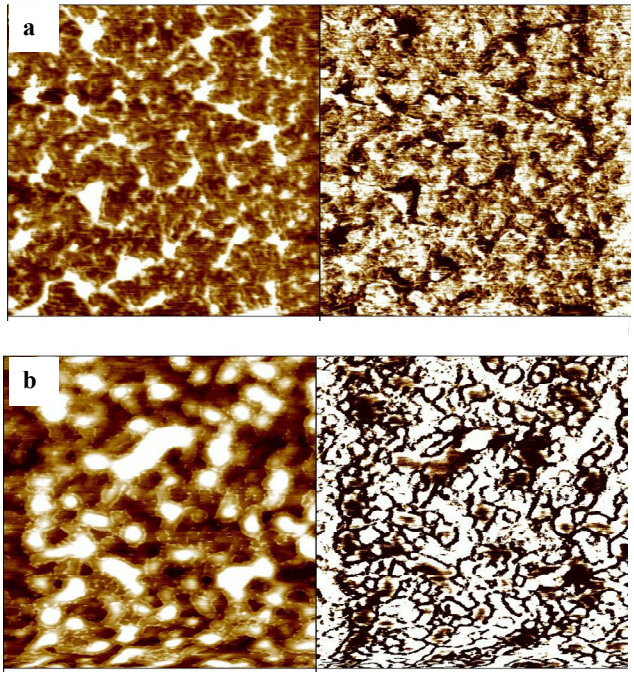

Figure 6-6. AFM images of micropatterned surfaces with adsorbed gold nanoparticles (left-topography and right-phase) for densely (a) and loosely (b) grafted Y-shaped brush layers.

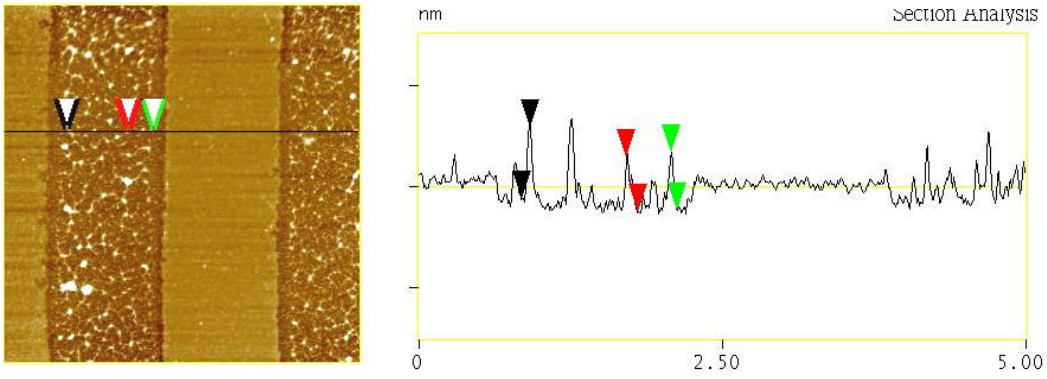

Figure 6-7. AFM topographical image of micropatterned surfaces with adsorbed gold nanoparticles and corresponding cross-section.

Obviously, the different morphology of the Y-shaped brush surface areas caused by variation in the grafting density of binary molecules is critical for the adsorption behavior and modes of aggregation of gold nanoparticles. We can expect that in both cases, the PAA arms should occupy the topmost location after water treatment as was discussed and modeled in our previous publications.[13] However, in the case of low grafting density, the Y-shaped molecules cannot adopt a predominantly vertical orientation (far from the brush-like regime) and instead spread out along the surface covering it with both PAA and PS arms arranged horizontally (pancake regime). As a result, the PAA arms may no longer collapse and/or become obscured by the PS arms, and that should maximize their overall exposure. This surface composition promotes intensive adsorption of the gold nanoparticles and their dense aggregation with submicron lateral dimensions. On the other hand, for densely packed Y-shaped brushes, PAA chains remain screened by PS chains even after treatment with water due to unfavorable volume composition (60 % PS) and 30 %-higher length of PS arms.[13] This "incomplete" surface coverage with PAA arms and the mixed state of the Y-shaped layers cause significant reduction of the overall Coulombic interactions. As a result, only few gold nanoparticles are still adsorbed to localized surface areas, and stay firmly tethered to these PAA-enriched regions. This mixed state may also be responsible for preventing large-scale aggregation of gold nanoparticles due to

surrounding hydrophobic PS-enriched surface areas and stabilization of the nano-sized clusters.

Conclusion

In conclusion, we demonstrated that the variation of the grafting density and selective solvent treatment of the micropatterned Y-shaped brushes influence the density and the modes of surface adsorption of gold nanoparticles creating micropatterns with variable contrast. This behavior is controlled by Coulombic interactions between oppositely charged gold nanoparticles and PAA arms. The surface morphology of the PAA arms is controlled by the grafting density and conformational reorganization caused by selective solvents. These two factors play a critical and synergistic role in selective adsorption of charged species and following surface aggregation that allow for tuning their surface distribution and the degree of aggregation.

Acknowledgements

We acknowledge support by the National Science Foundation, CMS-0099868. The authors thank M. Ornatska, H. Ko, and M. Lemieux for fruitful discussions.

References

[1] S. Minko, M. Mueller, M. Motornov, M. Nitschke, K, Grundke, M. Stamm *J. Am. Chem. Soc*, **2003**, *125*, 3896.

[2] A. Sidorenko, S. Minko, K. Schenk-Meuser, H. Duschner, M. Stamm *Langmuir*, **1999,** *15*, 8349.

[3] B. Zhao, W. J. Brittain, W. Zhou, S. Z. D. Cheng, *J. Am. Chem. Soc* **2000**. *122*, 2407.

[4] M. Ruths, D. Johannsmann, J. Ruehe, W. Knoll *Macromolecules,* **2000**, *33*, 3860.

[5] Zhao, Bin; Brittain, William J. *Prog. Polym. Sci* **2000,** *25*, 677.

[6] M. Müller *Phys. Rev. E* **2002,** *65*, 030802.

[7] M. C. LeMieux, D. Usov, S. Minko, M. Stamm, H. Shulha, V. V. Tsukruk, **2003**. *Macromolecules 36*, 7244.

[8] B. Zhao *Polymer* **2003**, *44*, 4079.

[9] I. Luzinov, S. Minko, V. V. Tsukruk, *Prog. Polym. Sci* **2004**, *29*, 635.

[10] E. Zhulina, A. C. Balazs *Macromolecules* **1996**, *29*, 2667.

[11] J. Teng, E. R. Zubarev *J. Am. Chem.* Soc, **2003,** *125*, 11840.

[12] D. Julthongpiput, Y.-H. Lin, J. Teng, E. R. Zubarev, V. V. Tsukruk *Langmuir* **2003** *19*, 7832.

[13] D. Julthongpiput, Y.-H. Lin, J. Teng, E. R. Zubarev, V. V. Tsukruk. *J. Am. Chem. Soc*, **2003,** *125***,** 15912.

[14] J. C. Meredith, A. P. Smith, A. Karim, E. J. Amis *Macromolecules* **2000**.*33*, 9747.

[15] L. Ionov, B. Zdyrko, A. Sidorenko, S. Minko, V. Klep, I. Luzinov, M. Stamm,. *Macromol. Rapid Commun,* **2004**. *25*, 360.

[16] I. Luzinov, D. Julthongpiput, A. Liebmann-Vinson, T. Cregger, M. D. Foster, V. V. Tsukruk *Langmuir* **2000**, *16,* 504.

[17] M. Geissler, Y. Xia *Adv. Mater.* **2004,** *16*, 1249.

[18] K. S. Mayya, B. Schoeler, F. Caruso *Adv. Funct. Mater* **2003,** *13*, 183.

[19] V. V. Tsukruk, *Rubber Chem. Technol*. **1997,** *70*, 430.

CHAPTER 7
TRI-LAYERED CERAMIC-METAL-POLYMER MICROCANTILEVERS WITH DRAMATICALLY ENHANCED THERMAL SENSITIVITY

A paper published in Advanced Functional Materials 2006, 18, 1157-1161

Yen-Hsi Lin, Michael E. McConney, Melburne C. LeMieux, Sergiy Peleshanko, Chaoyang Jiang, Srikanth Singamaneni, Vladimir V. Tsukruk

Department of Materials Science & Engineering, Iowa State University, Ames, 50011 IA

Introduction

The highly sensitive microcantilever sensors have a broad range of applicability for detecting diverse physical phenomena such as temperature, heat, magnet fields, mass, and stress [1,2,3,4,5] The applications of microcantilever sensors exploit the advantages which are offered by their microscopic dimensions, high sensitivity, easy fabrication, batch processing, and direct transduction.[6,7] Although microcantilevers themselves are fabricated via conventional photolithography from silicon and silicon nitride, to assure specific chemical and biological interactions, surface modification is required to detect and absorb appropriate chemical groups. At present, different techniques have been reported to modify silicon-based microcantilevers with an organic or polymer coating for different sensing capabilities. For example, microcantilever modification was conducted by using spin coated films[8] self-assembled monolayers,[9] layer-by-layer assembly[10,11], hydrogel layers[12,13] and polymer brush layers[14].

♦ Primary researcher; carried out majority of experiments, writer of all drafts.

Microcantilever sensors designed for thermal detection have been recently introduced for uncooled IR detection and imaging.[15,16,17,18,19] The design uses the well-known phenomenon of temperature-induced bending of bilayered beams composed of two materials with very different thermal expansion coefficients. The most common bimaterial design utilizes a silicon beam with a metallic coating, which is usually gold or aluminum, as these materials are readily proccessable.[20,21] Thermally induced stresses result in reversible bending of microcantilevers with measurements of cantilever deflections detected via various readout schemes such as laser beam deflection (Fig. 7-1).[4] Previous studies have reported that bimetallic microcantilevers had high sensitivity to ambient temperature changes as well as to absorbed IR photons.[22,23] These bimetallic microcantilevers are considered to be a promising platform for the microfabrication of highly sensitive uncooled IR detectors.[20] Polymers as layer with high thermal expansion have been considered but not applied because their perceived low mechanical strength and poor chemical affinity to metal surfaces. Moreover, polymer processing of cantilevers leads to damage, and large stresses within the polymer-silicon beams.

With sensitive optical or electrostatic readouts, the microcantilever-based devices can show resolution of several tens of mK with thermal sensitivity, S, (beam deflection per degree) reaching hundred nm/K for microcantilevers with the length around hundred microns. These characteristics are sufficient for the fabrication of medium resolution uncooled IR imaging arrays with promising spatial, thermal, and temporal characteristics.[24,25] However, to make significant progress in the miniaturization of these devices and, most importantly, increasing their sensitivity below the limits of modern cooled solid state sensors (below 10 mK), thermal sensitivity should be increased significantly. Considering that the difference of thermal expansion coefficients between the metal and ceramic materials constituting the bimorph is inherently limited and the thickness of metal layer cannot be increased significantly without compromising sensitivity and uniformity, other materials should be envisioned to enhance thermal bending ability of metal-silicon beam microstructures.

Therefore, we suggest a novel approach to design thermally-sensitive microcantilevers by fabricating *trilayer* ceramic-metal-polymer beams with enhanced thermal bending ability by adding the topmost strong, chemically grafted polymer nanocomposite layers (Fig. 7-1). [26,27,28,29] The topmost polymer nanocomposite layer with thermal expansion about two orders of magnitude higher than that for the gold layer in conjunction with its low thermal conductivity should provide for enhanced thermal sensitivity according to theoretical estimation.[21] To increase mechanical strength of this layer beyond usual limits, it has been reinforced with silver nanoparticles and carbon nanotubes and to increase stress transfer to underlying beam polymer nanocomposite nanolayer was chemically grafted to the gold surface via a bi-functional self-assembled monolayer (SAM). [30,31]

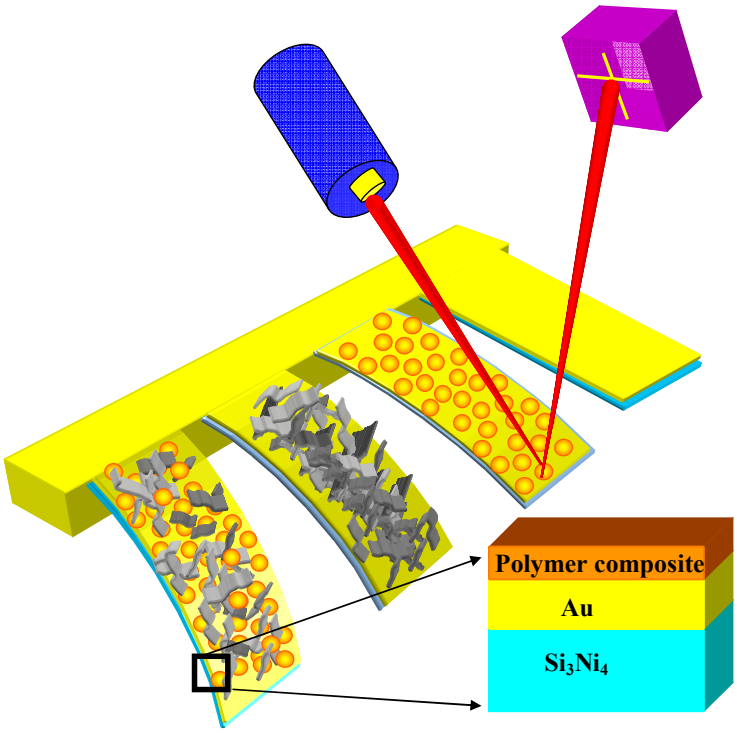

Figure 7-1. A schematics of a microcantilevers with optical readout and trilayered composition. Silicon nitride-gold microcantilever cantilevers modified with grafted polymeric layer reinforced with different nanoparticles.

For this study, we utilized rectangular and V-shaped silicon nitride-gold microcantilevers with the length 200 and 310 μm and spring constants in the range 0.02-0.03 N/m (as measured by thermal tuning) coated with the gold layer (Table 7-1). As polymeric materials we used end-functionalized poly(arylonitirle) (PAN) and polystyrene (PS) with the thermal expansion coefficient of 68-100 $x10^{-6}$ K^{-1} grafted to the gold layer via the cysteamine SAM and reinforced with highly dispersed single-walled carbon nanotube (SWCNTs) bundles and Ag nanoparticles (see Experimental, Fig. 7-1). PAN with high chemical and solvent resistance is commonly used with activated carbon for the variety of applications.[32]

Results and Disscusion

Figure 2 shows AFM topographic images of different nanocomposite layer directly scanned on the chip part of the microcantilevers. The microroughness of the topmost gold layer for uncoated microcantilevers was 3 nm (within a 10x10 μm surface area) and the microroughness of the polymer modified microcantilever increased to 10-12 nm. However, the surface morphology remained uniform with fine grainy nodes caused by Ag nanoparticles aggregation (Fig. 7-2b). SWNT formed dispersed aggregates at SAM surface but the final nanocomposite layer showed relatively smooth and uniform morphology due to encapsulating of carbon nanotubes into PS layer (Figs. 7-2c,d). The thickness of the polymer nanocomposite layers was obtained from AFM imaging of the micropatterned layers and was found to be in the range of 10-14 nm for all polymer layers fabricated here.

Raman spectroscopy with a confocal microscope conducted for the polymer composite layer was used to confirm independently the chemical composition of the topmost layer and the presence of carbon nanotube (Fig. 7-3). Raman micromapping was conducted by integrating intensity at 1590 cm^{-1} (a G-mode which ia a main resonance peak for carbon nanotubes) (Fig. 7-3c). [33,34] As an example, we present a Raman image for the polymer layer in the vicinity of the triangular microcantilever (Fig. 7-3b). The Raman

footprint shows the triangular shape which confirms the presence of carbon nanotubes embedded in the polymer matrix.

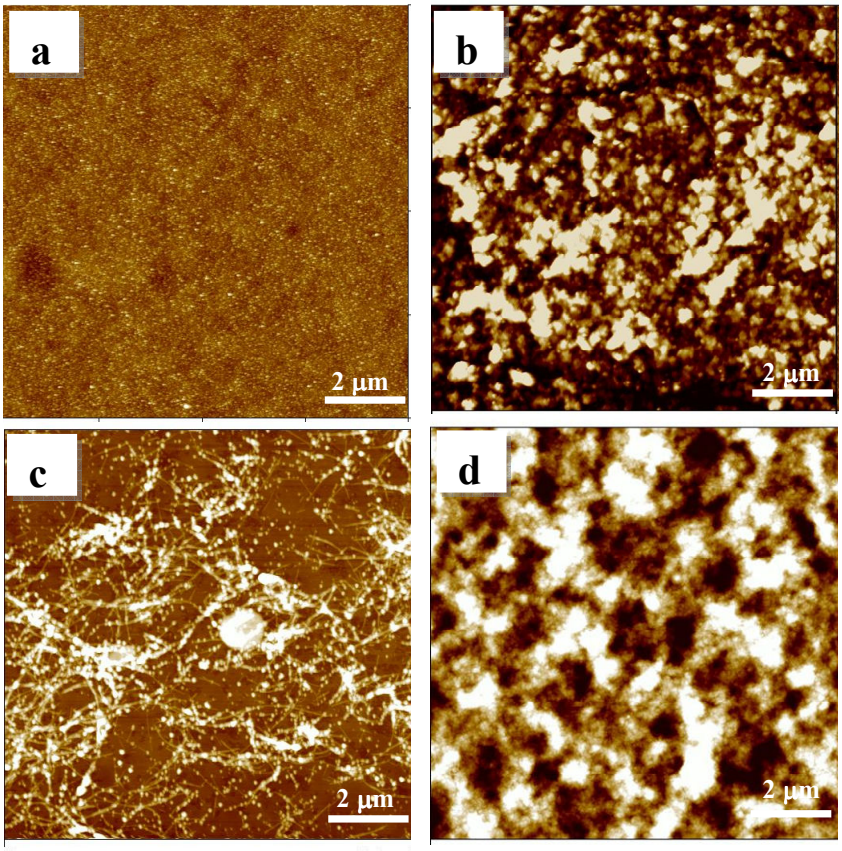

Figure 7-2. AFM images of different surfaces: (a) gold coating of an unmodified microcantilever (b) Ag/PAN topmost layer (c) Cysteamine SAM/SWNT layer (d) SAM/SWNT/PS/Ag/PAN layer. Z-scale is 60 nm.

The microcantilever deflection as a function of the temperature variation for four different microcantilevers is presented in Fig. 4 and corresponding characteristics are given in Table 1. First, it is worth to note that the grafting procedure and added topmost polymer layer do not compromise the general microcantilever characteristics. E.g., for the rectangular cantilevers a spring constant stays within 0.027-0.031 N/m, resonance frequency varies within 13.3-15.6 kHz, and the quality factor is within 23-26 (Table 7-1).

However, thermal bending ability changed dramatically after adding the polymer nanocomposite layer (Fig. 7-4).

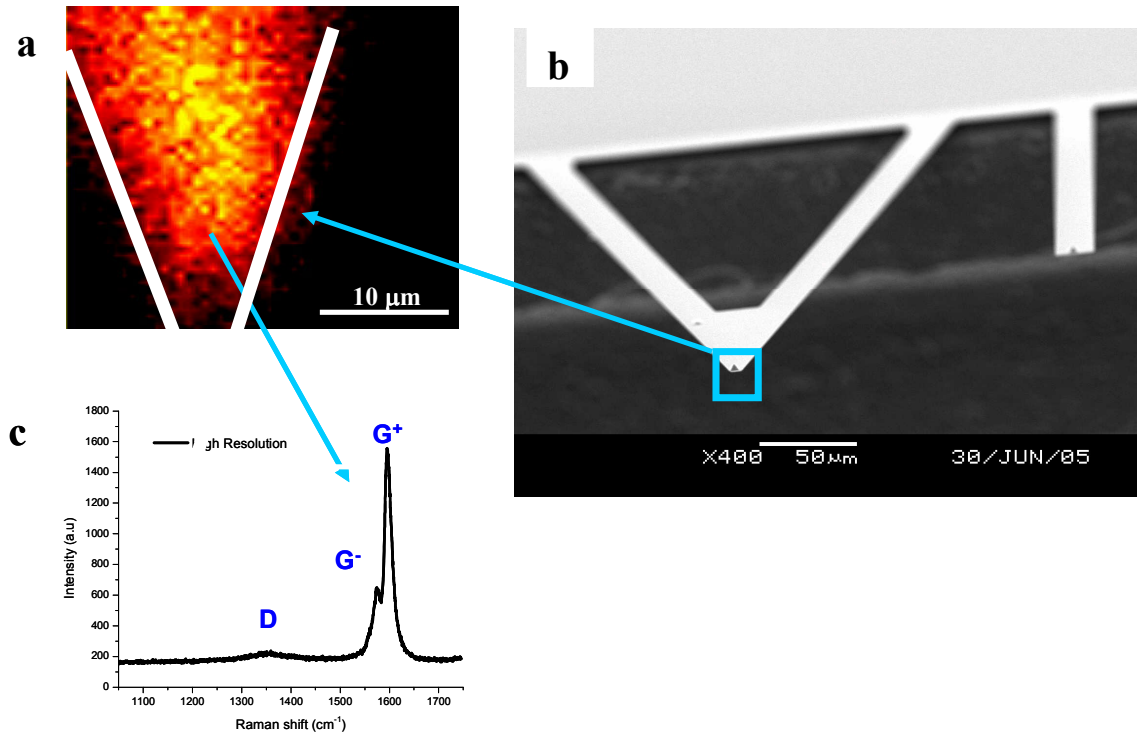

Figure 7-3. (a) Raman mapping of microcantilever end area as marked on an SEM image of a microcantilever (b);(c) Raman spectrum of carbon nanotubes embedded onto the microcantilever.

In fact, the silicon nitride-gold microcantilever bends downward by about 100 nm due to mismatch of thermal expansion coefficient of gold (14 x$10^{-6}K^{-1}$) and silicon nitride (0.8 x10^{-6} K^{-1}) (Fig 7-4a-d). The deflection of the microcantilever versus temperature is linear, reversible, and can be repeated hundreds of cycles with identical results. The thermal sensitivity calculated from the linear fit of the data was in the range 65-105 nm/K for various microcantilevers depending upon specific characteristics of individual microcantilevers. These values are within the typical range reported for similar gold-coated microcantilevers (Table 7-1).[23, 35] Considering this microcantilever-specific variations within the same batch are fairly large (± 30%), we conducted thermal sensitivity

measurements for each individual microcantilever before modification and repeated them for the same microcantilever after modification. This way, we can be sure that the accuracy of the individual measurement within ± 5% is much better that the changes caused by the chemical modification (from 12% to 450%).

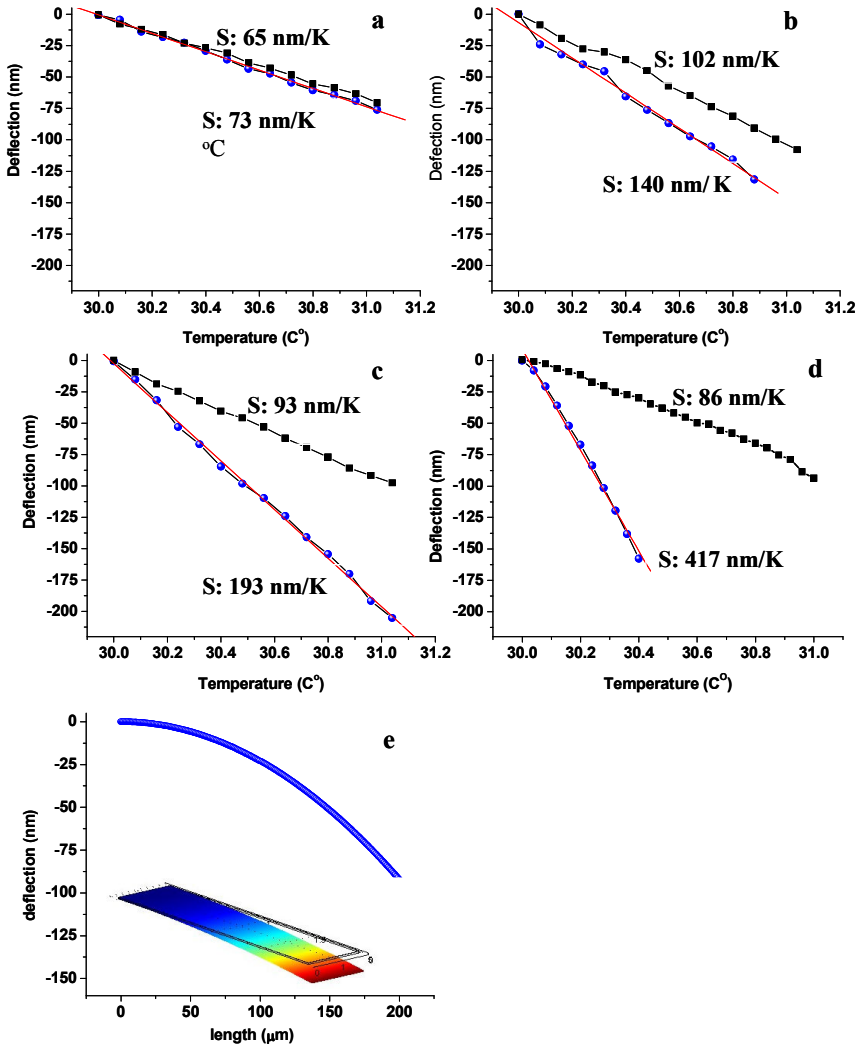

Figure 7-4. Temperature deflection for different microcantilevers, squares-unmodified gold-ceramic microntilevers, circles-modified microcantilevers with topmost layers: (a) PAN/Ag (b) PS/Ag/PAN (c) PAN/SWNT and (d) SWNT/PS/Ag/PAN (the error bars are smaller than symbol sizes, solid lines shows linear fits). (e) the simulated profile of the silicon nitride-gold cantilever for 1°C temperature increase and FEA image of the bent microcantilever.

As can be concluded fro the data obtained, the PAN-Ag topmost layer as the topmost layer (microcantilever **A**) changed thermal bending behavior very insignificantly (Fig. 4a). Much larger effect was observed for microcantilever **B** with PAN-Ag embedded in a grafted PS layer (Figs.7-4b, Table 7-1). However, the largest increase in the thermal sensitivity was achieved for the microcantilevers **C** and **D** with the topmost coating containing carbon nanotubes (Figs.7-4c, d, Table 1). Two-fold increase was observed after adding carbon nanotubes to the PAN matrix and even higher, *four-fold increase* was observed for the microcantilevers with a polymer nanocomposite layer containing both carbon nanotubes and silver nanoparticles embedded into PS layer (Table 7-1). All bending cycles were reproducible and similar bending behavior was obtained for larger temperature intervals (not shown). The thermal sensitivity for the microcantilever **D** reached 400 nm/K, which is a very high value for bimaterial microcantilever sensors. This suggest that in fact the nanocomposite layers of PAN/Ag/SWNT with high elastic modulus (estimated to be 50 GPa for the carbon nanotubes with random in-plane orientation) are firmly grafted to the metal surfaces in order to transfer thermally induced stresses and enhance bending ability despite slightly reduced thermal expansion coefficient due to negative thermal expansion of carbon nanotubes in axial direction.

The thermal bending scenarios for various polymer composite nanolayers was modeled with finite element analysis (FEA) simulation accounting for the thermally-induced stresses caused by mismatch in thermal expansion of different layers and full stress transfer across the interfaces (see a representative example in Fig. 7-4e). For silicon nitride and gold layers we used standard literature values for the thermal expansion coefficients and elastic moduli and for the polymer composite layer we evaluated the corresponding composite values from chemical composition (volume fractions of polymer, carbon nanotubes, and silver nanoparticles) assuming isostrain conditions.[36] The thermal sensitivity for different microcantilevers obtained with FEA showed good agreement with experimental observations for microcantilevers **B-D** as well as for un-modified microcantilevers **E** and **F** (difference within 20%) (Table 7-1). Only

in the case of the microcantilever **A** with PAN-Ag layer we observed much lower experimental value which can be related to poor adhesion between gold and PAN matrix.

Table 7-1. Characteristics of microcantilevers studied.

Cantilever	Topmost layer composition	Cantilever shape	Cantilever dimensions (L/W/T) μm	Spring constant (N/m)	Resonant frequency (kHz)	Sensitivity before modification (nm/K)	Sensitivity after modification (nm/K)	Theoretical sensitivity after modification (nm/K)
A	PAN/Ag	rectangular	200/20/0.6	0.031	14.1	65	73	130
B	PS/Ag/PAN	rectangular	200/20/0.6	0.028	13.3	102	140	170
C	PAN/SWNT	rectangular	200/20/0.6	0.027	15.6	93	193	220
D	SWNT/PS/Ag/PAN	V- shaped	320/22/0.6	0.016	6.5	86	417	450
E	Gold/Si_3Ni_4 (Unmodified)	rectangular	200/20/0.6	0.027	13.0-14.8	67-107	N/A	NA
F	Gold/Si_3Ni_4 (Unmodified)	V-shaped	320/22/0.6	0.017	6.1-7.3	73-103	N/A	NA

Experimental

A. Modification and characterization of microcantilevers

We used commercially available bimaterial Si_3N_4-Au cantilevers (one rectangular and five V-shaped) with a 60 nm gold layer sputtered on a 600 nm thick silicon nitride beam (Veeco, CA). PAN with carboxylic terminal groups was synthesized according established procedure, reported by Matyjaszewski et al.[37] , but using S-1-dodecyl-S'-(α,α'-dimethyl-α''-acetic acid) trithiocarbonate [38] as the RAFT agent. The M_n measurements were performed with a Varian 300MHz at 25 °C using dimethylsulfoxide-*d* (DMSO-d_6) as the solvent and tetramethylsilane (TMS) as an internal reference. The experimental molecular weight of PAN, M_n(NMR)=3 500, was calculated by comparing the area of peak corresponding to polymer backbone -CH_2 protons with those corresponding to -CH_3 protons from dodecyl of RAFT group , similar to procedure describe in literature.[39] Cystamine and α,ω-dicarboxy terminated PS (93.8K) were used as received from Aldrich and Polymer Source Inc.

The polymer composite nanolayer was immobilized via a functionalized SAM (cystamine on Au surface).[40,41] Single-walled carbon nanotubes (Carbolex, Texas) produced by the arc discharge method with COOH groups achieved by oxidation in nitric acid. Casting was conducted by drop drying of nanotube solution on cystamine-functionalized Au surface of microcantilever for about 24 hrs. The solution of 2% (w/w) of α,ω-dicarboxy terminated PS, in toluene were used for "grafting to" modification of the cantilever surface from melt.[27,42] The coated microcantilever were annealed at grafting temperatures ranging from 120˚C to 130˚C for 8 hours to enable the end groups to graft to the microcantilever. The un-grafted polymer was removed by multiple washings with toluene. Amine terminated silver nanoparticles (diameter of 10-20 nm, Nanohorizons) were cast onto the modified microcantilever over night before the last polymer layer build up. The last polymer layer of PAN in N,N-dimethylformamide were grafted from melt onto coated microcantilever by using spin coating followed by gentle thermal backing and drying under similar conditions. The overall layer microstructure is described as (A) PAN/Ag (volume fraction 70:30) (B) PS/Ag/PAN (43:14:43) (C) PAN/SWCN (90:10) and (D) SWNT/PS/Ag/PAN (5:40:15:40) (Table 1). AFM imaging in tapping mode was conducted on Dimension 2000 microscope according to usual procedure.[43,44] Raman measurements have been completed on custom-built confocal Raman spectrometer described earlier.[33]

B. Sensitivity measurements and thermal tune

The thermal sensitivity of microcantilevers was measured by utilizing the AFM optical detection system with angstrom resolution (Dimension 3000). The microcantilevers with spring constant 0.016-0.031 N/m was brought into within 1 □m of the surface of the thermal stage (a Peltier heater, 1x1 cm, ±0.001^{o}C). An acoustic/isolation hood was placed over the entire set-up to block out outside fluctuations. A laser beam was focused on the end of the microcantilever and reflected onto the AFM photodiode detector. The deflection of microcantilever was obtained with precision of 0.3 nm (as limited by the amplitude of thermal vibrations) after the sensitivity of the photodiode detector was independently calibrated. At each temperature

step (usually, 0.04-0.05C^{o}), the microcantilevers were kept for about a minute to reach an equilibrium.

The cantilever spring constants were measured using a Multimode AFM equipped with a Picoforce module, which used the well-known thermal tuning and resonant frequency measurements.[45,46,47] Before each measurement the tip was allowed to equilibrate before the photodetector was carefully calibrated. Then, after taking precautions to minimize environmental noise, the photodetector signal was sampled at frequencies from 0-35 kHz. The signal was filtered with a lock-in amplifier to optimize the signal to noise ratio. Then a Lorentzian fit was used to analyze the power vs. frequency spectra and to obtain the spring constant value and the quality factor.

C. Finite Element Analysis

Theoretical values for the deflections of the cantilever have been estimated with FEA using Structural Mechanics module of a commercial package COMSOL Multiphysics 3.2.[48] A typical FEA involves the reduction of the Energy Functional (***E***) of individual elements of the model. The minimization is attained by setting the derivative of ***E*** with respect to the displacement of the mesh element to zero. Principle of Virtual work has been opted as the implementation method for minimizing the ***E***. The model used a non-linear mode to account for the probable pinch-off effects in the deformation. The structure was meshed into ~40,000 elements. The ultra thin polymer layers and the gold layer have been mesh more finely compared to the thick Si_3N_4 beam so that the number of elements in each layer closely matched. The finer structure (increasing the element number twofold) caused less than 1% change in the deflection. Critical areas of the structure like the interfacial boundary between different layers and the edges were meshed finely to ensure small convergence parameter. The model accounts the material properties including Poisson's ratio, elastic modulus, thermal expansion coefficient, and density.

Conclusion

In summary, we have presented a novel *trilayered (ceramic-metal-polymer) approach* for designing thermally sensitive microcantilevers with the topmost *polymer nanocomposite layers* chemically grafted to the gold layer. The polymer layers were reinforced with carbon nanotubes and metal nanoparticles. Such a combination of materials within the strong polymer composite topmost layer provides for high thermal stresses that results in significant (*up to fourfold*) increase in the thermal sensitivity as compared with conventional ceramic-metal bilayered microcantilevers. These trilayered polymer-metal-ceramic microcantilevers with dramatically enhanced thermal sensitivity can serve as basis for the next generation of un-cooled IR sensor arrays with the thermal and spatial resolution manifold higher than those currently available.

References

1 Raiteri, M. Grattarola, H. J. Butt, P. Skladal, *Sens. Actuators, B* **2001**, *79,* 115.

2 N. V. Lavrik, M. J. Sepaniak, P. G. Datskos, *Rev. Sci. Instrum.* **2004**, *75*, 2229.

3 C. Ziegler, *Anal. Bioanal. Chem.* **2004**, *379*, 946.

4 J. R. Barner, R. J. Stephenson, M. E. Welland, C. Geberr, J. K. Gimzewski, *Nature* **1994,** *372*, 79.

5 T. Thundat, R. J. Warmack, G. Y. Chen, D. P. Allison, *Appl. Phys. Lett.* **1994**, *64*, 2894.

6 M. Sepanicak, P. Datskos, N. Lavrik, C. Tipple, *Anal. Chem.* **2002**, *74*, 568.

7 P. G. Datskos, P. I. Oden, T. Thuandat, E. A. Watchter, R. J. Warmack, S. R. Hunter, *Appl. Phys. Lett*. **1996,** *69*, 2986.

8 M. Calleja, J. Tamayo, A. Johansson, P. Rasmussen, L. Lechuga, A. Boisen, *Sens. Lett.* **2003**, *1*, 1.

9 L. A. Pinnaduwage, V. Boiadjiev, J. E. Hawk, T. Thundat, *Appl. Phys. Lett.* **2003**, *83*, 1471.

10 X. Yan, Y. Lvov, H. Ji, A. Singh, T. Thundat, *Org. Biomol. Chem*. **2003**, *1*, 460.

11 X. Yan, X. K. Xu, H. Ji, *Anal. Chem.* **2005**, *77*, 6197.

12 K. Liu, H. F. Ji, *Anal. Sci.* **2004**, *20*, 9.

13 Y. F. Zhang, H. Ji, D. Snow, R. Sterling, G. M. Brown, *Instrum.Sci. Technol*. **2004**, *32*, 361.

14 G. G. Bambu, G. Kircher, M. Wolkenhauer, R. Berger, J. S. Gutmann, *Macromol. Chem. Phys.* **2004**, *205*, 1713.

15 T. Perazzo, M. Mao, O. Kwon, A. Majumdar, J. B. Varesi, P. Norton, *Appl. Phys. Lett.* **1999**, *74*, 3567.

16 C. Jongeun, J. Yamaguchi, S. Morales, R. Horowitz, Y. Zhao, A. Majumdar, *Sens. Actuators, A*. **2003**, *104*, 132.

17 L. R. Senesac, J. L. Corbeil, S. Rajic, N. V. Lavrik, P. G. Datskos, *Ultramicroscopy* **2003**, *97*, 451.

18 Y. Zhao, M. Mao, R. Horowitz, A. Majumdar, J. Varesi, P. Norton, J. Kitching, *J. Microelectromech. Syst.* **2002**, *11*, 136.

19 C. Escriba, E. Campo, D. Estève, J. Y. Fourniols, *Sens. Actuators, A* **2005**, *120*, 267.

20 P. G. Datskos, M. J. Sepaniak, C. A. Tipple, N. Lavrik, *Sens. Actuators, B* **2001**, *76*, 393.

21 P. G. Datskos, N. Lavrik, S. Rajic, *Rev. Sci. Instrum*. **2004**, *75*, 1134.

22 E. A. Wachter, T. Thundat, P. G. Datskos, P. I. Oden, S. L. Sharp, R. J. Warmack, *Rev. Sci. Instrum*. **1996**, *67,* 3434.

23 J. L. Corbeil, N. V. Lavrik, S. Rajic, *Appl. Phys. Lett.* **2002**, *81*, 1306.

24 J. R. Barnes, R. J. Stephenson, C. N. Woodburn, S. J. O'Shea, M. E. Welland, T. Rayment, J. K. Gimzewski, Ch. Gerber. *Rev. Sci. Instrum.* **1994**, *65*, 3793.

25 J. K. Gimzewski, C. Gerber, E. Meyer, R. R. Schlitter, *Chem. Phys. Lett.* **1994,** *217*, 589.

26 .V. Tsukruk, *Prog. Polym. Sci.* **1997**, *22*, 247.

27 V. Tsukruk, A. Sidorenko, H. Yang, *Polymer* **2002**, *43,* 1695.

28 I. Luzinov, S. Minko, V. V. Tsukruk, *Prog. Polym. Sci.* **2004**, *29,* 635.

29 D. Julthongpiput, M. LeMieux, V. V. Tsukruk, *Polymer* **2003**, *44*, 4557.

30 V. V. Tsukruk, I. Luzinov, D. Julthongpiput, *Langmui* **1999**, *15*, 3029.

31 I. Luzinov, D. Julthongpiput, A. Liebmann-Vinson, T. Cregger, M. D. Foster, V. V. Tsukruk, *Langmuir* **2000**, *16*, 504.

32 T. V. Sreekumar, T. Liu, B. G. Min, H. Guo, S. Kumar, R. H. Hauge, R. E. Smalley, *Adv. Mater.* **2004**, *16*, 58.

33 H. Ko, Y. Pikus, C. Jiang, A. Jauss, O. Hollricher, V. V. Tsukruk, *Appl. Phys. Lett.* **2004**, *85*, 2598.

34. C. Jiang, H. Ko, V. V. Tsukruk, *Adv. Mater.* **2005**, *17*, 2127.

35 B. Li, *Sens. Actuators, A* **2004**, *112*, 351.

36 L. H. Sperling, *Polymeric multicomponent materials*, WILEY-INTERSCIENCE, New York **1998**.

37 C. Tang, T. Kowalewski, K. Matyjaszewski, *Macromolecules* **2003**, *36,* 8587.

38 J. T. Lai, D. Filla, R. Shea, *Macromolecules* **2002**, *35*, 6754.

39 A. Quanfu, J. Qian, L. Yu, Y. Luo, X. Liu, *J. Polym.Sci., Part A: Polym. Chem*. **2005**, *43*, 1973.

40 A. Ulman, *Chem. Rev.* **1996**, *96*, 1533.

41 V. V. Tsukruk, V. N. Bliznyuk, *Langmuir* **1998**, *14*, 446.

42I. Luzinov, D. Julthongpiput, H. Malz, J. Pionteck, V. V. Tsukruk, *Macromolecules* **2000**, *33*, 1043.

43 V. V. Tsukruk, D. H. Reneker *Polymer*, **1995**, *36*, 1791.

44 V. V. Tsukruk, *Rubber Chem. Techn.* **1997**, *70*, 430.

45 J. L. Hutter, J. Bechhoefer, *Rev. Sci. Instrum*. **1993**, *64*, 1868.

46 J. L. Hazel, V. V. Tsukruk, *Thin Solid Films* **1999**, *339,* 249.

47 J. Hazel, V. V. Tsukruk, *J. Tribology* **1998**, *120,* 814.

48 *Structural Mechanics Module Model User's Guide for Femlab3*, COMSOL AB,

CHAPTER 8
UV PHOTON CONDUCTIVITY OF ZnO NANOBELT BY POLYACRYLONITRILE FUNCTIONALIZATION

Jr H. He,*[,†,‡] Yen H. Lin,[†] Michael E. McConney,[†] Vladimir V. Tsukruk,[†] Gang Bao,[§] Zhong L. Wang*[,†]

A paper submitted to Advanced functional materials

[†]School of Materials Science and Engineering, Georgia Institute of Technology, Atlanta, Georgia 30332-0245 USA, [‡]Graduate Institute of Electro-Optical Engineering and Department of Electrical Engineering, National Taiwan University, Taipei, 106 Taiwan, [§]Department of Biomedical Engineering, Georgia Institute of Technology and Emory University, Atlanta, GA 30332-0245 USA

Abstract

UV photon detector fabricated using a single ZnO nanobelt (NB) has shown a photon response enhancement up to 750 times higher than that of a bare ZnO NB after coating with ~ 20 nm plasma polymerized acrylonitrile (PP-AN) nanoscale film. The mechanism for this colossal photon conductivity is suggested as a consequence of the efficient exciton dissociation under UV illumination due to enhanced electron transfer from valence band of ZnO NB to the PP-AN and then back to the conduction band of ZnO. This process has demonstrated an easy and effective method for improving the performance of the NW/NB-based devices, possibly leading to supersensitive UV detector for applications in imaging, photonsensing, and intrachip optical interconnects.

Introduction

Integrating nanophotonics with nanoelectronics is essential for developing the technologies for the next generation communication, computing and biomedical imaging. Low-dimensional nanostructures, such as nanodots [1] nanotubes, [2] and nanowires

♦ Assistant researcher, setup experiment, assisted with selecting materials, analysis, AFM measurements.

(NWs),[3,4,5,6] have been extensively studied for high sensitive optical detectoion, among which, ZnO is a typical example.

ZnO exhibits the most diverse and abundant configurations of nanostructures known so far, such as hierarchical nanostructures, [7] NWs,[6] nanobelts (NBs), [8] nanosprings,[9] nanorings,[10] nanobows,[11] and nanohelices.[12] Due to semiconducting and piezoelectric properties of ZnO, numerous studies have demonstrated potential applications in electronics and optoelectronics based on ZnO nanostructures, such as optically pumped nanolaser,[6] nanogenerator,[13] acoustic resonator,[14] piezoelectric gated diode,[15] field-emitter,[16] photodiode,[17] and photoconductor.[18,19,20]

Since the large surface-to-volume ratio of 1D ZnO nanostructures and the presence of deep level surface trap states in NWs/NBs, ZnO exhibits long lifetime photocarriers,[18,19,20, 21 , 22] and it usually exhibits lower photon sensitivity than photodiodes.[23,24] To date, despite a great deal of research on the photon sensing using nanowires, only a few of them reporting the improvement of photoresponse of NWs/NBs-based photoconductor.[25]

In this work, we present a bilayer polymer/ZnO photoconductor based on ZnO NBs and plasma polymerized acrylonitrile (PP-AN) nanoscale surface coating. By taking advantage of rectangular cross section of NBs, uniform bilayered PP-AN/ZnO NBs were fabricated by exploiting plasma enhanced chemical vapor deposition (PECVD). We demonstrated that under identical UV illumination conditions, the photoncurrent of ZnO NBs was increased by a factor of 750 after coating with PP-AN. The suggested mechanism includes a consequence of the efficient exciton dissociation under UV illumination due to enhanced electron transfer from valence band of ZnO NB to the photon-excited PP-AN rich on double and triple carbon-nitrogen bonds and then back to the conduction band of ZnO. The present study on the PP-AN-functionalized NBs presents a simple and cost-effective method for improving the performance of oxide NW/NB-based devices, possibly leading to a new generation of potential photon detector

for applications such as imaging, photosensing, and intrachip optical interconnects.

Experimental

In catalytically activated vapor phase transport and condensation deposition process, a 2-nm-thick Au thin film was deposited onto (11-20) Al_2O_3 substrate surface at room temperature using an electron beam evaporation system (~5×10^{-6} Torr), and Au serves as the catalyst for the growth. The experimental apparatus includes a horizontal tube furnace, a rotary pump system, and a gas supply system. A mixture of commercial ZnO and graphite powders in a ratio of Zn:C = 4:1 was placed in an alumina boat, which was heated to a peak temperature of 1100 ^{o}C. The Al_2O_3 substrate was placed at a temperature zone of ~ 700 ^{o}C for collecting ZnO nanostructures. After the tube had been evacuated to a pressure of 1×10^{-3} Torr, the mixed sources at high-temperature zone was heated to 1100 ^{o}C at a rate of 5 ^{o}C/min and held at 1100 ^{o}C for 60 min with a carrier gas of Ar+O_2 flowing through the tube. Morphological studies of grown ZnO nanostructures have been performed with a LEO 1530 field emission scanning electron microscopy (SEM). A representative SEM image of the grown ZnO NBs is shown in Figure 8-1a. After the growth process, the substrate-bound NBs were mechanically scrapped and sonicated in ethanol and deposited on carbon-coated copper grids for transmission electron microscopy (TEM) characterization. The inset in Figure 8-1a is a TEM image, which indicates that ZnO NBs is single-crystalline and free of dislocations.

Results and Discussion

The synthesized ZnO nanobelts are transferred from the Al_2O_3 substrate to prepatterned Ti/Au electrodes by touching the NB sample with the electrodes. A single ZnO NB device lying across two electrodes could be achieved easily using this method. To reduce the contact resistance, focused ion beam (FIB) microscopy is employed to deposit conducting mixture of Pt on the contacts between ZnO and Au/Ti electrodes. The prepatterned Au/Ti electrodes for contacting probes of current-voltage (I-V) measurements were fabricated on 100 nm Si_3N_4/Si wafer through a typical process in the literature.[26] The electrode pattern was designed to have a few parallel electrodes

separated by 5-20 μm. After the ZnO NB device fabrication, the PP-AN was deposited as a nanoscale surface layer by using PECVD technology with argon (50-200 cm^3/min, 99.999%) as the carrier gas within a custom built chamber according to the procedure published elsewhere.[27] The oxygen plasma treatment was carried out for eliminating the surface contamination of ZnO NB device before depositing PP-AN using PECVD. Figure 8-1b is a representative SEM image of a single ZnO NB device. Figure 8-1c shows topographic atom force microscopy (AFM, Dimension 3000, Digital Instruments) image of highly cross-linked PECVD PP-AN surface. The microroughness of the PP-AN was less than 0.7 nm (within 10μm x 10μm area), indicating a smooth and uniform surface morphology with a fine, granular nanodomain texture, which is a typical surface morphology of plasma polymerized polymers with high crosslinking density.[28] The average thickness of the PP-AN coating 27 nm was obtained from AFM scratch test (Figure 8-1d and 1e) and confirmed with ellipsometry.

Figure 8-2a shows the resultant schematic structure of PP-AN/ZnO NB device. The electron transport of a single ZnO NB was then studied. Figure 8-2b indicates the I-V characteristic of a bare ZnO NB device and a PP-AN/ZnO NB device. The device shows an almost identical IV characteristic before and after depositing the PP-AN on ZnO NBs, and there is no change in the current transported through the NB, suggesting the coated PP-AN has a much lower conductivity than that of ZnO. In fact, PP-AN is known as an insulating polymer with ultra high electrical resistivity.[29] Therefore, the total conductance of the PP-AN/ZnO NB is the conductance of the ZnO NB alone.

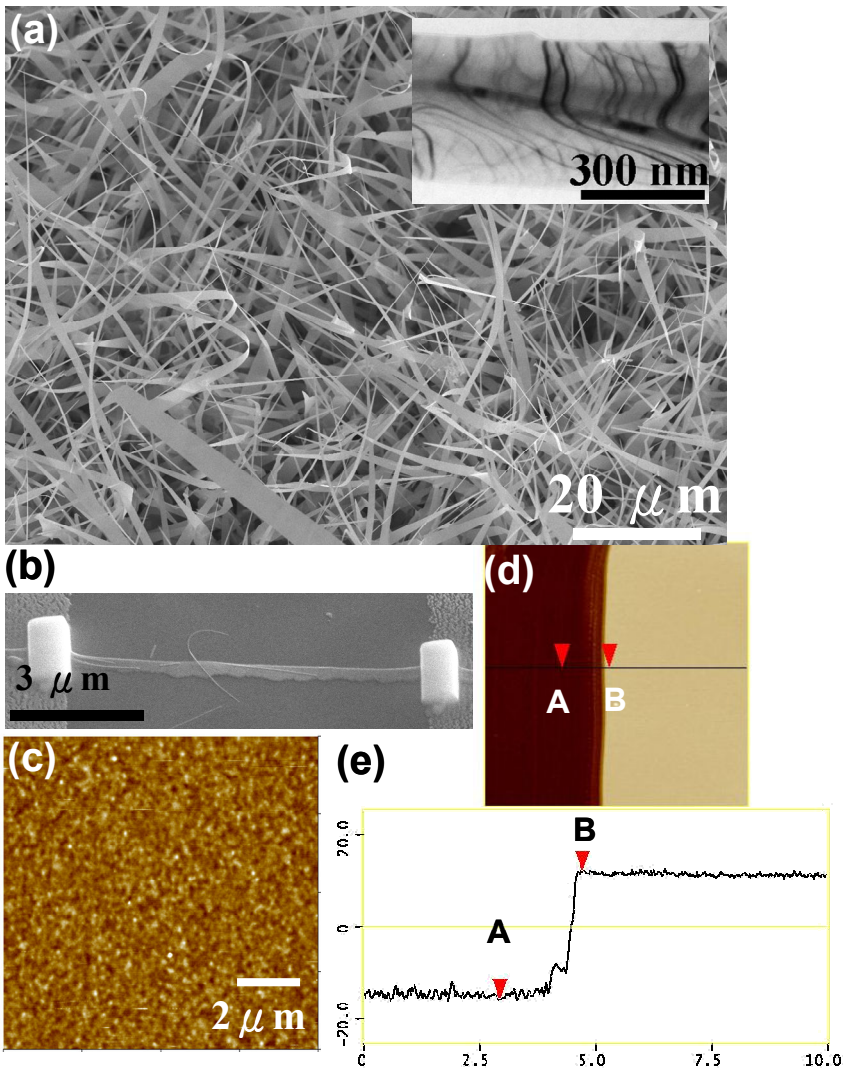

Figure 8-1. (a) A representative SEM image of ZnO nanobelts. The inset is an TEM image of a ZnO nanobelt. (b) The SEM image of a single ZnO NB device. (c) AFM topographic image of PP-AN (z scale is 10 nm, roughness is 0.7 nm). (d) AFM image for scratching test. The left-hand side film is PP-AN, (e) AFM line profile analysis of coated film thickness. Note: A and B in (d) are corresponding to A and B in (e).

To further explore the performance, we compared the photon current of the ZnO before and after PP-AN coating under identical UV illumination condition. The UV light source used in the experiment is a 100 Watt UV lamp with a wavelength of 365 nm (UVP, CA). All samples performed in the experiments of photon response were carried out

under identical measurement condition (e.g., position of UV light source, and the distance between light source and measured samples). Both the bare ZnO NB and the PP-AN/ZnO NB photoconductors showed an on/off state corresponding to the exposure of the UV light, as shown in Figure 8-3. Figure 8-3a is an intrinsic photon response of the bare ZnO NB under UV illumination. The current flowing through the bare ZnO NB increased with a ~12 % enhancement upon the exposure of the UV light. Here, the enhancement is the photocurrent-to-dark-current ratio. The photocurrent is deduced by subtracting the dark current from the current measured under UV. Surprisingly, for the PP-AN/ZnO NB, the photocurrent increased up to ~ 9000 %, as shown in Figure 8-3b, a colossal increase by a factor of 750 in comparison to that of bare ZnO NB (~12 %). Turning UV light off resulted in fast decrease of the photocurrent to the background level and overall cycling in photocurrent intensity was reproducible for many on-off cycles. Therefore, functionalizing the ZnO NBs by a thin layer of PP-AN is an effective and cost-effective approach for enhancing the optical response of NBs for UV detection.

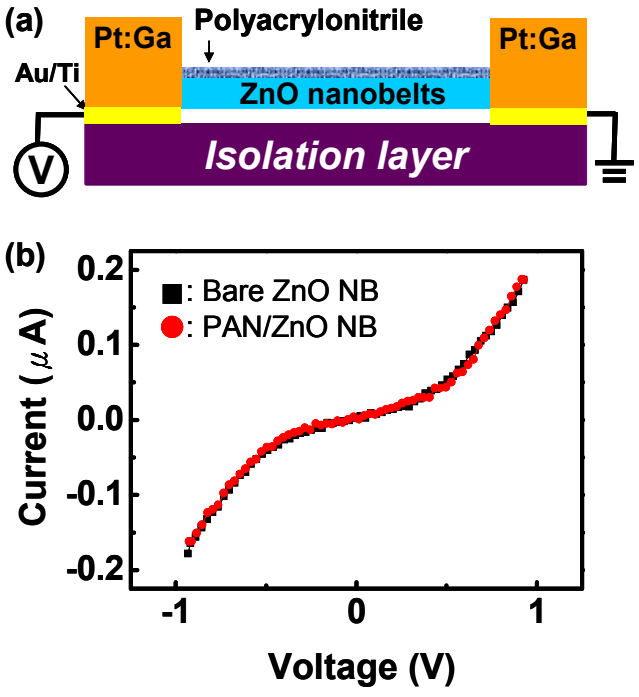

Figure 8-2. (a) The schematic diagram of PP-AN/ZnO NB device. (b) The I-V characteristic of a bare ZnO NB device and a PP-AN/ZnO NB device.

In contrast, by replacing UV with visible light, the photon response of PP-AN/ZnO shows no enhancement at all (Figure 8-3c). The absence of photon conduction upon visible light illumination indicates the absence of defect states,[18,19,20] such as oxygen vacancies in the PP-AN/ZnO NBs, indicating that there is no detectable level of defects created in the NB after PP-AN coating.

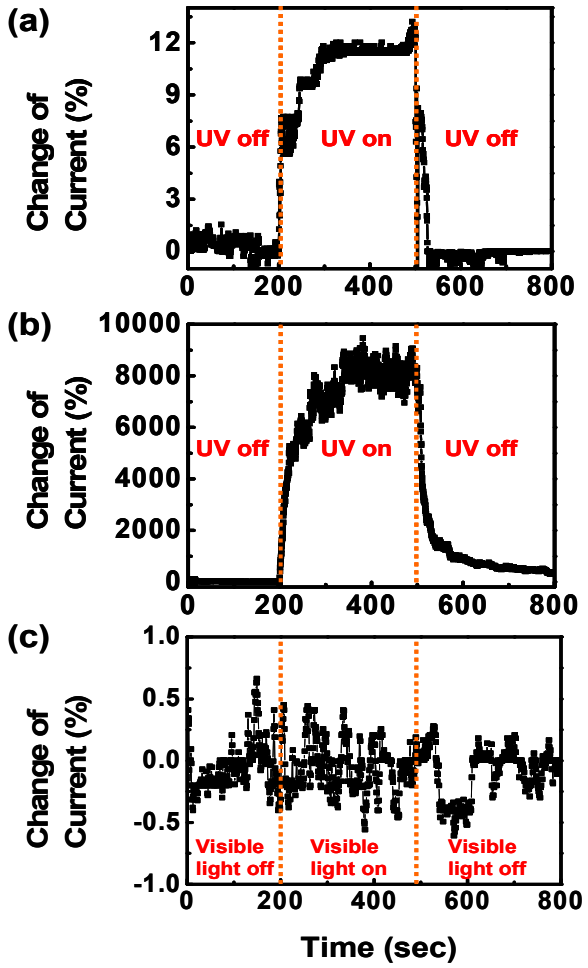

Figure 8-3. Photocurrent of (a) a bare ZnO NB device and (b) a PP-AN/ZnO NB device under UV light illumination, received under identical measurement conditions. (c) Photon current of PP-AN/ZnO NB device under visible-light illumination. Note: Vertical axis is the ratio of the photon-current to dark-current. The photon-current was derived by subtracting dark current from the observed total current

To clarify the mechanism of ultrahigh photon response of PP-AN/ZnO NB photon detectors, the electrical performance of the PP-AN film alone was examined by electrical and fluorescence (FL) measurements. First, PP-AN films were deposited between the two parallel electrodes separated by 5-20 μm. I-V measurements in the dark and under UV illumination were performed, as shown in the Figure 8-4. The inset in the Figure 8-4 is a schematic diagram of the measurement for PP-AN films. PP-AN shows the insulating electrical property and absence of photoconduction under UV illumination, which indicates no distinctive change of conductivity under UV illumination. The emission spectrum of PP-AN is shown in Figure 8-5a, which exhibited a broad peak at the wavelength of around 550 nm. The PL of PP-AN is associated with the π–π* electronic transition in C=N and C≡N groups in PP-AN [30,31] with presence of these groups in highly cross-linked material confirmed by FTIR and XPS studies as reported elsewhere.[32] In fact, the UV-vis spectroscopy confirmed the presence of strong absorption bands around 250 and 310 nm attributed to the *Π-Π** electronic transition of the nitrile group and the C≡N absorption.[31, 33, 34] These peaks with the appearance of a broad absorbance at higher wavelength reflect the formation of C=N *Π* electron conjugation system for the plasma polymers indicating a extended conjugated *Π* -system in highly cross-linked PP-AN.[33]

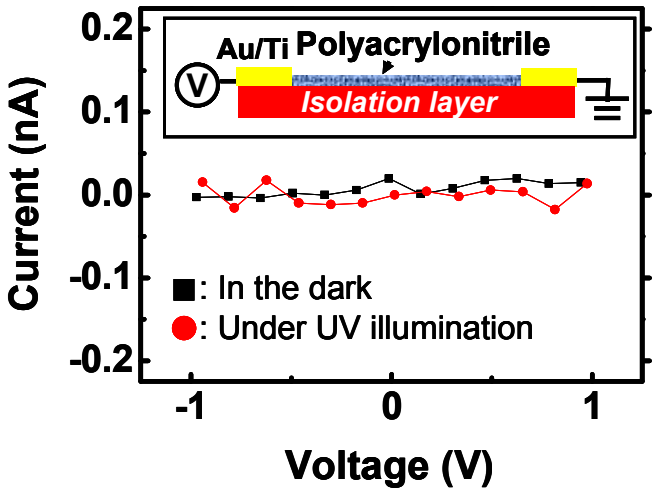

Figure 8-4. I-V measurements of PP-AN films in the dark and under UV illumination. The inset is a schematic diagram of the measurement.

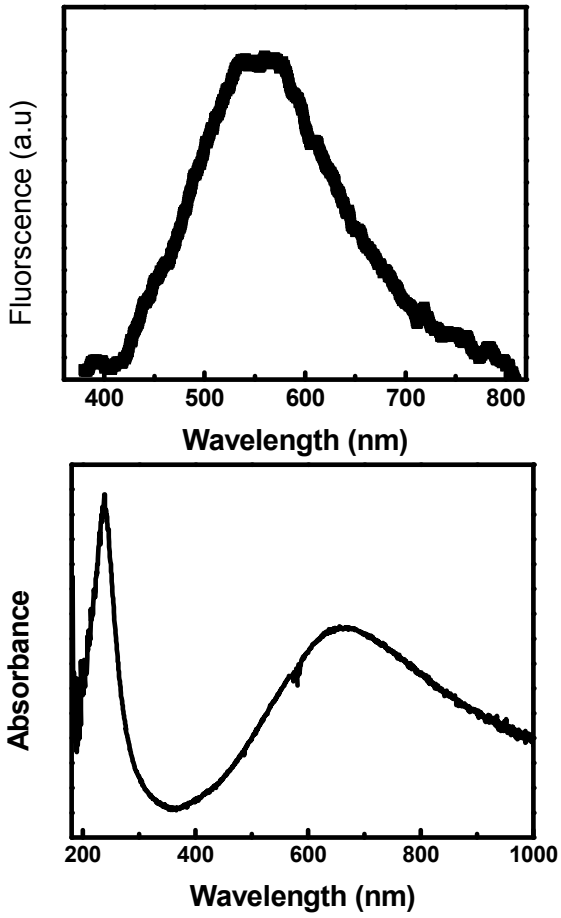

Figure 8-5. Fluorescence (top) and UV (bottom) spectra of a PP-AN coating

Generally, the molecular structures of plasma polymerized molecular are different from starting monomers, because the polymers are formed with highly decomposed molecules under ions and electron reactions with high energy.[35] Moreover, the shift of peak in the PL associated with the morphology transition could be explained in terms of the rearrangement of intermolecular structure in the polymer backbone as the size and dimensionality of PP-AN nanomaterials change.[28,29] The emission spectrum of PP-AN means that electrons in the PP-AN were excited to a higher energy state (excited state) under the exposure of UV light, which left an unoccupied orbital (ground state) at an energy level that falls within the band gap of ZnO. At the same time, the electrons inside

the ZnO NB were also excited under the exposure of the UV illumination. The ground state and excited state of PP-AN acted as a transition state for the electron in the valance band of ZnO to transit to the conduction band of ZnO. This hopping process of electrons from the valance band of ZnO to PP-AN and then back to conduction band of ZnO is suggested to be responsible for the much enhanced conductivity of the PP-AN/NB device.

Conclusion

In summary, we have explored the photon conduction of an inorganic–organic hybrid NB. A simple coating of PP-AN on the ZnO NB increased its photon conductivity by a factor of 750 in comparison to that of a bare ZnO NB. This effect is suggested as a consequence of the high efficiency of exciton dissociation under UV illumination due to efficient electron transfer from valence band of ZnO NB to the PP-AN and then back to the conduction band of ZnO. Emission spectrum of the PP-AN films shows good agreement with the exciton dissociation model that is electron excition from the ground state to the excited state. The present study on the PP-AN-functionalized NBs presents a simple and cost-effective approach for significant improving the performance of oxide NW/NB-based devices for photon detection, possibly leading to a motivation for studying the optoelectronic properties of inorganic–organic hybrid nanomaterials.

Acknowledgement

The support is provided by Emory-Georgia Tech CCNE (NIH), DARPA, AFOSR, AFRL, and NSC. The authors thank T. J. Bunning,' H. Jiang, and J. O. Enlow (AFRL) for technical assistance.

References

1 V. L. Colvin, M. C. Schlamp, A. P. Alivisatos, *Nature* **1994**, *370*, 354.

2 J. A. Misewich, R. Martel, P. Avouris, J. C. Tsang, S. Heinze, J. Tersoff, S*cience* **2003**, *300*, 783.

3 X. Duan, Y. Huang, R. Agarwal, C. M. Lieber *Nature* **2003**, *421*, 241.

[4] J. H. He, R. S. Yang, Y. L. Chueh, L. J. Chou, L. J. Chen, Z. L. Wang *Adv. Mater.* **2006**, *18*, 650.

[5] J. H. He, T. H. Wu, C. L. Hsin, K. M. Li, L. J. Chen, Y. L. Chueh, L. J. Chou, Z. L. Wang *Small* **2006**, *2*, 116.

[6] M. H. Huang, S. Mao, H. Feick, H. Q. Yan, Y. Y. Wu, H. Kind, E. Weber, R. Russo, P. D. Yang *Science* **2001**, *292*, 1897.

[7] J. Y. Lao, J. G. Wen, Z. F. Ren *Nano Lett.* **2002**, *2*, 1287.

[8] Z. W. Pan, Z. R. Dai, Z. L. Wang *Science* **2001**, *291*, 1947.

[9] X. Y. Kong, Z. L. Wang *Nano Lett.* **2003**, *3*, 1625.

[10] X. Y. Kong, Y. Ding, R. Yang, Z. L. Wang *Science* **2004**, *303*, 1348.

[11] W. L. Hughes, Z. L. Wang *J. Am. Chem. Soc.* **2004**, *126*, 6703.

[12] P. X. Gao, , Y. Ding W. J. Mai, W. L. Hughes, C. S. Lao, Z. L. Wang *Science* **2005**, *309*, 1700.

[13] Z. L. Wang, J. H. Song *Science* **2006**, *312*, 242.

[14] B. A. Buchine, W. L. Hughes, F. L. Degertekin, Z. L. Wang *Nano Lett.* **2006**, *6*, 1155.

[15] J. H. He, C. L. Hsin, J. Liu, L. J. Chen, Z. L Wang *Adv. Mater.* **2007**, *19*, 781.

[16] Y. B. Li, Y. Bando, D. Golberg, *Appl. Phys. Lett.* **2004**, *84*, 3603.

[17] J. H. He, S. T. Ho, T. B. Wu, L. J. Chen, Z. L. Wang *Chem. Phys. Lett.* **2007**, *435*, 119.

[18] K. Keem, H. Kim, G. T. Kim, J. S. Lee, B. Min, K. Cho, M. Y. Sung, S. Kim *Appl. Phys. Lett.* **2004**, *84*, 4376.

[19] Z.Y. Fan, , P. C. Chang, J. G. Lu, E. C. Walter, R. M. Penner, C. H. Lin, H. P Lee *Appl. Phys. Lett.* **2004**, *85*, 6128.

[20] C. Soci, A. Zhang, B. Xiang, S. A. Dayeh, D. P. R. Aplin, J. Park, X. Y. Bao, Y. H. Lo, D. L. Wang, *Nano Lett.* **2007**, *7,* 1003.

[21] H. Kind, H. Q. Yan, B. Messer, M. Law, P. D. Yang *Adv. Mater.* **2002**, *14*, 158.

[22] S. Mathur, S. Barth, H. Shen, J. C. Pyun, U. Werner *Small* **2005**, *1*, 713.

[23] O. Hayden, R. Agarwal, C. M Lieber,. *Nature Mater.* **2006**, *5*, 352.

[24] S. M. Sze *Physics of Semiconductor Devices*; John Wiley et Sons, **1981**.

[25] C. S. Lao, Y. Li, C. P. Wong, Z. L. Wang, *Nano Lett.* (ASAP paper).

[26] J. Liu, P. X. Gao, W. J. Mai, C. S. Lao, Z. L. Wang *Appl. Phys. Lett.* **2006**, *89*, 063125.

[27] Jiang, H.; Grant, J. T.; Eyink, K.; Tullis, S.; Enlow J.; Bunning, T. J. *Polymer* **2005**, *46*, 8178.

[28] LeMieux, M. C.; McConney, M. E.; Lin, Y.-H.; Singamaneni, S.; Jiang, H.; Bunning, T. J.; Tsukruk, V. V. *Nano Lett.,* **2006**, *6*, 730.

[29] S. R. C. Vivekchand, K. C. Kam, G. Gundiah, A. Govindaraj, A. K. Cheetham, C. N. R. Rao, *J. Mater. Chem.* **2005**, *15*, 4922.

[30] An, B. K.; Kwon, S. K.; Jung, S. D.; Park, S. Y. *J. Am. Chem. Soc.* **2002**, *124*, 14410.

[31] Jang, J.; Bae, J.; Park, E. *Adv. Funct. Mater.* **2006**, *16*, 1400.

[32] S. Singamaneni, M. C. LeMieux, H. Jiang, T. J. Bunning, V. V. Tsukruk *Chem. Mater.*; **2007;** *19*, 129.

[33] Pethkar, S.; Dharmadhikari, J. A.; Athawale, A. A.; Aiyer,R. C.; Vijayamohanan, K**.** *J. Phys. Chem. B* **2001,** *105,* 5110.

[34] Ge, J. J.; Hou, H.; Li, Q.; Graham, M. J.; Greiner, A.; Reneker, D. H.; Harris, F. W.; Cheng, S. Z. D. *J. Am. Chem. Soc*. **2004**; *126*, 15754.

[35] Kim, M. C.; Cho, S. H.; Han, J. G.; Hong, B. Y.; Kim, Y. J.; Yang, S. H.; Boo, J. H. *Surf. Coat. Technol.* **2003**, *169*, 595.

CHAPTER 9
ROBUST, FLUORESENT, AND NANOSCALE FREESTANING CONJUGATED FILMS

A paper published in Soft Matter, 2007, 3, 432-436

Yen-Hsi Lin,[ab] Chaoyang Jiang,[a] Jun Xu,[b] Zhiqun Lin[b],Vladimir V. Tsukruk[a]

a. School of Materials Science & Engineering, Georgia Institute of Technology, Atlanta, Georgia 30332, U.S.A

b. Department of Materials Science & Engineering, Iowa State University, Ames, Iowa 50011, U.S.A

Abstract

Conjugated polyelectrolytes composed of rod-like chains are exploited here for layer-by-layer (LbL) assembly of freestanding films with nanoscale (<20 nm) thickness. These LbL films are flexible, robust and demonstrated excellent mechanical properties combined with high and stable fluoresence response even under high stresses.

Introduction

Ultrathin polymeric films with well-defined nanoscale structures have great potential to be integrated in microdevices with fast response time and high sensitivity as a new generation of sensors and actuators.[1] The ultrathin planar freestanding layer-by-layer (LbL) films, with versatile multilayer architectures composed of alternating layers of magnetite nanoparticles, clay palletes, and polyelectrolytes, have showed extraordinary mechanical properties.[2] With novel spin-assisted LbL (SA-LbL) assembly, a series of robust free-standing nanoscale film from polyelectrolytes reinforced by nanofillers (gold nanoparticles, carbon nanotubes, or silver nanorods) have recently been fabricated and studied.[3] These exceptionally stable films demonstrated interesting micromechanical and

♦ Primary researcher; carried out most of experiments, writer of all drafts

optical properties and were suggested as promising candidates for prospective sensing elements for acoustic, thermal, magnetic, and pressure sensors.[4]

The free standing LbL films fabricated to date are truly self-supporting structures (preserving their shape and dimensions under their own weight and under significant mechanical loads) which survive under normal laboratory conditions (humid air, capillary forces, vibrations, temperature fluctuations) and possess truly long shelf life (years). However, to achieve this important robustness, they are either reinforced with high-strength nanoscale fillers (e.g., metal nanoparticles) or are made relatively thick (microns), which limit their applications as flexible nanoscale films. The successful fabrication of *purely polymeric and robust* free-standing nanoscale structures is still technically challenging because of poor mechanical stability of non-reinforced polymer chains within films with the thickness comparable with their dimensions.[5] A minimum thickness for robust and strong freely suspended LbL polymeric films achieved today is around 50 nm.[3]

On the other hand, conjugated polymers have several unique features such as strong inter-chain interaction, light weight, semiconducting properties, high strength, strong fluorescence, and low-voltage actuation, which make them attractive for electrooptical applications.[1,6] Controlling the solid state organization of such conjugated polymers within nanoscale films is critical for tuning their macroscopic optical and electrical properties and therefore should be intensively studied for the applications of light emitting diodes, photovoltaic cell, electrochromic switchers, and optical sensors. In fact, LbL films from various conjugated polymers have already been fabricated and their interesting electrochemical, photoluminescence, and non-linear optical properties have been explored.[7] These films offer the possibility for impact in the areas of photovoltaic cells,[8] light emitting diodes (LED),[9] thin-film transistors,[10] and bio-sensors[11] due to their intriguing optoelectronic properties.[12] The most commonly used water soluble conjugated polymer is poly-2,5-methoxy-propyloxy sulfonate phenylene vinylene (MPS-PPV).[13] However, all these films have been assembled on the supporting solid substrates

and the questions of their mechanical integrity and stability as well as fluorescent properties in the free standing state have been not even addressed.

In this communication, we report on the fabrication of freely suspended polymeric LbL films without any nanofillers with a truly nanoscale thickness (below 20 nm) which demonstrated very robust mechanical properties. For this fabrication, we selected a water soluble conjugated polymer MPS-PPV, which is essentially a rod-like chain with much stronger mechanical properties than usual flexible-chain polyelectrolyte exploited for previous LbL assembly of free-standing films. Moreover, the conjugated nature of the MPS-PPV chains brings intense fluorescent response, which is extremely stable even under large mechanical deformations. The morphology as well as mechanical and optical properties of these ultra-thin LbL films are investigated and discussed.

Experimental

The polymer films with different thicknesses were fabricated using spin-assisted LbL (SA-LbL) method and characterization techniques as described in detail in previous publications. [3,14] Briefly, silicon wafers for initial LbL film deposition of the {100} orientation with one side polished were cut to 10 × 20 mm pieces and were then cleaned in fresh piranha solution (1:3 (v/v) H_2O_2/H_2SO_4). A sacrificial cellulose acetate (CA) layer was spin coated on the freshly cleaned silicon substrate. A droplet (150 μL) of 0.2% (w/w) cationic PAH solution was spun coated on the sacrificial layer (3000 rpm) and followed by throughout rinsing with nanopure water (twice). After that, aqueous anionic MPS-PPV solution was spun coated and rinsed in a similar manner. This procedure was repeated until the needed number of polymer bilayers, *n*, was achieved. Acetone solution was used to dissolve the sacrificial CA layer in order to release the LbL films. The LbL films were transferred to Nanopure water where they could then be picked up with different substrates such as a highly polished copper plate with a single micromachined hole or a clean silicon wafer for further experiments.

Results and Discussion

SA-LbL films with different thicknesses have been prepared on a sacrificial support in accordance with the known procedure (see Experimental). These films could be transferred in large pieces to cover an array of holes with different diameters and showed relatively uniform optical appearance (Figure 9-1a,b). The surface of SA-LbL films was relatively uniform with developed grainy morphology and a microroughness (within 1 μm^2 surface area) below 5 nm which is a typical value for LbL films from conjugated polymers (Figure 9-1a). The thickness of LbL films increased linearly with the number of bilayers with an increment about 3.5 nm per bilayer, which is a common value for PPV-based LbL films. [8] This thickness corresponds to the transversal dimension of two rod-like chains packed side-to-side (2.6 nm) combined with the thickness of PAH (Poly allylamine hydrochloride) layer (about 1 nm) (Figure 9-1c). The average thickness of $(MPS\text{-}PPV/PAH)_5$, the thinnest film discussed here in great detail, was 18 ± 2 nm.

The major absorption maxima in UV-vis spectra at 295 nm and 425 nm correspond to the longitudinal π-π* transitions of the MPS-PPV backbones (Figure9-2a), as reported in the literatures. [15] The broad absorption band at 355 nm corresponds to the pendant groups (sulfur trioxide) [16] and transversal transitions of delocalized states of rigid backbones. [15] The steady linear increase in absorbance intensities at both 295 nm and 425 nm with a number of deposited layers (n = 5-30) indicates a progressive LbL assembly growth (Figure 9-2). [17]

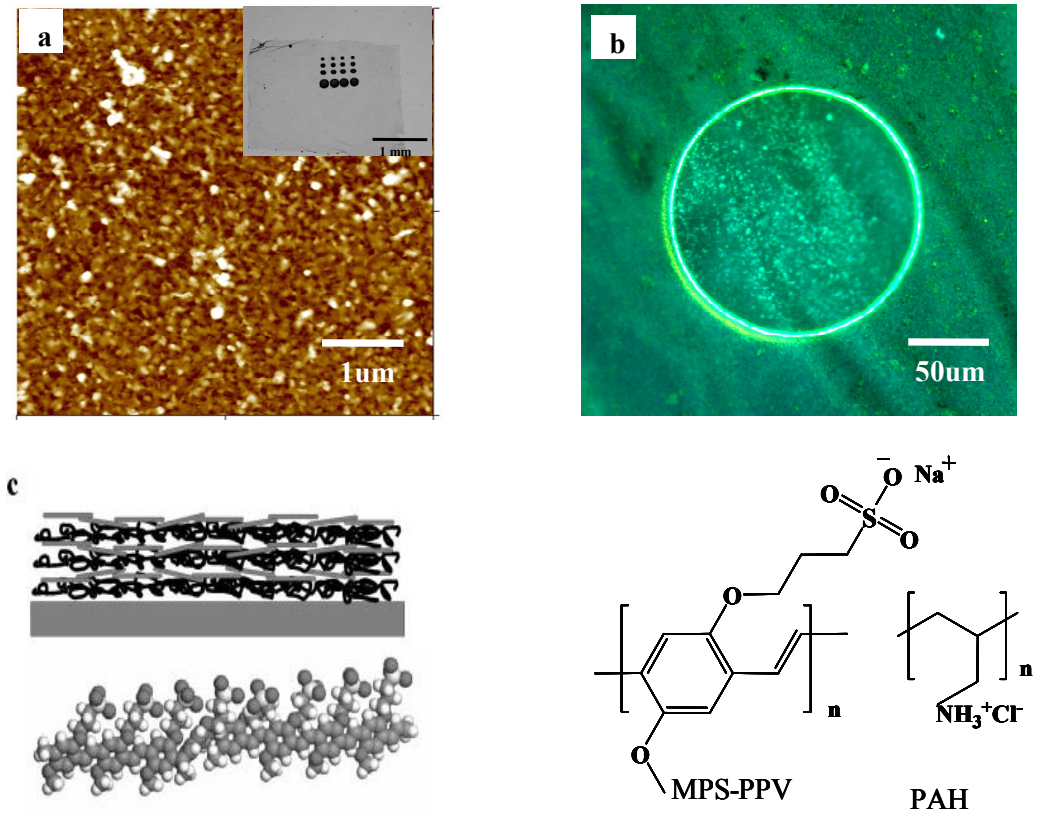

Figure 9-1. (a) AFM topographical image of (MPS-PPV/PAH)$_5$ film (z range is 80 nm) and an optical image of a whole free standing film on an array of holes (inset). (b) Fluorescence image of freely suspended film on a 150 um diameter hole. (c) The cartoon of multilayered structure and a molecular model of MPS-PPV chain; (d) Chemical structure of polymers exploited.

Figure9-2(b) shows the emission spectra of (MPS-PPV/PAH)$_5$ LbL film as well as the spin-cast MPS-PPV film and dilute solution normalized to the same peak intensity. The emission profiles are very similar for all states with an emission maximum at 530 nm (Figure 9-2b). The presence of a single poorly resolved broad (half-width about 120 nm) peak can be also associated with the fact that MPS-PPV cast film shows predominantly single-chain emission in solid state with significant overlap of the individual vibronic bands. [18] This is usually observed for LbL and LB films based on PPV-derivatives as well as corresponding spin-cast films and blends. [19]

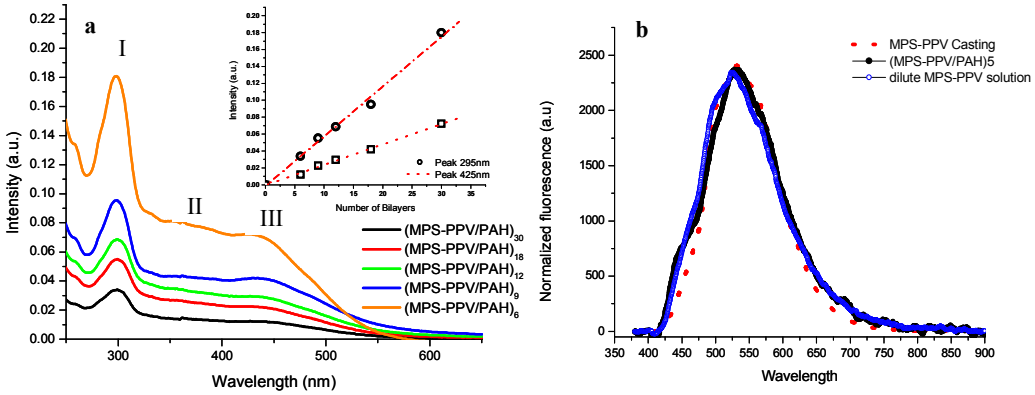

Figure 9-2. (a) UV/Vis spectra for LbL films with different numbers of bilayers, inset shows absorbance at 425 nm vs the number of deposited bilayers. (b) Fluorescent spectra (normalized) of the spin-cast MPS-PPV film, dilute MPS-PPV solution, and $(MPS\text{-}PPV/PAH)_5$ LbL film.

The emission peak of MPS-PPV is blue-shifted significantly as compared to bulk PPV films (at 583 nm for as spin-cast and at 610-630 nm for annealed films).[15,20] A significant blue shift of the emission band for PPV-based molecules embedded into multilayered LbL films is a common phenomenon.[21,22] This behavior is caused by coupling of the longitudinal packing of rod–like molecules combined with their loose lateral packing both caused by the confinement of rod-like MPS-PPV molecules between PAH layers (Figure 9-1c). In such a structure, the presence of PAH interlayers significantly disturbs transversal interchain interactions typical for crystalline packing which, in turn, should result in blue-shift of the corresponding emission band due to decoupling side-by-side interactions, in fact, observed here. On the other hand, this significant blue shift can be an indication of the formation of strong H-aggregates within the MPS-PPV layer with predominant parallel side-by-side packing of rod-like segments.[23]

The emission spectra collected in rest and deformed states have very similar shapes with an insignificant blue shift of the peak position close to the experimental

uncertainty (from 528 to 525 nm) (Figure 9-3a). Fitting of the emission band with five Lorentzian peaks (as suggested before for PAH-PPV composites [24]) with different contributing peaks attributed to longitudinal intrachain transitions (shorter wavelength) and transversal interchain transitions and side-by-side interactions was conducted to test the consistency of photoemission. [20,25,26] Essentially, the main contribution is from intermolecular interaction to the optical properties. However, there is no simple, clear correlation of the fluorescence with mechanical deformation. The application of pressure could potentially increase the mobility of the excitons to quenching. As the pressure increased distortion in disordered PPV polymer chain. This could increase of the degree of conjugation and facilitate the motion of excitons along the polymer chain. As we observed, the characteristics of all peaks but last one remain virtually unchanged (within experimental accuracy) indicating stable state of PPV backbones under these deformation conditions (strain reaching 0.8% and film deflection reaching 7 μm). Apparently, this result indicates highly stable local ordering and conformation of PPV chain under level of tensile elastic deformation tested here which results in very stable photoemission signature even under significant mechanical deformations. The explanation for this highly stable photoemission could result from the LbL structure. By using PAH layer as a spacer layer, we were able to construct assemblies which lead to a reduction of the interpenetration of each photoemission PPV layer.

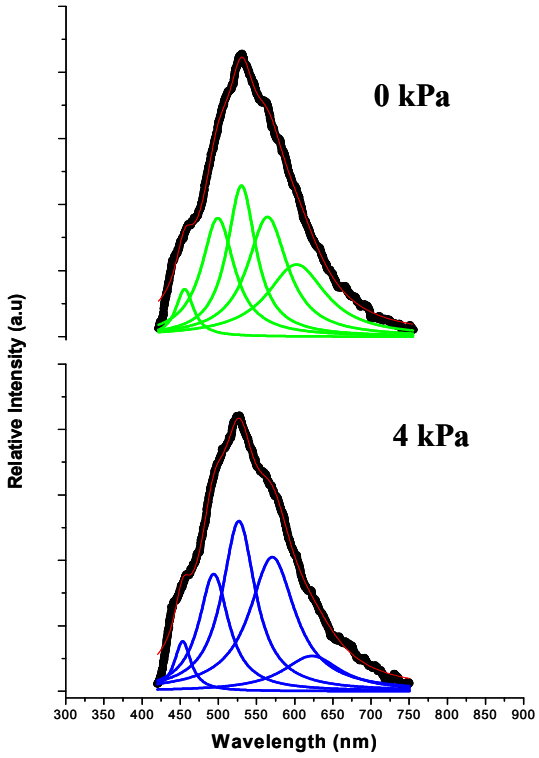

Figure 9-3. Fluorescence spectra of $(MPS\text{-}PPV/PAH)_5$ LbL film in the rest state and under elastic deformation (0.8%).

The micromechanical properties of these LbL films under tensile and compression stresses were studied using two independent experiments. For tensile properties, a bulging test was used and compressive properties were tested with buckling instability test (see Experimental). Figure 9-4(a) shows the deflection of the freely suspended $(MPS\text{-}PPV/PAH)_5$ film under an increasing hydrostatic pressure applied from one side. The LbL film response was nonlinear and experimental data are well fit with the theoretical prediction for the large elastic deformation of a circular plate clamped to a stiff edge. The pressure-deflection experimental data (before plastic deformation region) was fit with a proper equation following a cubic term, indicating a common phenomenon: internal stresses for polymer thin film as previous discussed in detail. The 18 nm thick $(MPS\text{-}PPV/PAH)_5$ films freely suspended across 150 μm opening showed extremely

robust but flexible behavior: multiple elastic deformations were observed for pressures reaching 4 kPa which corresponds to the tensile strain 0.8% at stress reaching 35 MPa, a high value for polymers. A full pressure versus deflection curve can be converted into a stress versus strain curve which can be use for estimate the film toughness. The toughness of the $(MPS\text{-}PPV/PAH)_5$ film estimated from film fracture was determined to be 118 kJ/m^3 which is very high for nanoscale polymeric films and indicates their exceptional long-term durability. The necking region from stress-strain curve apparent at pressure 2.5 kPa (close to deflection 7μm) causing carbon-carbon chains to become aligned and more ordered until neck boundary no longer propagates at pressure 9.8 KPa (close to deflection 20μm). Therefore the film deflection reached 20 μm for the highest pressure applied which is close to failure point in the permanent plastic deformation region. However, only deformations below 7 μm (in elastic deformation) were completely reversible with higher deflection leading to plastic deformation. The average elastic modulus obtained from the data analysis by using the theory of the elastic deformation of the freely suspended membranes was calculated to be 2.4 ± 0.3 GPa. [27]

On the other hand, in-plane compression of LbL film deposited on the PDMS substrate resulted in uniform buckling pattern with microscopic spacing (obtained from 2D FFT data), which can be used to the estimation of the elastic modulus (Figure 9-4b). [28,29] The elastic modulus of 2.6 ± 0.3 GPa calculated from the buckling spacing is close to that evaluated from budging experiments as expected for uniform elastic solids.

The Young's moduli of ultra-thin LbL films determined here is twofold higher than typical values obtained for conventional polymeric LbL films. For example, LbL films of PAH/PSS (poly sodium-4-styrene sulfonate) usually shows the modulus of 1-2 GPa [3]. By comparing the molecular structure of PSS and MPS-PPV, we can clearly realize that the presence of rigid rod-like conjugated backbones with stronger inter-chain interactions can enhance the mechanical properties of the multilayer films.

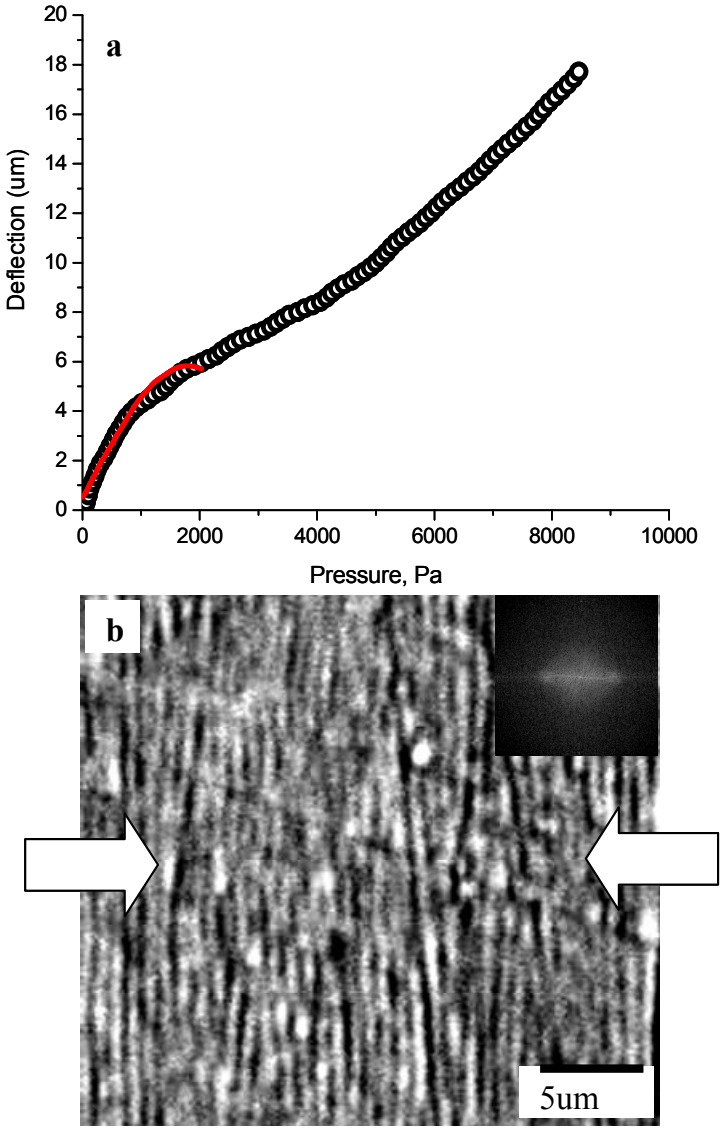

Figure 9-4. a) Pressure-induced deformation of the freely suspended (MPS-PPV/PAH)$_5$ LbL film. (b) Optical image of buckling pattern of the compressed LbL film (compression direction is shown by arrows).

Conclusion

In conclusion, we demonstrated successful fabrication of record thin (below 20 nm), robust, free-standing purely polymeric LbL films which incorporated

polyelectrolyte MPS-PPV molecules as an important reinforcing and electro-optically active component. These LbL films with nanoscale thickness can be significantly deformed and show elastic behavior for strain reaching 0.8% with the elastic modulus of 2.6 GPa. Moreover these robust LbL films in free-standing state possess strong photoemission in a green range which can be easily detected and stable under the elastic regimes applied here. This optical-quality freely standing conjugated film offers the possibility for prospective applications such as flexible, lightweight displays and ultrathin luminescent panels with strong and stable emission properties.

Acknowledgements

This work was supported by the AFOSR, FA9550-05-1-0209 and NSF-CTS-0506832 Grants, and the 3M Non-tenured Faculty Award (ZL). JX thanks the Institute for Physical Research and Technology of Iowa State University for a Catron graduate research fellowship. We also thank Emily Merrick for assistance with sample preparations.

References

[1] (a) E. W. H. Jager, E. Smela, O. Inganäs, *Science*, **2000**, *290,* 1540. (b) R. Vendamme, S.-Y. Onoue, A. Nakao, T. Kunitake, *Nat. Mater.*, **2006**, *5*, 494.

[2] A. Mamedov, N. A. Kotov, *Langmuir*, **2000**, *16*, 5530.

[3] (a) H. Ko, C. Jiang, H. Shulha, V. V. Tsukruk, *Chem. Mater.*, **2005**, *17*, 2490. (b) C. Jiang, H. Ko, V. V. Tsukruk, *Adv. Mater.*, **2005**, *17,* 2127. (c) C. Jiang, S. Markutsya, Y. Pikus, V. V. Tsukruk, *Nat. Mater.*, **2004**, *3,* 721. (d) R. Gunawidjaja, C. Jiang, S. Peleshanko, M. Ornatska, S. Singamaneni, V. V. Tsukruk, *Adv. Fun. Mater*., **2006**, *16*, 2024.

[4] (a) C. Jiang, V. V. Tsukruk, *Adv. Mater.*, **2006**, *18,* 829. (b) F. Hua, T. Cui, Y. M. Lvov, *Nano Lett.*, **2004**, *4*, 823; (c) C. Jiang, M. E. McConney, S. Singamaneni, E. Merrick, Y. Chen, J. Zhao, L. Zhang, V. V. Tsukruk, *Chem. Mater.*, **2006**, *18*, 2632. (d) V. Maheshwari, R. F. Saraf, *Science*, **2006**, *312*, 1501.

[5] S. S. Ono, G. Decher, *Nano Lett*., **2006,** *6*, 592.

[6] (a) Semiconducting Polymer, ed. G. Hadziioannou and P. F. van Hutten, Wiley-VCH, Weinheim, 2000**;** (b) E. Smela, *Adv. Mat.*, **2003**, *15*, 481.

[7] a) M. Ferreirat, M. F. Rubner, *Macromolecules*, **1995**, *28,* 7107. b) J. W. Baur, S. Kim, P. B. Balanda, J. R. Reynolds, M. F. Rubner, *Adv. Mater.*, **1998**, *10,* 1452.

[8] a) G. Yu, J. Gao, J. C. Hummelen, F. Wudl, A. J. Heeger, *Science*, **1995**, *270*, 1789. b) K. M. Coakley, Y. X. Liu, C. Goh, M. D. McGehee, *MRS Bulletin*, **2005,** *30*, 37.

[9] R. H. Friend, R.W. Gymer, A. B. Holmes, J. H. Burroughes, R. N. Marks, C. Taliani, D. D. C. Bradley, D. A. Dos Santos, J. L. Brédas, M. Lögdlund, W. R. Salabeck, *Nature*, **1999**, *397*, 121.

[10] Y. L. Loo, T. Someya, K. W. Baldwin, Z. N. Bao, P. Ho, A. Dodabalapur, H. E. Katz, J. A. Rogers, *Proc. Natl. Acad. Sci. USA*, **2002**, *99*, 10252.

[11]. P. S. Heeger, A. J. Heeger, *Proc. Natl. Acad. Sci. U. S. A.*, **1999**, *96*, 12219.

[12] B. J. Schwartz, *Ann. Rev. Phys. Chem.*, **2003**, *54,* 141.

[13] (a) H. G. Gilch, W. L. Wheelwright, *J. Polym. Sci., Polym. Chem.*, **1966**, *4*, 1337. (b) S. C. Chang, J. Bharathan, Y. Yang, R. Helgeson, F. Wudl, M. B. Ramey, J. R. Reynolds, *Appl. Phys. Lett.*, **1998**, *73*, 2561. (c) S. Shi, F. Wudl, *NATO ASI Ser., Ser. E*., **1990,** *182,* 83.

[14] (a) C. Jiang, S. Markutsya, V. V. Tsukruk, *Adv. Mater.*, **2004**, *16,* 157. (b) C. Jiang, S. Markutsya, H. Shulha, V. V. Tsukruk, *Adv. Mater.***, 2005**, *17,* 1669. (c) V. V. Tsukruk, D. H. Reneker, *Polymer*, **1995**, *36*, 1791. (d)V. V. Tsukruk, *Rubber Chem. Techn.,* **1997**, *70*, 430.

[15] a) A. Köhler, D. A. Dos Santos, D. Beljonne, Z. Shuai, J.-L. Brédas, A. B. Holmes, A. Kraus, K. Müllen, R. H. Friend, *Nature*, **1998**, *392*, 903. b) Z. Gu, Q.-D. Shen, J. Zhang, C.-Z. Yang, Y.-J. Bao, *J. Appl. Polym. Sci.*, **2006**, *100*, 2930.

[16] S.-J. Chung, K.-Y. Kwon, S.-W. Lee, J.-I. Jin, C. H. Lee, C. E. Lee, Y. Park, *Adv. Mater*., **1998**, *10,* 1112.

[17] Z. Liang, K. L. Dzienis, J. Xu, Q. Wang, *Adv. Funct*. *Mater.*, **2006**, *16*, 542.

[18] T.-Q. Nguyen, I. B. Martini, J. Liu, B. J. Schwartz, *J. Phys. Chem. B.*, **2000**, *104*, 237.

[19] (a) A. Marletta, F. A. Castro, C. A. M. Borges, O. N. Oliveira Jr., R. M. Faria, F. E. G. Guimaraes, *Macromolecules*, **2002**, *35,* 9105. (b) D. Moses, J. Wang, A. J. Heeger, N.

Kirova, S. Brazovski, *Synth. Met.*, **2001**, *119,* 503. (c) M. Ferreira, C. J. L. Constantino, C. A. Olivati, D. T. Balogh, R. F. Aroca, R. M. Faria, O. N. Oliveira Jr., *Polymer*, **2005**, *46*, 5140. (d) M. B. Ramey, J.-A. Hiller, M. F. Rubner, C. Tan, K. S. Schanze, J. R. Reynolds, *Macromolecules*, **2005**, *38*, 234; (e) A. P. H. J. Schenning, E. Peeters, E. W. Meijer, *J. Am. Chem. Soc.*, **2000**, *122*, 4489.

[20] K.-Y. Peng, S.-A. Chen, *J. Phys. Chem. B*, **2005**, *109*, 9368.

[21] J. Tang, W. J. Li, Y. Wang, B. Wang, J. Sun, B. Yang, *J. Photochem. Photobiol. A*, **2001**, *141*, 179.

[22] H. Hong, D. Davidov, M. Tarabia, H. Chayet, I. Benjamin, E. Z. FaFaraggi, Y. Avny, R. Neumann *Synth. Met.,* **1997***, 85,* 1265.

[23] (a) M. J. Winokur, W. Chunwachirasiri, *J. Phys. Chem. B.,* **2003**, *41,* 2630. (b) S. Siddiqui, F. C. Spano, *Chem. Phys. Lett.*, **1999,** *308*, 99. (c) K. S. Bourbon, M. Gao, U. De Rossi, *Isr. J. Chem.*, **2000**, *40,* 130. (d) I. G. Scheblykin, L. S. Lepnev, A. G. Vitukhnovsky, M. Van der Auweraer, *J. Lumin.*, **2001,** *94,* 461.

[24] G. Yang, Y. Li, J. O. White, H. G. Drickamer, *J. Phys. Chem. B.*, **1999**, *103*, 5181.

[25] P. K. Jain, S. Eustis, M. A. El-Sayed, *J. Phys. Chem. B.*, **2006**, *110*, 18243.

[26] S. Yokojima, D.-H. Zhou, G.-H. Chen, *Chem. Phys. Lett.*, **2001**, *333*, 397.

[27] S. Markutsya, C. Jiang, Y. Pikus, V. V. Tsukruk, *Adv. Funct. Mater.*, **2005**, *15*, 771.

[28] A. J. Nolte, M.F. Rubner, R.E. Cohen, *Macromolecules*, **2005,** *38*, 5367.

[29] C. Jiang, S. Singamaneni, E. Merrick, V. V. Tsukruk, *Nano Lett.*, **2006**, ***6***, 2254.

CHAPTER 10
SCULPTURED LAYER-BY-LAYER FILMS

A paper accepted in Advanced Materials, 2007

Yen-Hsi Lin,[ab] Chaoyang Jiang,[a] Jun Xu,[b] Zhiqun Lin[b],Vladimir V. Tsukruk[a]

a. School of Materials Science & Engineering, Georgia Institute of Technology, Atlanta, Georgia 30332, U.S.A

b. Department of Materials Science & Engineering, Iowa State University, Ames, Iowa 50011, U.S.A

Abstract

We report freely standing, three-dimensional, layer-by-layer (LbL) films with the microscopic periodic modulations of refractive properties. The modulated refractive properties are achieved by the topological variation of the film shape that generates optical diffraction effects with bright structural colors and optical grating properties. An LbL deposition on a sacrificial microimprinted substrate was employed to generate such a sculptured LbL structure with the effective thickness of 60 nm and the 160-nm peak-to-peak modulation.

Introduction

Precise assemblies of nanostructured materials into two and three dimensional periodic microscopic arrays are achieved by employing various assembling technologies such as microparticle self-organization,[1] photolithography,[2] holographic lithography,[3] selective chemical etching,[4] ink printing,[5] laser-based polymerization,[6] selective responsive grafting[7], and inversion of bilayers.[8] Soft lithography, such as microcontact printing has been widely applied to tackle this challenge in few steps, with a submicron resolution, and at low cost.[9,10,11] It has been demonstrated that the most popular fabrication of well-defined nanostructured materials with layer-by-layer (LbL) assembly can be combined with

♦ Primary researcher; carried out most of experiments, writer of all drafts

photolithography and microprinting to fabricate complex 2D and 3D structures with modulated distribution of different components.[12 , 13 , 14] Examples of micropatterned assembly of nanoparticles, microchannels, antireflective coatings, and Raman arrays have already reported.[15,16,17,18,19,20] A variety of functional materials have been utilized in the LbL construction to make these structures suitable for prospective applications as antiwetting coatings, sensitive films for solar cells, fuel cells, ultra-strong nanomaterials, microcapsules, and membranes for controlled drug release.[21,22,23,24,25,26,27] On the other hand, microstructural arrays based upon the principles of either diffraction or refraction with in-printed microscopic modulations are extensively used as optical components such as grating, beam splitters, microlenses, displays, and mirrors.[28,29,30,31]

A vast majority of LbL structures has been fabricated on solid planar or curved (microparticle) supports and represented essentially 2D planar structures with vertical (along the surface normal) modulations of chemical composition. Micropatterning of LbL films has been recently reviewed by Hammond.[32] Few examples of free-standing LbL structures have been reported either in the form of uniform, micropatterned, or curved shell structures.[33,34,35 3637] Therefore, although potential for the fabrication of interesting modulated structures, which provides for optical effects, is inherently present in the LbL technology, few attempts have been made to investigate the feasibility of the fabrication of modulated LbL structures for light control. In a recent study, Rubner has demonstrated that properly matched LbL coating can serve for constructive-destructive light interferences with efficient antireflective ability.[18,38] In a related study, Rubner and Cohen have demonstrated that a proper modulation of the reflective index within LBL films might lead to pronounced structural color effect with selective reflection of visible light controlled by the reflective index modulation rather than the presence of conjugated molecules with proper electronic structures.[39] Although these initial studies showed some potential in LbL technology to generate nanostructures materials with the ability to control visible light diffraction, they have been limited to one-dimensional modulation of the refractive properties.

In this communication, we report an example of three-dimensional (3D) LbL grating structures with the ability to diffract light due to modulation of local LbL film shape with microscopic periodicity. In these freely-suspended 3D LbL films, the effective modulation of the refractive properties is caused by the topological variation of the local film shape, thus representing a purely structural color effect. A simple and economical spin-assisted LbL deposition on a sacrificial microimprinted substrate was employed here for conjugated polyelectrolytes to generate robust, free-standing sculptured LbL structure with the effective thickness of 60 nm and the 160-nm peak-to-peak modulation of square lattice with 2.5-μm periodicity (Figure 10-1). These films demonstrated efficient optical grating properties and bright structural colors in a reflective mode controlled by the in-plane spacing and the angle of incidence.

Results and Discussion

Conjugated polyelectrolyte, poly(2,5-methoxypropyloxy sulfonate phenylene vinylene) (MPS-PPV) applied in this LbL assembly was critical in providing mechanically strong structure as has been tested in our previous work to fabricate mechanically robust planar ultrathin LbL films.[40] MPS-PPV is a well known water-soluble conjugated polymer with highly charged, stiff backbone, and strong fluorescence properties.[26] LbL films from MPS-PPV and poly(allylamine hydrochloride) (PAH) demonstrate excellent mechanical properties combined with high fluoresce as has been demonstrated in our previous work.[40] Figure 10-1 shows a schematic of the experimental procedure, including the use of a micropatterned sacrificial substrate and spin-assisted LbL (SA-LbL) assembly. A sacrificial polystyrene (PS) micropatterned template was first obtained by using capillary transfer microprinting as discussed in a previous publication[34] and LbL film has been fabricated and released to form free-standing films with dimensions about 0.3 mm x 0.3 mm and clearly seeing square micropattern over a large surface area (Fig. 1, see Methods).[33]

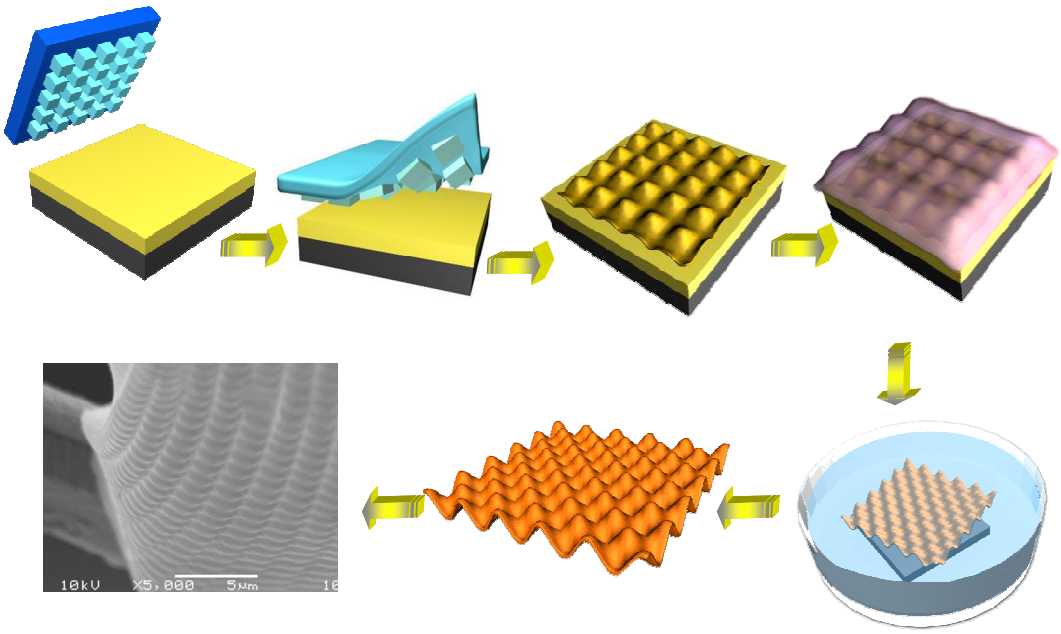

Figure 10-1. Schematic illustration of the route for the fabrication of sculptured LbL films by combining microstamping and sacrificial templates and SEM image of the freely standing film with a square pattern.

AFM topographical image demonstrates a square lattice on a PDMS stamp exploited to form micropatterned sacrificial substrate (Figure 10-2a). The spacing in this sacrificial micropattern was 2.4 μm with a diagonal distance of 3.4 μm and 400 nm difference in elevations. The AFM imaging of the freely suspended LbL film, conducted in light tapping mode on both sides of the film, revealed a topographical 3D replica of the original micropatterned substrate with the periodicity of modulation identical (within experimental errors) to those in the original microstamp (see topography of both sides and corresponding cross-sections in Figure 10-2 b-d). Apparently, the 3D structure of the sacrificial micropatterned PS template have been successfully replicated into the 3D topology of the nanoscale LbL film with a "nominal" thickness of about 60 nm with original square shape of the template smeared during assembly (Figure 10-2c).

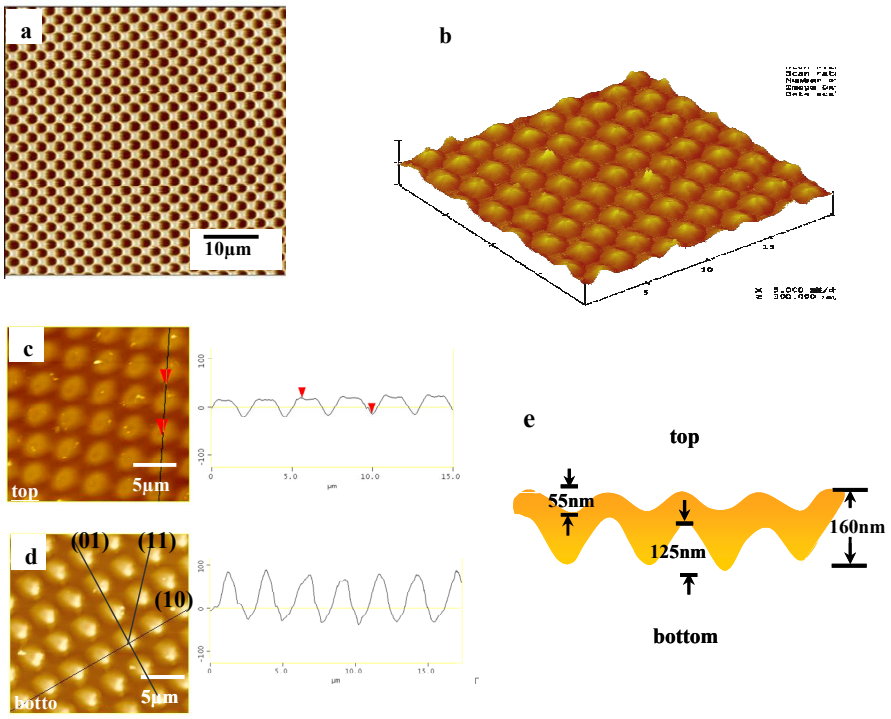

Figure 10-2. a) AFM image of the PDMS stamp used for capillary transfer; b) AFM 3D surface plot of released LbL film; AFM line profile analysis of c) top and d) bottom of freely standing sculptured LbL film on TEM grid; e) Schematics of 3D LbL film with major dimensions.

The overall "thickness" (peak-to-peak value) of the sculptured 3D LbL film reached 160 nm which is smaller than the elevation difference in the original template, indicating some contraction in the process of drying and transfer. Although AFM images of top and bottom surfaces display modulated shape of the LbL film with "in-printed" periodicity, the difference in the cross-sectional shape suggests an asymmetric morphology (Figure 10-2e). The bottom side of LbL film, which was in the contact with micropatterned sacrificial layer, has a difference in elevations of 125 nm while the top side of film showed smaller difference of 55 nm (Figure 10-2d). We believe that this difference between two sides is due to the relative small channel length of 2D patterned PS sacrificial layer and it might be also related to the features of the array processing such as uneven water access due to the surface topography during LbL deposition.

The optical and fluorescence images of 3D LbL film suspended on the TEM grid or across the 150 μm round opening within a copper holder showed large defect-free areas with clearly visible imprinted square lattice (Figures 10-3 and 4). The fluorescence of the MPS-PPV observed in solution is preserved in this state as confirmed by photoluminiscence spectrum (inset in Figure 10-3b), showing green fluorescence with an emission maximum at 530 m which is blue-shifted (see earlier discussion on planar MPS-PPV LbL films). Pieces of damaged LbL film showed very regular fracturing with straight cracks propagating always along the lattice cell sides and changing a register in a "quantified" manner with an integer number of lattice cells (Figure 10-3c). This type of the "organized" brittle fracture under high stresses has been reported for three-dimensional ordered microporous solids fabricated with interference lithography and has been associated with the preferential crack propagation along "weak lines" in the lattices.[3] Higher magnification of the fractured LbL film showed a regular patterns on two sides of the 3D array with a characteristic smeared-squared shape of the individual cells as discussed above (Figure 10-2c, 3d). It is worth to note that other micropatterns with different symmetries and dimensions can be generated by exploiting the same approach with spacings ranging from 1 to 20 μm as will be discussed in further publications.

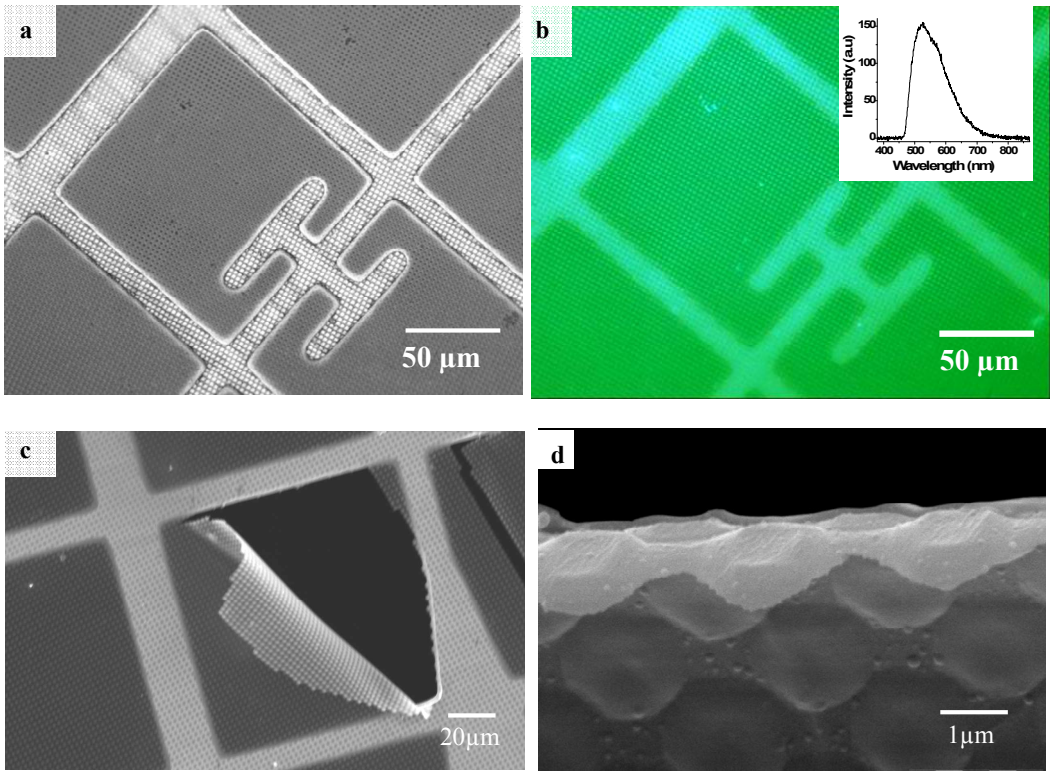

Figure 10-3. Sculptured LbL film on TEM grid: a) optical image, b) fluorescence image with fluorescence spectrum (inset), c) SEM image of the damaged piece of the 3D LbL film with characteristic fracturing (top view), d) high resolution SEM image of freely standing 3D LbL film (side view).

Micromechanical properties of sculptured LbL films have been tested under both compressive and tensile modes in accordance with usual procedures.[41,42,43,44] The film deflection under a hydrostatic pressure applied from one side is shown in Figure 10-4b in comparison with conventional planar LbL film with identical composition. The sculptured LbL films showed much higher deflection indicating less stiff response associated with modulated 3D shape of the polymer film. In fact, the effective elastic modulus of this structures obtained from the data analysis was calculated to be within 0.4 ± 0.1 GPa which is an order smaller than that found earlier for planar MPS-PPV LbL film.[40] This value of the elastic modulus is a characteristic of tough rubbery polymers rather than conjugated polymers in the glassy state. Such a significant difference implies very different mechanisms of the elastic deformation for planar and

sculptured films within strain range 0.35-0.5%. We suggest that the expansion ("unfolding") of 3D modulated structure occurs in sculptured LbL films in contrast to the ordinary tensile deformation of conjugated backbones in the planar film. Moreover, very low resistance under tensile stress has been also confirmed with the film compression.[45] For this test, the 3D LbL film was transferred to a PDMS substrate and compressed by 0.1-0.5% until periodic buckling pattern appeared (Figure 10-4c). Spacing of these wrinkles determined from optical micrographs was 3.6 ± 0.2 μm as obtained from Fourier transforms (Figure 10-4d). This peridocity corresponds to the elastic modulus of 0.30 ± 0.03 GPa, which is close to that measured from tensile deformation.[46] It is interesting to note that this spacing corresponds to the "diagonal" direction in the square lattice of the modulated areas and, thus, the collapse of the squared lattice under compression occurs along the direction which includes the widest gap between modulations (between next-next neighbors) in contrast to tensile deformation with unfolding occurring between next neighbors (Figure 10-2d). Therefore, the symmetry of the sculptured structure defines preferential fracturing directions along the rows of modulated areas under tensile stress ((01) and (10) directions) and different (11) direction (at angle 45^{o}) for collapse of this film under compressive stress (Figure 10-2d).

Finally, bright coloration was observed for sculptured LbL film transferred on a silicon wafer in a reflection mode in contrast to planar LB films which show weak brownish color due to absorption of conjugated backbones.[40] Our experiments showed that the white light can be reflected by 3D LbL with the intense color changing from blue to red while adjusting the view angle (Figure 10-5a). The intensity of the color is remarkable considering that the physical thickness of the LbL film is only 60 nm. Correspondingly, the 2D diffraction pattern is observed under an incident illumination from a He-Ne laser (λ = 632 nm). Bright diffraction spots forming a square lattice can be seen beyond the third order (Figure 10-5b). The diffraction pattern produced by 3D LbL film should follow a Fraunhofer diffraction law with positions of individual spots in a reciprocal space defined by the symmetry and spacing of the modulations in real

space.[47] Thus, from multiple diffraction orders (m) we estimated the expected distribution of the diffraction spots taking into account the known spacing of the square modulations of 2.4 μm. Under this assumption, excellent coincidence was observed between the experimental positions measured and those estimated from the spacing of the LbL modulations as demonstrated for the (01) direction (Figure 10-5c).

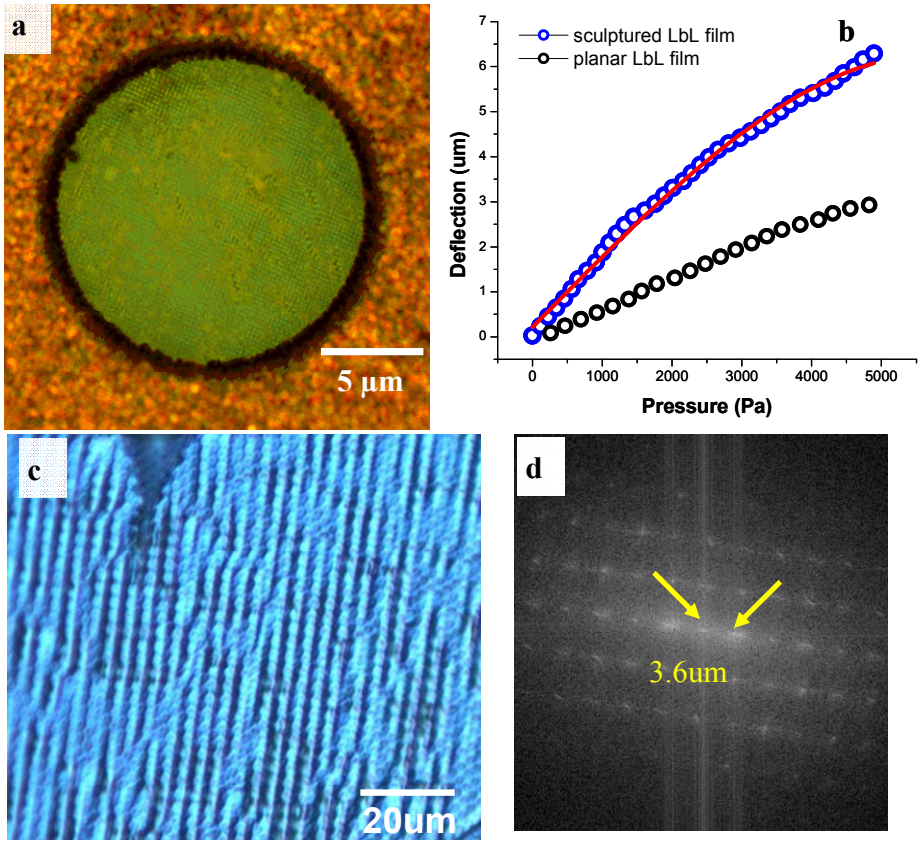

Figure 10-4. Sculptured LbL film suspended across opening into the copper holder (a); mechanical testings: bulging test for sculptured and planar LbL films, solid line shows theoretical fit (b); buckling pattern (c) and corresponding 2D FFT (d) for compressed 3D LbL film.

Thus, the modulated refractive properties achieved by the topological variation of the LbL film shape can generate intense structural color effect with bright structural colors and optical grating properties, a phenomenon which can be of interest for light-

controlling polymeric microdevices. Overall, this study shows an interesting potential in LbL technology to generate optically-relevant nanostructured materials with the ability to control visible light diffraction beyond one-dimensional modulation of the refractive properties reported before.

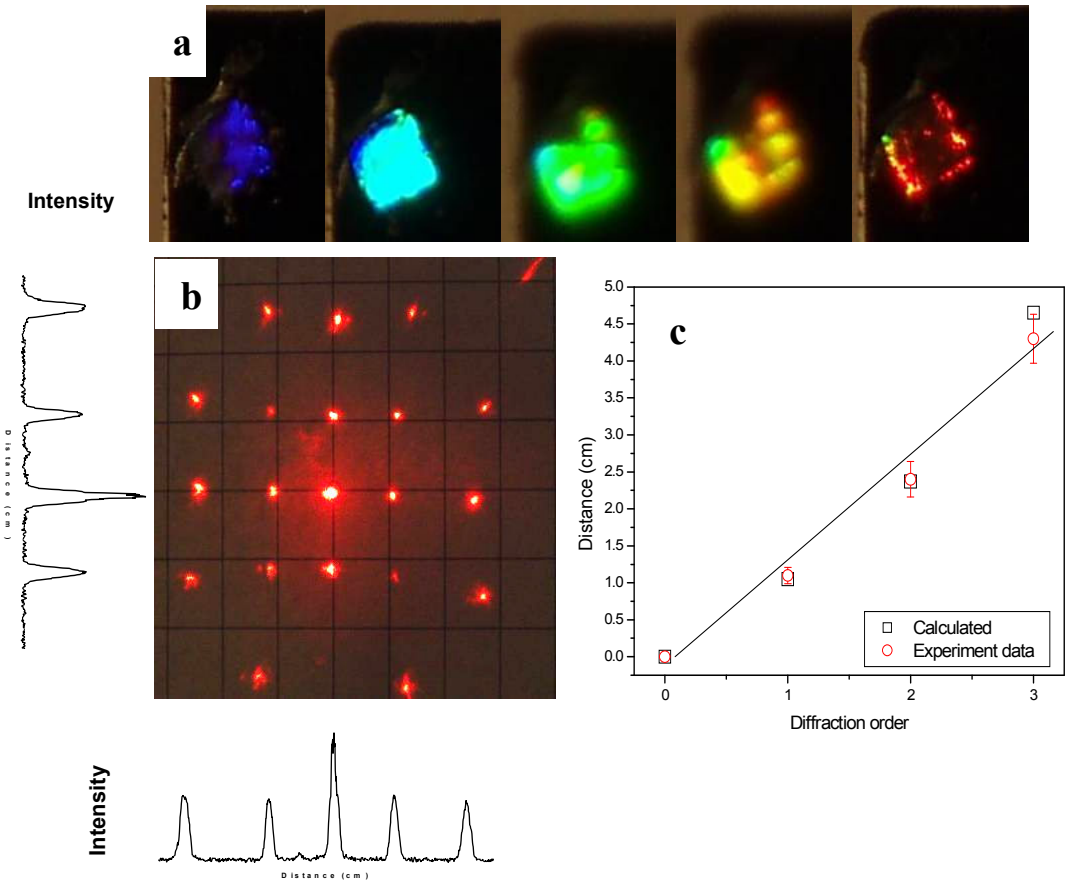

Figure 10-5. a) Sculptured LbL film with different structural colors generated at different viewing angles. b) The diffraction pattern produced by the LbL film in the reflection mode with intensity versus distance profiles. c) The calculated and experimental positions of diffraction spots of different orders along the (01) direction.

Experimental

Poly(allylamine hydrochloride) (PAH, MW = 65,000) was purchased from Aldrich and used as received. Water soluble conjugated polymer MPS-PPV was synthesized according to the known routine and described before.[40 48] The (100) silicon wafers with a typical size of 10 mm × 20 mm were cleaned in piranha solution (3:1 mixture of H_2SO_4/H_2O_2) for 1 h and then rinsed thoroughly with Nanopure water (resistivity 18 MΩ cm). PDMS stamps were prepared by curing liquid prepolymer (Sylgard 184, Dow Chemical) on top of a corresponding silicon master (Mikromasch) at 60 °C for 1 h in a vacuum oven.

The experimental procedure for fabricating 3D sculptured LbL film is outlined in Figure 10-1. First layer of sacrificial PS film (MW=200 000, 2% in toluene) was spin cast (3000 rpm for 20 s) on a silicon wafer and a second layer of sacrificial PS micropattern has been fabricated by using capillary transfer lithography.33 For this procedure, PDMS stamp was soaked in toluene for 1-2 min and brought into conformal contact with the PS film on the PDMS substrate and pressed for 1 min. When the PDMS stamp was detached, the PS material was trapped inside the recessed regions of the PDMS stamp. The polymer pattern formed in this way was then immediately transferred onto the first sacrificial PS layer by conformal contact of the PDMS stamp for 1 min.[33] Tetrahydrofuran solution (THF) was used to dissolve the sacrificial PS layer in order to release the films. The polymer films with different thicknesses were fabricated using spin-assisted LbL (SA-LbL) method as described in detail in previous publications.[33,36] A droplet (150 μl) of 0.2% (w/w) MPS-PPV and PAH layers were deposited in an alternating manner. This procedure was repeated until the needed 25 of polymer bilayers. The LbL film presented here in detail has a general formula $(MPS\text{-}PPV/PAH)_{25}$. The LbL films were transferred to Nanopure water where they could then be picked up with different substrates such as a highly polished copper plate with a single micromachined hole or a clean silicon wafer with and without holes.

AFM scanning was conducted on a Dimension 3000-Nanoscope IIIa microscope (Digital Instruments) according to usual procedure.[49,50] Film thickness on a silicon

substrate was obtained with AFM scans along the film edge. Photoluminescence image and spectrum were taken on a Leica DM 4000 microscope with a mercury source and attached CRAIC QDI202 microscopic spectrophotometer. The samples were excited at 365 nm and the emission spectra were collected within 400 - 1000 nm. SEM was conducted in secondary electron scattering mode at 5 keV (JEOL JSM-6060LV and JEOL 5800LV). The bulging test was conducted by applying a hydrostatic pressure to one side of an LbL film that covered a copper plate with 150 μm hole in accordance with a usual procedure.[37] The film deflection was measured using a custom-built interference optical set-up with a helium–neon laser and the elastic modulus was calculated as described earlier.[51] The experimental data was analyzed by using an appropriate equation for elastic membrane deformation as discussed in detail elsewhere.[51] At least 5 different specimens with same composition were tested. The buckling instability was observed for the film transferred to the PDMS substrate and the buckling pattern formed under compressive stress was analyzed according to the known procedure.[41,42]

References

1 M. H. Lu, Y. Zhang, *Adv. Mater.* **2006**, *18*, 3094.

2 S. Y. Lin, J. G. Fleming, *Nature* **1998**, *394*, 251.

3 J.-.H. Jang, C. K. Ullal, T. Choi, M. C. Lemieux, V. V. Tsukruk, E. L. Thomas, *Adv. Mater*, **2006**, *18*, 2123.

4 S. Noda, K. Tomoda, N. Yamamoto, A. Chutinan, *Science* **2000**, *289*, 604.

5 G. M. Gratson, M. Xu, J. A. Lewis, *Nature* **2004**, *428,* 386.

6 M. Campbell, D. N. Sharp, M. T. Harrison, R. G. Denning, A. J. Turberfield, *Nature* **2000**, *404*, 53.

7 Luzinov, S. Minko, V. V. Tsukruk, *Prog. Polym. Sci.* **2004,** *29,* 635

8 J. Léopoldès, P. Damman, *Nat. Mater*. **2006** *5*, 957.

9] a) E. Kim, Y. Xia, G. M. Whitesides, *Nature* **1995**, *376*, 581. b) J. Zaumseil, M. A. Meitl, J. W. P. Hsu, B. R. Acharya, K. W. Baldwin, Y.-L. Loo, J. A. Rogers, *Nano Lett.* **2003**, *3*, 1223.

[10] G. M. Whitesides, E. Ostuni, S. Takayama, X. Y. Jiang, D. E. Ingber, *Annu. Rev. Biomed. Eng.* **2001**, *3*, 335.

[11] K. Y. Suh, Y. S. Kim, H. H. Lee, *Adv. Mater*. **2001**, *13*, 1386.

[12] M. Mrksich, *Chem. Soc. Rev.* **2000**, *29*, 267.

[13] *Langmuir-Blodgett Films* (Ed: G. Roberts), Kluwer Academic Norwell MA 1990.

[14] G. Decher, *Science* **1997**, *277*, 1232.

[15] J. Park, L. D. Fouche, P. T. Hammond, *Adv. Mater.* **2005**, *17*, 2575.

[16] C. Jiang, S. Markutsya, V. V. Tsukruk, *Langmuir* **2004,** *20*, 882.

[17] C. Jiang, H. Ko, V. V. Tsukruk. *Adv. Mater.* **2005**, *17,* 2127.

[18] J. A. Hiller, J. D. Mendelsohn, M. F. Rubner, *Nat. Mater*, **2002**, *1*, 59

[19] F. Hua, T. Cui, Y. M. Lvov, *Nano Lett.* **2004**, *4*, 823.

[20] C. Jiang, V. V. Tsukruk, *Adv. Mater.* **2006**, *18*, 829.

[21] L. Zhai, M. C. Berg, F. C. Cebeci, Y. Kim, J. M. Milwid, M. F. Rubner, R. E. Cohen, *Nano Lett.* **2006**, *6*, 1213.

[22] C. Jiang, S. Markutsya, Y. Pikus, V. V. Tsukruk, *Nat. Mater.* **2004**, *3*, 721.

[23] A. G. Agrios, I. Cesar, P. Comte, M. K. Nazeeruddin, M. Grätzel, *Chem. Mater.* 2006, 18, 5395.

[24] Z. Tang, N. A. Kotov, S. Magonov, B. Ozturk, *Nat. Mater.* **2003**, *2*, 413.

[25] D. N. Lynn, *Soft Matter* **2006**, *2*, 269.

[26] A. G. Skirtach, C. Dejungnat, D. Braun, A. S. Susha, A. L. Rogach, W. J. Parak, H. Möhwald, G. B. Sukhorukov, *Nano Lett.* **2005**, *5*, 1371; Z. Tang, N. A. Kotov, S. Magonov, B. Ozturk, *Nat. Mater.* **2003**, *2*, 413; F. Caruso, *Adv. Mater.* **2001**, *13*, 11.

[27] J. W. Baur, S. Kim, P. B. Balanda, J. R. Reynolds, M. F. Rubner, *Adv. Mater.* **1998**, *10*, 1452.

[28] J. Kim, M. J. Serpe, L. A. Lyon, *Angew. Chem. Int. Ed.* **2005**, *44*, 1333.

[29] J.-Y. Ha, D.-Y. Jeong, J.-S. Kim, S.-J. Yoon, *J. Opt. A: Pure Appl. Opt*. **2007**, *9*, 170.

[30] M. Wu, T. W. Odom, G. M. Whitesides, *Adv. Mater*. **2002**, *14*, 1213.

[31] K.-H. Jeong, J. Kim, L. P. Lee, *Science* **2006**, *312*, 557.

[32] P. T. Hammond, *Adv. Mater.* **2004**, *16*, 1271.

[33] A. Mamedov, N. A. Kotov, *Langmuir*, **2000**, *16*, 5530.

[34] H. Ko, C. Jiang, V. V. Tsukruk, *Chem. Mater.* **2005**, *17*, 5489.

[35] F. Hua, T. Cui, Y. M. Lvov, *Nano Lett.* **2004**; *4*, 823.

[36] C. Jiang, S. Markutsya, H. Shulha, V. V. Tsukruk, *Adv. Mater.* **2005**, *17,* 1669.

[37] C. Jiang, S. Markutsya, V. V. Tsukruk, *Adv. Mater.* **2004**, *16*, 157.

[38] Z. Wu, J. Walish, A. Nolte, L. Zhai, R. E. Cohen, M. F. Rubner, *Adv. Mater.*, **2006**, *18,* 2699.

[39] W. Zhizhong, D. Lee, M. F. Rubner, R. E. Cohen, *Small*, in print

[40] Y.-H. Lin, C. Jiang, J. Xu, Z. Lin, V. V. Tsukruk, *Soft matter*, **2007**, *3*, 432.

[41] A. J. Nolte, M. F. Rubner, R. E. Cohen, *Macromolecules* **2005,** *38*, 5367.

[42] C. Jiang, S. Singamaneni, E. Merrick, V. V. Tsukruk, *Nano Lett.* **2006,** *6*, 2254.

[43] S. Jayaraman, R. L. Edwards, K. J. Hemker, *J. Mater. Res.* **1999**, *14*, 688.

[44] C. Poilane, P. Delobelle, C. Lexcellent, S. Hayashi, H. Tobushi, *Thin Sol. Films* **2000**, *379*, 156.

[45] C. M. Stafford, C. Harrison, K. L. Beers, A. R Karim, E. J. Amis, M. R. VanLandingham, H.-C. Kim, W. Volksen, R. D. Miller, E. E. Simonyi, *Nat. Mater*. **2004**, *3*, 545.

[46] A. L. Volynskii, S. Bazhenov, O. V. Lebedeva, N. F. Bakeev, *J. Mater. Sci.* **2000**, *35*, 547.

[47] D. Winoto, S. H, Carr, *Macromolecules* **1996,** *29*, 5149.

[48] A. D. Smith, C. K. F. Shen, S. R. Roberts, R. Helgeson, B. J. Schwartz, http://www.chem.ucla.edu/dept/Faculty/schwartz/schwartz_complete_pubs.htm

[49] V. V. Tsukruk, D. H. Reneker, *Polymer* **1995**, *36*, 1791.

[50] V. V. Tsukruk, *Rubber Chem. Techn.* **1997**, *70*, 430.

[51] S. Markutsya, C. Jiang, Y. Pikus, V. V. Tsukruk, *Adv. Funct. Mater.* **2005**, *15*, 771.

CHAPTER 11
GENERAL CONCLUSIONS

The sensor devices employ polymers with define roles either in sensing mechanism or through immobilizing the species responsible for sensing component because polymer can be tailored for particular properties and easily processed. We have explored a series of responsive materials at nanoscale for sensor applications. This research utilized several potential approaches to improve and control over interfacial behavior of polymeric films and sensor substrate. Specific conclusions for different types of polymers studied here are presented as below. Throughout this study, several novel innovations and significant contributions were made for the development or improvement of surface responsive materials. It can be divided into three categories: 1) switchable adaptive polymer nanolayer on a planer silicon substrates, 2) compliant polymer or nanocomposite nanolayer enhance/improve the sensitivity of current microcantilever based sensors 3) assembled ultra thin LbL films with optical grating 3D structure. 4) polymer nanolayer on nanobelts with enhanced photoconductivities.

1) Switchable adaptive polymer nanolayer on silicon substrate

We demonstrated surface reorganization of Y-shaped brushes resulted in dramatic changes from uniform, repellent, compliant layer covered by swollen PS arms in toluene to adhesive, mixed layer composed of coexisting swollen PAA and collapsed PS arm in water. We believe that these smart layers with efficient switchable properties in different fluids and the overall thickness not exceeding several nanometers can serve as adaptive coatings for nanofluidic channels with stimuli-responsive properties. The nanoscale thickness of these switchable surface layers firmly grafted to the silicon surfaces (well below the thickness of conventional surface coatings (hundred nanometers)) can be critical for advanced applications such as controlling fluidic flow or selective adsorption within channels with a diameter below 100 nm that remains unachievable by any synthetic or lithographic techniques.

Furthermore, we also demonstrated that the variation of the grafting density and selective solvent treatment of the micropatterned Y-shaped brushes influence the density and the modes of surface adsorption of gold nanoparticles creating micropatterns with variable contrast. This behavior is controlled by Coulombic interactions between oppositely charged gold nanoparticles.

2) Compliant polymer or nanocomposite nanolayer enhance/improve the sensitivity of current cantilever based sensor

For designing thermally sensitive microcantilevers, the polymer layers were reinforced with carbon nanotubes and metal nanoparticles. Such a combination of materials within the strong polymer composite topmost layer provides for high thermal stresses that results in significant (*up to fourfold*) increase in the thermal sensitivity as compared with conventional ceramic-metal bilayered microcantilevers. These trilayered polymer-metal-ceramic microcantilevers with dramatically enhanced thermal sensitivity can serve as basis for the next generation of un-cooled IR sensor arrays with the thermal and spatial resolution manifold higher than those currently available.

3) Assembled ultra thinLbL films with optical grating 3D structure

A freely standing, three-dimensional, LbL films from conjugated polymers with the microscopic periodic modulations of refractive properties were introduced presented in this study. The modulated refractive properties are achieved by the topological variation of the film shape that generates optical diffraction effects with bright structural colors and optical grating properties. An LbL deposition on a sacrificial microimprinted substrate was employed to generate such a sculptured LbL structure with the effective thickness of 60 nm and peak-to-peak modulation of square lattice with 2.5-μm periodicity. These films demonstrated efficient optical grating properties and bright structural colors in a reflective mode controlled by the in-plane spacing and the angle of incidence.

.

4) Polymer nanolayer on nanobelts with enhanced photoconductivities

We demonstrated that plasma polymerized Acrylonitrile (PP-AN) coating (250nm) on the ZnO NB increased its photonconductivity by under UV irradiation a factor of 750 in comparison to that of a bare ZnO NB. This effect is suggested to be cause by of the high efficiency of exciton dissociation under UV illumination due to efficient electron transfer from valence band of ZnO NB to the PP-AN and then back to the conduction band of ZnO. This provides a simple and cost-effective approach for significant improving the performance of oxide NW/NB-based devices for photondetection, possibly leading to a motivation for studying the optoelectronic properties of inorganic–organic hybrid nanomaterials.

This research demonstrated an extensive range of work but the main conclusion that can be drawn from this thesis is that nanoscale responsive polymeric nanoscale film and the design of more active and sensor specific polymer will lead to successful miniature sensor arrays. The studies presented in this work provide several novel selection and development of proper sensing polymer materials as well as improved and recognition mechanisms necessary for instant identification of sensing target and also mechanism to create the signal that is obtained from the sensing device. The work here represents a successful effort to develop functional sensors with nanoscale dimensions. Responsive polymer film are designed and fabricated, integrated into sensors as active nanolayers, and the response to various environments was shown and proven in this research..

BIOGRAPHY

Refereed publications

1. **Lin, Y.-H.**; Jiang, C**.** Xu, J.**;** Lin, Z.; Tsukruk, V. V.; Sculptured Layer-by-Layer Films , Advanced Materials, 2007, Accepted.
2. He, J.-H., **Lin, Y.-H.;** McConney, M. E., Tsukruk, V. V. , Bao, G., Wang Z. L." Colossal UV Photon Conductivity of ZnO Nanobelt by Polyacrylonitrile Functionalization, Advanced Materials, under review.
3. **Lin, Y.-H.**; Jiang, C**.** Xu, J.**;** Lin, Z.; Tsukruk, V. V.; "Robust Fluorescent Freestanding LbL Conjugated Films with below 20 nm thickness", *Soft Matter*, **2007**, *3*, 432.
4. **Lin, Y.-H.**; McConney, M. E.; LeMieux, M. C.; Peleshanko S.; Jiang, C.; Singamaneni, S.; Tsukruk, V. V.; "Trilayered Ceramic-Metal-Polymer Microcantilevers with Dramatically Enhanced Thermal Sensitivity", *Advanced Materials*, **2006**, 18, 1157 (***Inside cover story***).
5. LeMieux M. C.; McConney, M. E.; **Lin, Y.-H**.; Singamaneni, S.; Jiang, H.; Bunning, T. J.; Tsukruk, V. V, "Polymeric Nanolayers as Actuators for Ultrasensitive Thermal Bimorphs *Nano letter*, **2006,** 6, 730.
6. **Lin, Y.-H.**; Teng, J.; Zubarev, E. R.; Peleshanko S.; Tsukruk,V. V. **Responsive Polymer Materials**:"Designs and Applications: Controlling Selective Adsorption on Patterned Gradient Y-shaped Amphiphilic Brushes" (Ed. S. Minko **book chapter**), Blackwell Professional, **2006**.
7. LeMieux, M. C.; **Lin, Y.-H.;** Cuong, P. D.; Ahn, H.-S.; Tsukruk, V. V.; "Nanomechanical and Nanoscale Surface Properties of Switchable Y-shaped Amphiphilic Brushes in Fluid" *Advanced Functional Materia*ls **2005**, 15, 1529.
8. Shulha, H.; **Lin, Y.-H.;** Tsukruk, V. V. **Application of Scanned Probe Microscopy to Polymers** *"Multilayerd Nanoscale Systems and Atomic Force Microscopy Mechanical Measurements"* (Eds: D. J. Batteas, C. A. Michaels, and G. C. Walker, **book chapter**), American Chemical Society, **2005.**

9. **Lin, Y.-H.**; Teng, J.; Zubarev, E. R.; Shulha, H.; Tsukruk,V. V. "Observing Nanoscale Fluidic Flip-Flops: Switchable Y-shaped Brushes in Selective Solvents", *Nano letter*, **2005**, 5, 491.
10. LeMieux, M. C.; Julthongpiput, D., Cuong, P. D.; Ahn H-S; **Lin, Y-H.**; Tsukruk, V. V. "Ultrathin Binary Grafted Polymer Layers with Switchable Morphology" *Langmuir***, 2004,** *20*; 10046.
11. Julthongpiput, D.; **Lin, Y.-H.**; Teng, J; Zubarev, E. R.; Tsukruk, V. V. "Y-Shaped Amphiphilic Brushes with Switchable Micellar Surface Structures" *Journal of the American Chemical Society*, **2003,** 125, 15912.

Presentations and Proceedings

- Materials Research Society Spring Meeting in San Francisco, CA, **2007**
- 231th American Chemical Society National Meeting in Atlanta, GA, **2006.**
- 230th American Chemical Society National Meeting in Washington DC, **2005.**
- 226th American Chemical Society National Meeting in New York, NY **, 2003.**

- **Lin Y.-H.**; LeMieux, M. C; McConney, M. E.; Tsukruk, V. V ***Designing active polymer nanolayers on free standing ceramic structures.*** Abstracts of Papers, 231st ACS National Meeting, Atlanta, **2006.**
- **Lin, Y.-H.**; LeMieux, M. C; Tsukruk, V. V. ***Switchable Y-shaped brushes and nanomechanical properties in selective fluids.*** **Polymer** Preprints ACS National Meeting, **2005**, *46, 95.*
- LeMieux, M. C.; Peleshanko, S.; **Lin, Y.-H.**; Tsukruk, V. V. ***The fabrication of smart surfaces with different architecture nanomechanical properties***. Polymer Preprints, ACS National Meeting **2005**, *46*, 20.
- Julthongpiput, D.; **Lin, Y-H.**; Teng, J.; Zubarev, E. R.; Tsukruk,V. ***Surface properties of novel Y-shape polymer brush grafted on silicon surface***. Polymer Preprints ACS National Meeting, **2003**, *89*, 344.